

**SURFACE CHARACTERIZATION USING THE RESTRICTED APERTURE  
ACOUSTIC MICROSCOPE**

**DISSERTATION**

Submitted in Partial Fulfillment  
of the Requirements for the  
Degree of

**DOCTOR OF PHILOSOPHY ( Electrophysics)**

at the

**POLYTECHNIC UNIVERSITY**

Brooklyn, NY

by

**Dmitry Chizhik**

**June 1991**

Approved:

*AL Baidoni*

Department Head

Copy No. \_\_\_\_\_

**DTIC QUALITY INSPECTED 5**

5/16, 1991

19981202 031

# REPORT DOCUMENTATION PAGE

Public reporting burden for this collection of information is estimated to average 1 hour per response, including the and maintaining the data needed, and completing and reviewing the collection of information. Send comments information, including suggestions for reducing this burden, to Washington Headquarters Services, Directorate for 1204, Arlington, VA 22202-4302, and to the Office of management and Budget, Paperwork Reduction Project (0704

AFRL-SR-BL-TR-98-

0776

ering  
on of  
Suite

1. AGENCY USE ONLY (Leave Blank)		2. REPORT DATE June 1991	3. REPORT TYPE AND DATES COVERED Final
4. TITLE AND SUBTITLE Surface Characterization Using the Restricted Aperture Acoustic Microscope			5. FUNDING NUMBERS
6. AUTHORS Dmitry Chizhik			
7. PERFORMING ORGANIZATION NAME(S) AND ADDRESS(ES) Polytechnic University, NY			8. PERFORMING ORGANIZATION REPORT NUMBER
9. SPONSORING/MONITORING AGENCY NAME(S) AND ADDRESS(ES) AFOSR/NI 4040 Fairfax Dr, Suite 500 Arlington, VA 22203-1613			10. SPONSORING/MONITORING AGENCY REPORT NUMBER
11. SUPPLEMENTARY NOTES			
12a. DISTRIBUTION AVAILABILITY STATEMENT Approved for Public Release			12b. DISTRIBUTION CODE
13. ABSTRACT (Maximum 200 words) See attachment			
14. SUBJECT TERMS			15. NUMBER OF PAGES
			16. PRICE CODE
17. SECURITY CLASSIFICATION OF REPORT Unclassified	18. SECURITY CLASSIFICATION OF THIS PAGE Unclassified	19. SECURITY CLASSIFICATION OF ABSTRACT Unclassified	20. LIMITATION OF ABSTRACT UL

**SURFACE CHARACTERIZATION USING THE RESTRICTED APERTURE  
ACOUSTIC MICROSCOPE**

**DISSERTATION**

Submitted in Partial Fulfillment  
of the Requirements for the  
Degree of

**DOCTOR OF PHILOSOPHY ( Electrophysics)**

at the

**POLYTECHNIC UNIVERSITY**

Brooklyn, NY

by

**Dmitry Chizhik**

**June 1991**

Approved:

\_\_\_\_\_

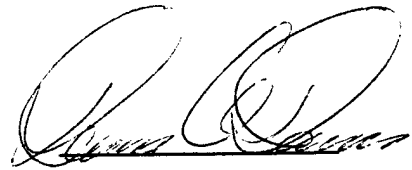
Department Head

Copy No. \_\_\_\_\_

\_\_\_\_\_, 19

Approved by the Guidance Committee:

Major: Electrophysics:

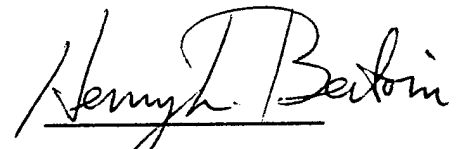


Douglas A. Davids

Thesis advisor/

Associate Professor

of Electrophysics



Henry L. Bertoni.

Chairman/Professor

of Electrophysics

Minor: Physics

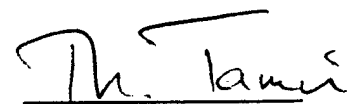


Ming Leung

Associate Professor

of Physics

Additional Committee Member:



Theodor Tamir

Professor of Electrical

Engineering and

Electrophysics.

Microfilm or other copies of this dissertation are obtainable from

UNIVERSITY MICROFILMS

300 N. Zeeb Road

Ann Arbor, Michigan 48106

The author was born on June 9, 1966 in Kiev, USSR. In September of 1982 he entered Polytechnic University and obtained a BS in June of 1986 and an MS in June of 1988, both in Electrical Engineering. The author started his doctoral studies in Electrophysics in 1988.

\*\*\*\*\*

*To Elina  
and to my parents*

## ACKNOWLEDGEMENTS

I would like to thank my advisor Professor D. A. Davids for the immense amount of help, inspiration and enlightenment that he has provided through my entire graduate work.

I am deeply thankful to Professor H. L. Bertoni for all the encouragement and guidance throughout my years at the Polytechnic. His help in selection of many of the topics in this work was immeasurable.

I am forever indebted to the faculty of the Polytechnic for the education and knowledge that I have received.

I would also like to acknowledge Walter Honcharenko for his help and advice in preparation of the manuscript.

Finally, I would like to thank the US Air Force for providing the funding for this work, which was supported under contracts F 49620-86-C-0217/SB5861-0436 and AFSD-SCEEE 4-25126 .



# **AN ABSTRACT**

## **SURFACE CHARACTERIZATION USING THE RESTRICTED APERTURE ACOUSTIC MICROSCOPE**

**by**

**Dmitry Chizhik**

**Advisor: Douglas A. Davids**

**Submitted in Partial Fulfillment of the Requirements  
for the Degree of Doctor of Philosophy ( Electrophysics)**

**May 1991**

A scanning acoustic microscope that uses a novel lens having a slot-shaped aperture is used to investigate the quantitative measurements of properties of isotropic and anisotropic materials and also the characterization of surface- breaking cracks. The slot lens has a point focus and yet launches leaky Rayleigh waves in preferential directions. This allows surface wave velocity measurements of anisotropic materials as well as interrogation of cracks at nearly normal incidence for determination of the crack reflection coefficient. Such a lens can also be used for imaging of polycrystalline material surfaces where contrast depends solely on Rayleigh-wave anisotropy. Diffraction-corrected geometric theory is employed to model the response of both the slot and circular aperture lenses to cracked as well as defect-free sample surfaces. Experimental measurements were made to test the theoretical predictions.

## Table of Contents

<b>Chapter I. Introduction.....</b>	<b>1</b>
1.1 Acoustic microscope.....	1
1.2 The $V(z)$ measurement.....	4
1.3 The $V(x)$ measurement.....	4
1.4 The slot lens.....	8
 <b>Chapter II. Theoretical Modelling of the <math>V(z)</math></b>	
<b>for the Circular Aperture Lens.....</b>	<b>11</b>
2.1 The angular spectrum approach.....	11
2.2 The Ray approach.....	17
2.2.1 The geometric component $V_G(z)$ .....	17
2.2.2 The leaky component $V_L(z)$ .....	20
2.2.3 The total voltage $V(z)$ .....	21
2.3 Diffraction correction to the ray model.....	24
2.3.1 Introduction.....	24
2.3.2 Approximation of phase variation of field $U(\rho)$ .....	25
2.3.3 Approximation of amplitude variation of field $U(\rho)$ .....	30
2.3.4 Calculation of the transducer response $V_G(z)$ .....	31
2.3.5 Calculation of the leaky contribution $V_L(z)$ .....	36
2.3.6 Calculation of the total transducer response $V(z)$ .....	41
2.4 Extraction of the Rayleigh velocity $v_R$ from the $V(z)$ .....	44

### **Chapter III. Theoretical Modelling of $V(z)$ for the Slot Lens**

Acoustic Microscope.....	49
3.1 The angular spectrum approach.....	49
3.2 The Ray approach.....	52
3.2.1 Calculation of the specularly reflected contribution $V_G(z)$ .....	52
3.2.2 Calculation of the leaky contribution $V_L(z)$ .....	53
3.2.3 The total voltage $V(z)$ .....	54
3.3 Extracting $v_R(\phi)$ of an anisotropic material using the slot lens.....	57

### **Chapter IV. Modelling of $V(z)$ Measurements across a surface breaking crack using the ray theory.....**

4.1 Specularly reflected component $V_G(z)$ .....	64
4.2 Transmitted component $V_T(x, z)$ .....	64
4.3 Reflected surface wave contribution $V_{refl}(x)$ .....	74
4.4 The total voltage response $V(x, z)$ .....	90

### **Chapter V. Experimental Measurement of $V(x)$ .....**

5.1 Experimental measurement of $V(x)$ .....	94
5.2 Extracting the surface wave reflection coefficient of a crack from $V(x)$ measured using the slot lens.....	100

### **Chapter VI. Conclusions.....**

Appendix A.....	108
Appendix B. ....	115
References.....	116

## Table of Figures

1.1 Reflection mode acoustic microscope with sample at focus.....	2
1.2 Ray diagram of the acoustic lens, defocused toward the sample, showing the specularly reflected axial ray and the excited and re-radiated leaky surface rays.....	3
1.3 Measured transducer output voltage $V$ as a function of defocus distance $z$ for a glass sample and a circular aperture lens.....	5
1.4 Rayleigh wave interaction with a crack. A surface wave normally incident on the crack from the left results in reflected and transmitted surface waves propagating away from the crack.....	6
1.5 Measured transducer output voltage $V$ as a function of lateral displacement $x$ for a glass slide containing a deep surface breaking crack at $x = 0$ .....	7
1.6 Slot aperture acoustic lens.....	9
2.1 $V(z)$ of Teflon for a circular aperture lens: observed (solid) and calculated using the angular spectrum approach (dotted).....	13
2.2 $V(z)$ of glass for a circular aperture lens: observed (solid) and calculated using the angular spectrum approach (dotted).....	14

2.3	V(z) of Teflon calculated using (a) $T_{WL}(z)$ (solid) and (b) assuming $T_{WL}(z) = T_{WL}(z = 0)$ .....	16
2.4	V(z) of Teflon for a circular aperture lens: observed (solid) and calculated using the geometric ray approach (dotted).....	19
2.5	Cross-sectional view of the lens showing a bundle of leaky rays forming a focus in the lens rod.....	22
2.6	V(z) of glass for a circular aperture lens: observed (solid) and calculated using the geometric ray approach (dotted).....	23
2.7a	Amplitude profile of field $U(\rho)$ illuminating the back focal plane. Calculated using the theory of Tjotta and Tjotta [12].....	27
2.7b	Relative phase profile of field $U(\rho)$ illuminating the back focal plane. Calculated using the theory of Tjotta and Tjotta [12].....	28
2.8	Angular deviation $\theta$ from the vertical of rays illuminating the back focal plane...	29
2.9	Amplitude profile of effective field $U_{eff}(\rho)$ illuminating the back focal plane: (a) Calculated using the theory of Tjotta and Tjotta [12] (solid) and (b) two-Gaussian fit (dashed).....	32
2.10	Ray structure for specularly reflected component $V_G$ for $z < 0$ .....	33

<b>2.11</b>	<b>V(z) of Teflon for a circular aperture lens calculated using</b>	
	(a) the angular spectrum approach (solid) and	
	(b) the diffraction-corrected ray approach (dotted).....	37
<b>2.12</b>	<b>V(z) of Teflon for a circular aperture lens: observed (solid) and calculated</b>	
	using the diffraction-corrected ray approach (dotted).....	38
<b>2.13</b>	<b>V(z) of Teflon for a circular aperture lens: (a) observed (solid),</b>	
	(b) calculated using the diffraction-corrected ray approach (dashed) and	
	(c) calculated using the geometric ray theory (dotted).....	39
<b>2.14</b>	<b>Calculated leaky contribution <math>V_L(z)</math> for glass.....</b>	40
<b>2.15</b>	<b>V(z) of glass for a circular aperture lens: observed (solid) and calculated</b>	
	using the diffraction-corrected ray approach (dotted).....	42
<b>2.16</b>	<b>V(z) of glass for a circular aperture lens calculated using</b>	
	(a) the angular spectrum approach (solid) and	
	(b) the diffraction-corrected ray approach (dashed).....	43
<b>2.17</b>	<b><math>V_I(z)</math> of glass obtained from measured data by</b>	
	$V_I(z) = (V^2(z) - V_G^2(z)) / V_G(z)$ .....	46
<b>2.18</b>	<b>Amplitude of Fourier spectrum of <math>V_I(z)</math> of glass calculated by DFT.....</b>	47
<b>3.1</b>	<b>V(z) of Teflon for a slot aperture lens: observed (solid) and calculated using the</b>	
	angular spectrum approach (dashed).....	50

3.2 V(z) of glass for a slot aperture lens: observed (solid) and calculated using the angular spectrum approach (dashed).....	51
3.3 V(z) of Teflon for a slot aperture lens: observed (solid) and calculated using the diffraction-corrected ray approach (dashed).....	55
3.4 V(z) of glass for a slot aperture lens: observed (solid) and calculated using the diffraction-corrected ray approach (dashed).....	56
3.5 Observed V(z) of Y-cut quartz with slot oriented along the crystalline x-axis ( $\phi = 0$ ).....	58
3.6 Observed V(z) of Y-cut quartz with slot oriented at $90^\circ$ to the crystalline x-axis..	59
3.7 Rayleigh wave velocity $v_R$ of Y-cut quartz as a function of direction of propagation $\phi$ measured from the crystalline x-axis: accepted (solid line) and measured using the slot lens (open boxes).....	60
3.8 $V_I(z)$ of Y-cut quartz obtained from data measured with slot oriented along the crystalline x-axis ( $\phi = 0$ ).....	61
4.1 Surface-wave and specular ray paths for various contributions to V(x,z): (a) transmitted through the crack , (b) reflected from the crack, and (c) specularly reflected from the surface.....	63
4.2 Leaky ray bundle in the x-z plane.....	66

4.3	Distribution of the leaky ray flux (shaded) that excites the transducer, defined on the sample surface. Note also the definition of $\phi_1$ and $\phi_{\max}$ in the sample plane...	67
4.4	Geometry of a surface ray is excited on the left and leaks energy to the right of lens axis. After the ray crosses the crack the leaky field is reduced by the factor $T_c$ ..	68
4.5	Distinct ranges of crack displacement that lead to different geometric relations in determining $Q_R$ :	
	(a) $0 < x < c_{\min}$ ,      (b) $c_{\min} \cos \phi_{\max} < x < c_{\min}$	
	(c) $c_{\min} < x < c_{\max}$ ,      (d) $x > c_{\max}$ .....	70
4.6	Distinct ranges of crack displacement that lead to different geometric relations in determining $Q_L$ : (a) $0 < x < c \cdot \cos \phi_1$ , (b) $c \cdot \cos \phi_1 < x < c$ , (c) $x > c$ .....	73
4.7	Focusing of surface rays reflected from the crack on the (a) left and (b) right side of the Rayleigh circle.....	75
4.8	Divergence of reflected surface waves at the edge of the Rayleigh circle.....	77
4.9	Focus formed in the lens rod by the rays re-radiated along the arc BAC in Fig. 4.8.....	79
4.10	Illumination of the transducer by a bundle of leaky rays, shown in y-z plane, reflected from the crack.....	81
4.11a	Amplitude of $K_1(x)$ calculated for a circular lens.....	83



4.11b	Phase of $K_1(x)$ calculated for a circular lens.....	84
4.12a	Amplitude of $K_1(x)$ calculated for a slot lens.....	85
4.12b	Phase of $K_1(x)$ calculated for a slot lens.....	86
4.13	Surface wave interaction with a crack for $z > 0$ .....	89
4.14	$V(x, z = -400 \mu\text{m})$ calculated for a circular lens.....	91
4.15	$V(x, z = -400 \mu\text{m})$ calculated for a slot lens.....	92
4.16	Variation of amplitude of the crack reflection coefficient $R_c$ with crack depth $d$ normalized to the Rayleigh wavelength $\lambda_R$ for normally incident surface waves ( from Angel and Achenbach [3]).....	93
5.1	$V(x, z = -300 \mu\text{m})$ for a circular aperture lens : observed (solid) and calculated (dotted) (scaled to match at $x = -500 \mu\text{m}$ ).....	95
5.2	$V(x, z = -400 \mu\text{m})$ for a circular aperture lens : observed (solid) and calculated (dotted).....	96
5.3	$V(x, z = -346 \mu\text{m})$ for a slot aperture lens : observed (solid) and calculated (dotted).....	97

5.4 $V(x, z = -474 \mu\text{m})$ for a slot aperture lens : observed (solid) and calculated (dotted).....	98
5.5 Selected surface wave paths on the sample surface at $z < 0$ containing a crack parallel to the y-axis at $x = 0$ .....	99
5.6 (a) Calculated $V(x, z = -346 \mu\text{m})$ for a slot aperture lens (solid) and (b) $\cos(2k_R x)$ function ( dashed).....	102
A.1.....	109
A.2.....	110
A.3.....	113
A.4.....	114
B.1 Lens dimensions.....	115

## Chapter I

### Introduction

#### 1.1 Acoustic microscope

The acoustic microscope used in this work consists of a fused quartz lens rod which has a transducer bonded to one end and a concave spherical lens ground in the other end (Fig. 1.1). To make a measurement at a particular location, a tone-burst signal of 49 MHz and 0.5  $\mu$ sec duration is applied to a piezoelectric transducer. The transducer excites a compressional acoustic wave which travels down the lens rod. The curved surface of the lens causes focusing in the coupling fluid (usually water) at or near the surface of the sample. The resulting incident wave travels as a conical beam, thus illuminating the sample with rays that cover a wide range of angles. The tone-burst signal reflected from the surface of the sample, which now contains information about the sample, is refracted at the lens surface into the lens rod and ultimately excites the same transducer. Time-gating is employed in the receiver circuit to isolate the desired echo signal and exclude internal rod reverberations and other undesired signals that may be present. The lens can be mechanically scanned along any of the three axis, thus allowing various types of measurements, including imaging, to be performed.

It has been shown by Weglein [1], Bertoni [2], and others that when the focal point of the lens lies below the sample surface, the signal returning from the sample can be viewed as consisting of two contributions: a geometrically scattered part and a leaky wave part. The geometric contribution results from specular reflection from the sample surface. The leaky contribution results from those incident rays that strike the sample at the Rayleigh critical angle, thus launching Rayleigh surface waves which propagate along the sample surface and radiate (leak) energy back into the water in the form of P-waves ( Fig.1.2). Some of these leaked rays are refracted by the lens toward the

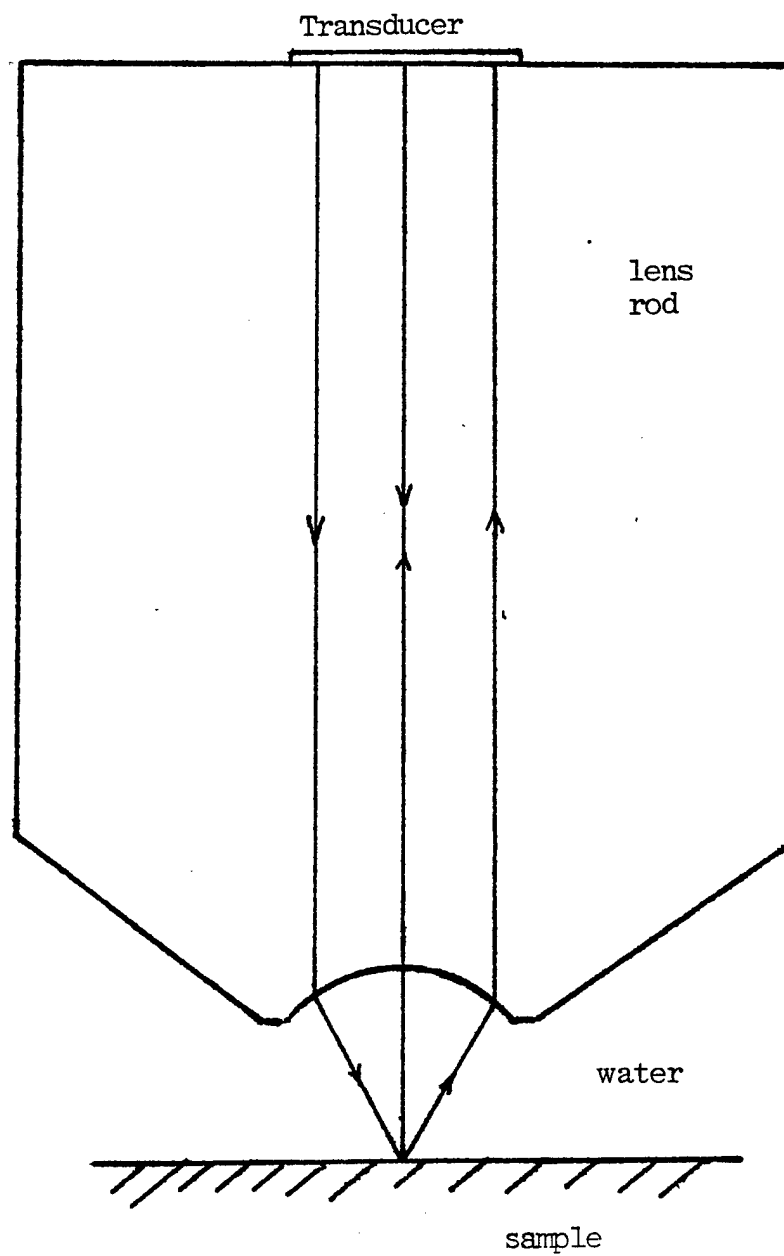


**Fig. 1.1** Reflection mode acoustic microscope with sample at focus.

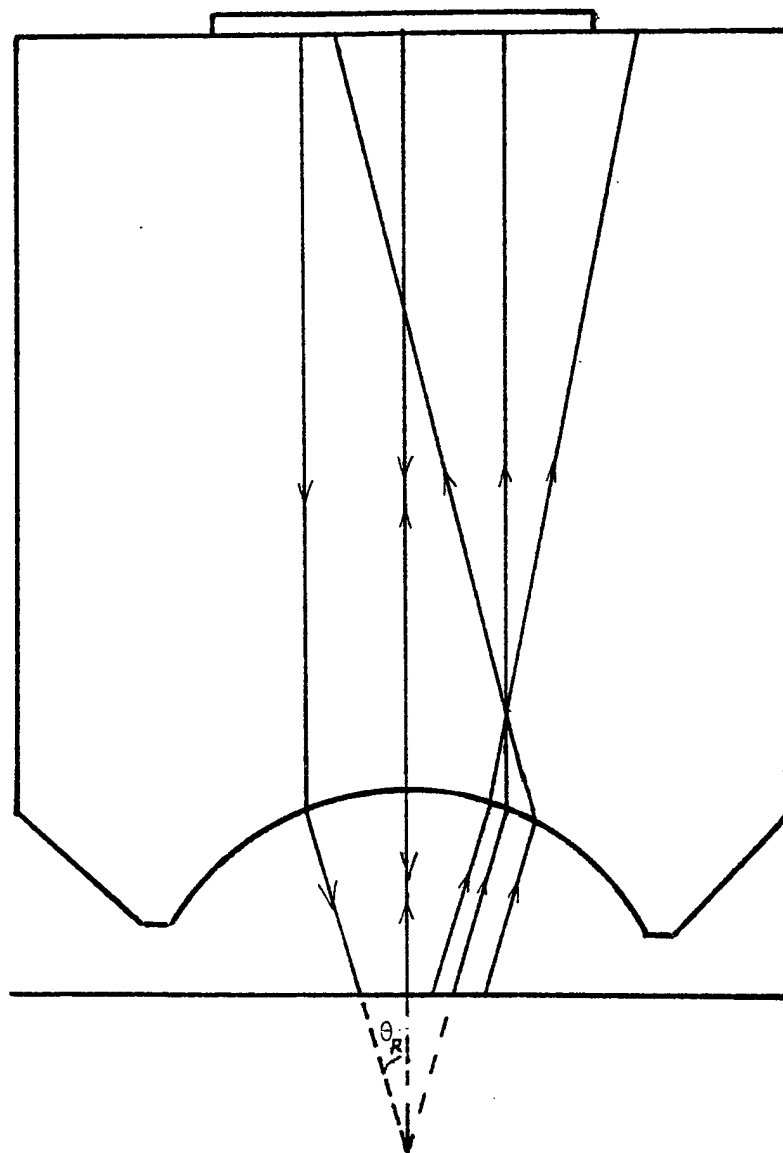


**Fig. 1.2** Ray diagram of the acoustic lens, defocused toward the sample, showing the specularly reflected axial ray and the excited and re-radiated leaky surface rays.

transducer where they become part of the total transducer voltage.

## 1.2 The $V(z)$ measurement

An important type of measurement, called the acoustic material signature or  $V(z)$ , involves the variation in amplitude of the signal reflected from the sample surface as the lens is defocused toward the sample along the vertical or  $z$ -axis. The defocus distance  $z$  is measured from the front focal plane of the lens. The rays comprising the geometric and leaky contributions travel along different paths which results in the two components arriving at the transducer with different phases. This phase difference is a function of  $z$ , which leads to an interference pattern in  $V(z)$  resulting from the geometric and leaky contributions gradually going in and out of phase as the lens-sample separation is varied. A typical  $V(z)$  measurement made using as a sample a glass microscope slide is shown in Fig. 1.3. The separation between local minima is directly related to the Rayleigh wave velocity, which can thus be extracted from the  $V(z)$ . This velocity is strongly dependent upon the elastic properties of the sample and thus the  $V(z)$  measurement becomes a valuable tool in the evaluation of material properties .

## 1.3 The $V(x)$ measurement

Another important type of measurement, called  $V(x)$ , records the transducer voltage as the lens is scanned laterally at constant defocus height  $z$  above the sample. When the sample surface contains a discontinuity, such as a thin crack, the transducer voltage is altered since the defect may interfere with the surface wave propagation. The usual leaky contribution is reduced and another contribution to the total detected signal arises due to the surface waves that are scattered from the crack. Some of the rays reflected from the crack or transmitted through it are shown in Fig. 1.4. The strength of

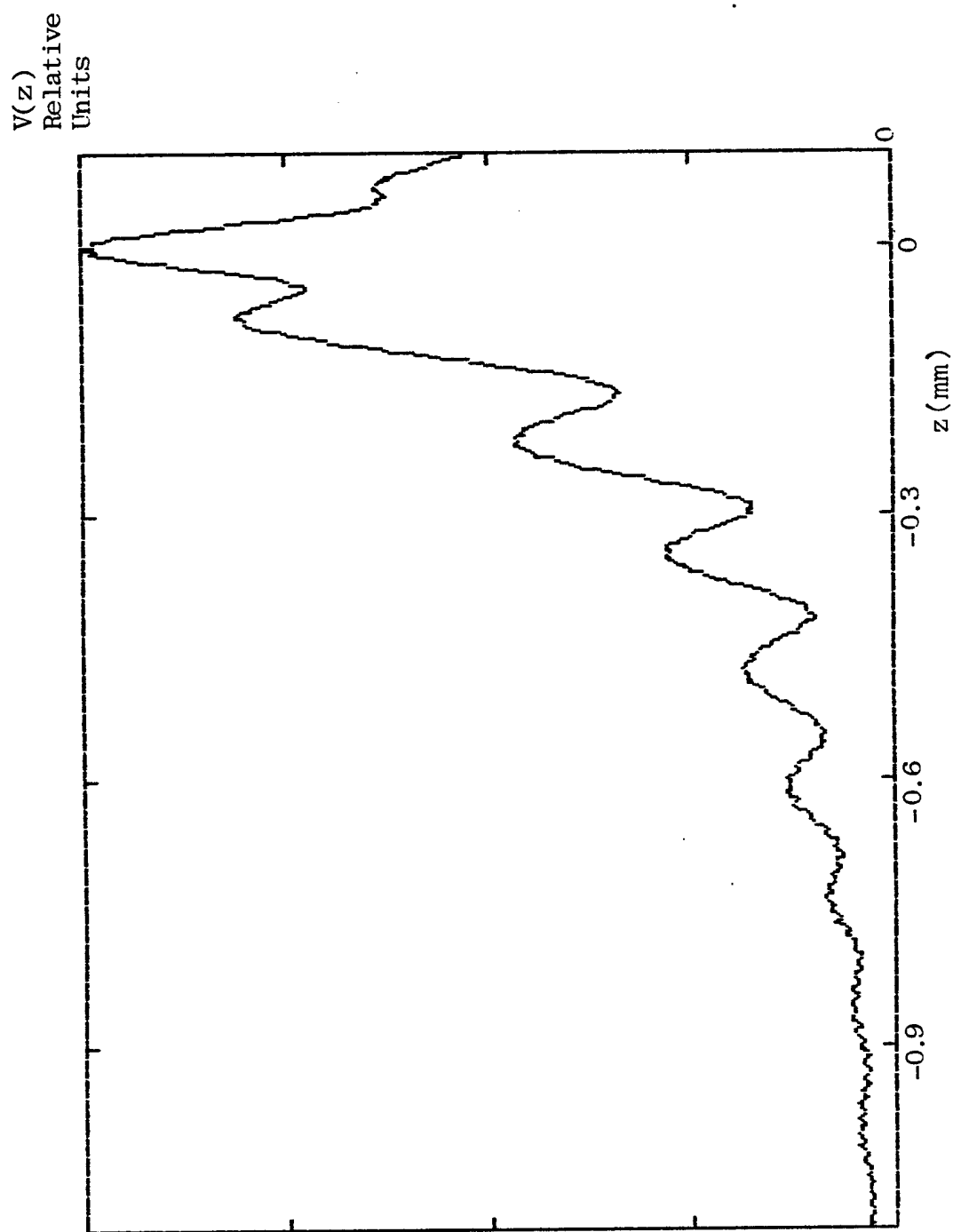


**Fig. 1.3** Measured transducer output voltage  $V$  as a function of defocus distance  $z$  for a glass sample and a circular aperture lens

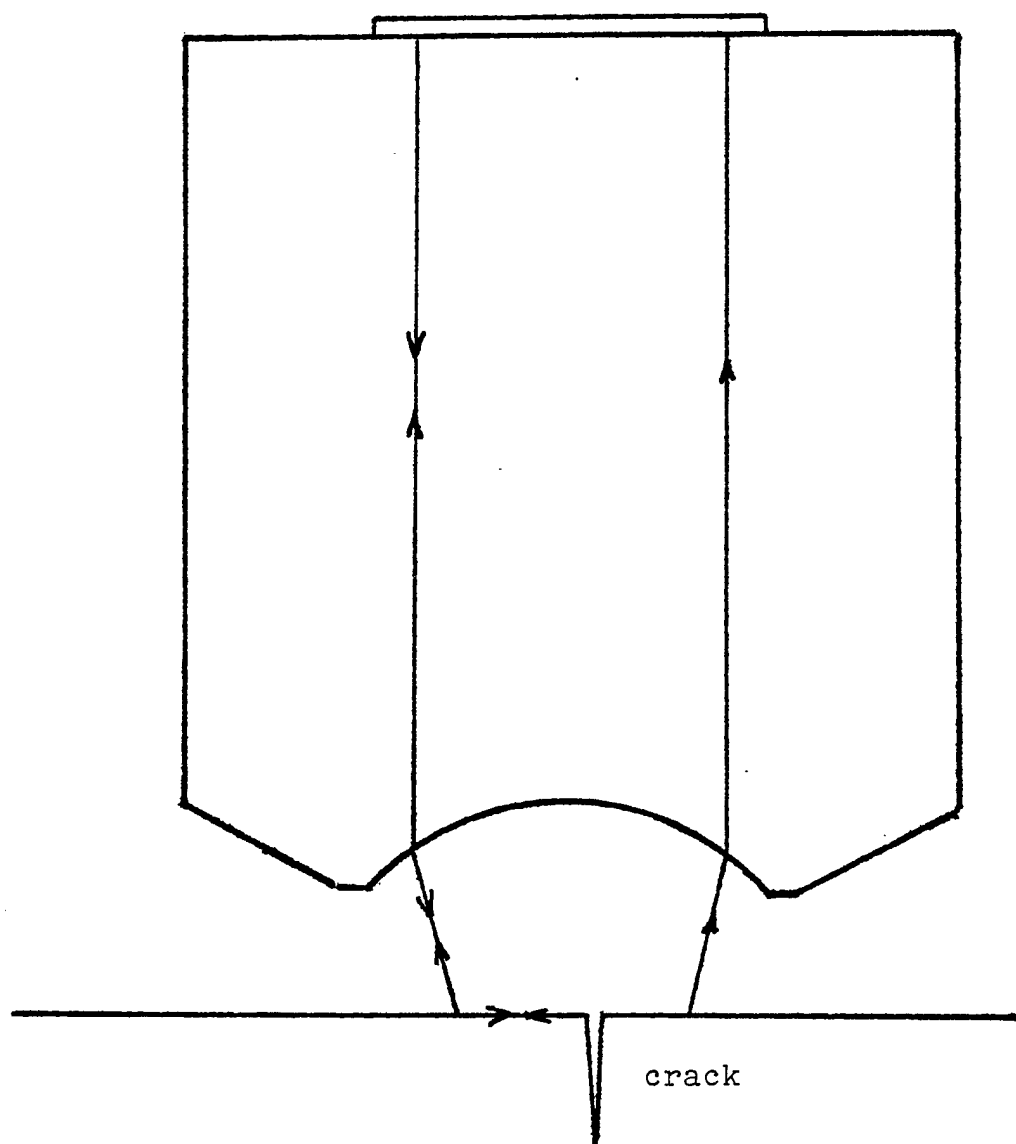


**Fig. 1.4** Rayleigh wave interaction with a crack. A surface wave normally incident on the crack from the left results in reflected and transmitted surface waves propagating away from the crack.



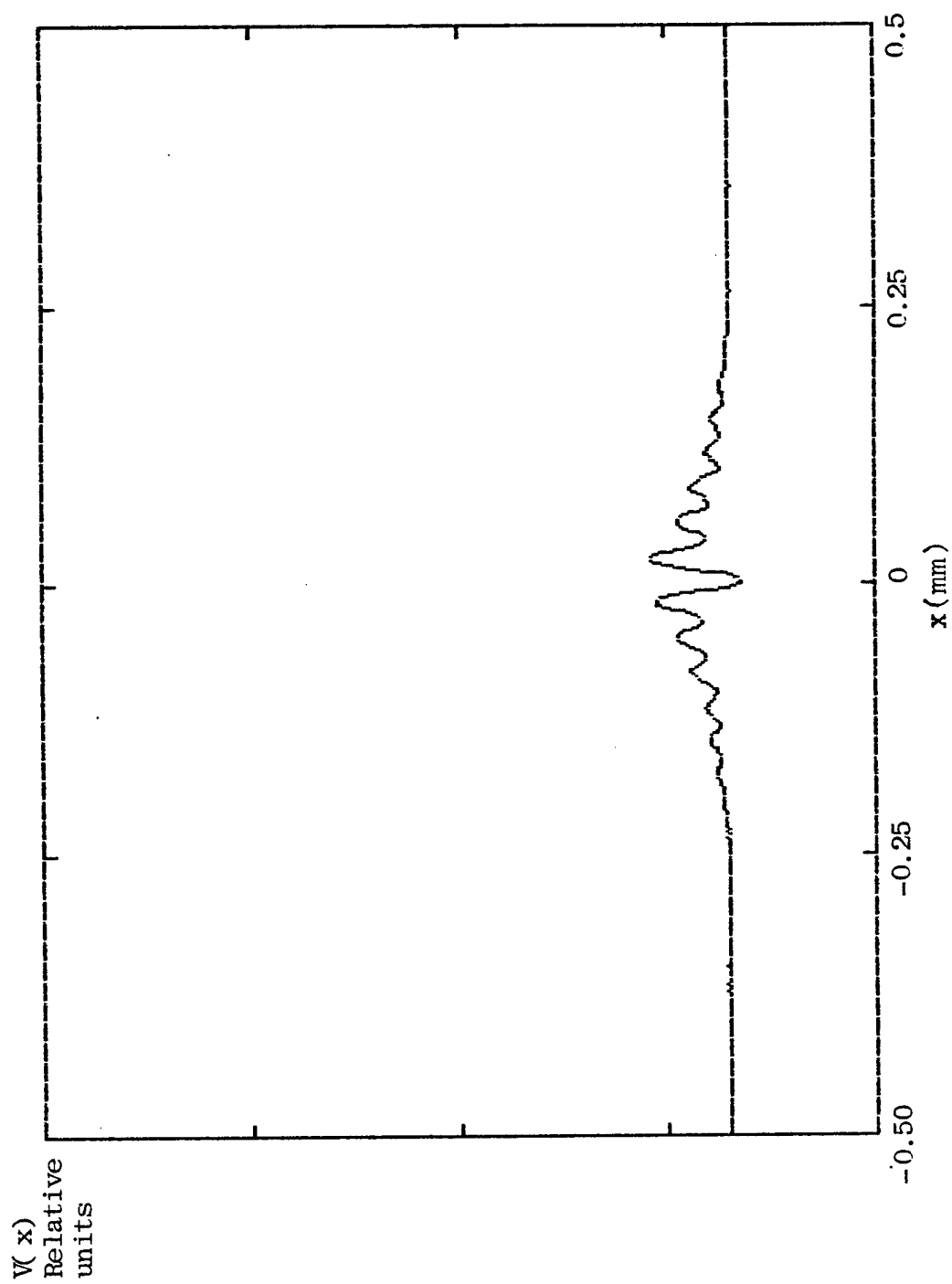


**Fig. 1.5** Measured transducer output voltage  $V$  as a function of lateral displacement  $x$  for a glass slide containing a deep surface breaking crack at  $x = 0$ .

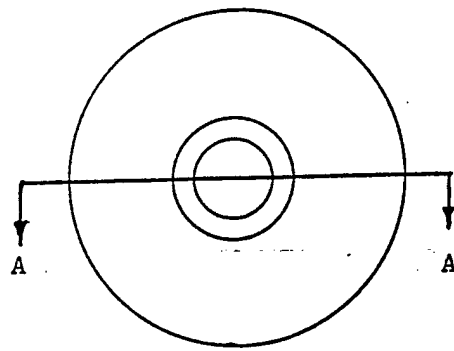
the scattered signal is directly proportional to the crack surface reflection coefficient. The propagation path length of the component scattered from the crack varies with crack displacement  $x$ . This results in interference between this component and the geometric contribution, whose phase remains constant for all  $x$ . A typical  $V(x)$  measurement of a cracked glass slide is displayed in Fig. 1.5. Angel and Achenbach [3] have shown that the surface wave reflection coefficient  $R_c$  at the crack is related to crack depth. Thus if  $R_c$  is determined from  $V(x)$ , it may be possible to determine the crack depth, which is of interest to non destructive evaluation (NDE).

#### 1.4 The slot lens

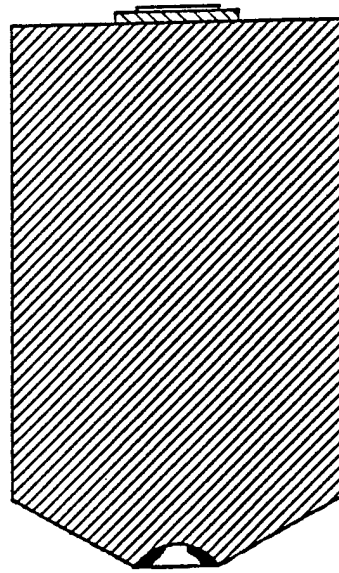
Conventionally, a point-focus lens with a circular aperture is used for  $V(z)$  measurements. When this type of lens is defocused toward a sample, surface waves are launched in all directions on the sample surface which makes this lens unsuitable for meaningful measurements of anisotropic materials as the Rayleigh wave velocity varies with the direction of propagation. In addition, a circular lens cannot readily be used to measure surface wave reflection coefficient of cracks, since this coefficient is also strongly dependent on the angle of incidence of the surface wave with the crack.

A line-focus (cylindrical) lens has been used by Kushibiki, et. al. [4] with anisotropic materials to launch surface waves along a particular direction of the sample surface. However, since it focuses to a line and not a point, it has good resolution in only one direction and is thus unsuitable for imaging polycrystalline materials. This lens can also be used for determination of the crack reflection coefficient, however, again, its poor lateral resolution requires a very long straight uniform crack which may not be feasible experimentally or encountered in practice.

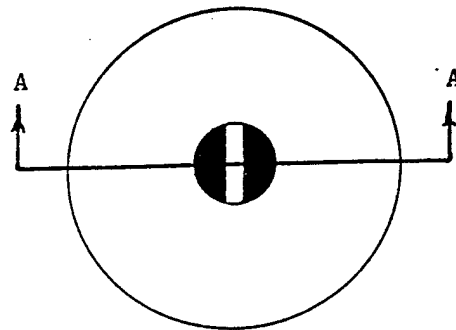
To conduct measurements of anisotropic crystalline materials, graphite-epoxy composites, as well as defect characterization, a new kind of lens was proposed [5]. In a



Top View



Section A-A



Bottom View

**Fig. 1.6** Slot aperture acoustic lens

novel approach, part of the aperture of the new lens was blocked by an acoustically absorbent material so as to leave only a slot-shaped aperture exposed. This lens, called the slot lens (Fig. 1.6), can launch and receive leaky surface waves only along a narrow range of directions, thus allowing anisotropy measurements to be performed, with only somewhat degraded resolution. It can also be used to interrogate short cracks under nearly normally incident conditions which allows the determination of the crack reflection coefficient, and thus, possibly, the crack depth.

To assess the lens performance it is necessary to have a theoretical model to be able to predict the lens response to both cracked and defect-free surfaces. Atalar [6] used the angular spectrum method to develop a theory for predicting  $V(z)$ . It takes into account field diffraction both in the lens rod and in water and treats the concave surface of the lens as a thin lens. Bertoni [2] has proposed an alternate approach that uses geometrical ray techniques to model the microscope. While the latter theory ignores the effects of diffraction which produces poor agreement near focus, it provides a more physical visualization as well as computationally simpler approach.

It is also important to model the  $V(x)$  for the purpose of extracting the crack surface wave reflection coefficient. Somekh, et. al. [ 7] extended Atalar's [6] approach to cracked surfaces measured with a cylindrical lens. Ahn, et. al. [8] have used a Green's function solution implemented by numerical boundary element method. None of these approaches involve the reflection coefficient of the crack in a simple way that permits a direct determination of this coefficient.

In this work geometrical ray techniques are extended to include diffraction effects in the lens rod and are used to model the  $V(z)$  and the  $V(x)$  for both circular and slot aperture lenses. A simple technique is developed to extract the crack reflection coefficient from the  $V(x)$ .

## Chapter II

### Theoretical modelling of the $V(z)$ for the circular aperture lens

A review of two theoretical models that predict  $V(z)$  for a circular aperture lens are presented: the angular spectrum approach of Atalar [6] and the ray method of Bertoni [2]. A modification of the ray method is then proposed that accounts for diffraction effects in the lens rod. Finally, a method of extracting the Rayleigh wave velocity from the  $V(z)$  is described.

#### 2.1 The angular spectrum approach

The following is a brief overview of the angular spectrum model of the microscope  $V(z)$  response, as developed by Atalar [6].

The transducer radiates an acoustic field  $u_0^+(x,y)$  that propagates down the lens rod, undergoes diffraction and is defined at the back focal plane of the lens as the field  $u_1^+(x,y)$ . A crucial assumption is that the spherical lens is assumed to be thin and, thus, the field  $u_2^+(x,y)$  at the front focal plane may be expressed in terms of the Fourier transform of  $u_1^+(x,y)$ . The phase variation produced in propagating from the front focal plane to the plane of the sample, located a distance  $z$  from the front focal plane is included by multiplying the angular spectrum of the field  $u_2^+(x,y)$  by the phase factor  $\exp(i k_z z)$ . The resultant angular spectrum is multiplied by the water-sample reflection coefficient  $R(k_x, k_y)$  and multiplied again by the above phase factor, which results in the reflected spectrum  $U_2^-(k_x, k_y)$  at the front focal plane. The field  $u_2^-(x,y)$  is then Fourier transformed again to obtain the reflected field  $u_1^-(\rho)$  at the back focal plane. The transducer response voltage  $V$  is found by integrating the product of the acoustic fields defined at the back focal plane, i.e.

$$V(z) = \int_{-\infty}^{\infty} \int_{-\infty}^{\infty} u_1^+(x,y) u_1^-(x,y) dx dy \quad (2.1.1)$$

Substituting  $u_1^-(x,y)$  found by carrying out the above steps leads to

$$V(z) = \int_{-\infty}^{\infty} \int_{-\infty}^{\infty} u_1^-(x,y) u_1^-( -x, -y) \mathcal{R}(k_x, k_y) P_1(x,y) P_2(x,y) \exp(i2k_z z) dx dy \quad (2.1.2)$$

In evaluating the above integral,  $k_x$ ,  $k_y$  and  $k_z$  are expressed in terms of  $x$  and  $y$  by using the following relations

$$\begin{aligned} k_x &= k_w \sin \theta \cos \phi \\ k_y &= k_w \sin \theta \sin \phi \\ k_z &= k_w \cos \theta \\ \rho &= \sqrt{x^2 + y^2} \\ \theta &= \tan^{-1} \rho / (f - R + \sqrt{R^2 - \rho^2}) \\ \phi &= \tan^{-1} y / x \end{aligned}$$

In these relations  $k_w$  and  $f$  are the wavenumber and focal length, respectively, in water, and  $R$  is the lens radius of curvature. The pupil functions  $P_1(x,y)$  and  $P_2(x,y)$  account for two-way propagation through the lens aperture, and include both the finite extent of the aperture as well as the lens-water and water-lens transmission coefficients  $T_{LW}$  and  $T_{WL}$ , respectively. In the usual Fourier optics approximation [9], these functions are evaluated at the lens aperture and projected onto the back focal plane in unmodified form, thus neglecting diffraction effects on the pupil functions between these two planes.

The expression (2.1.2) for  $V(z)$  can be evaluated numerically. The results of such calculations are plotted against  $z$  in Fig. 2.1 and 2.2 for teflon and glass samples,

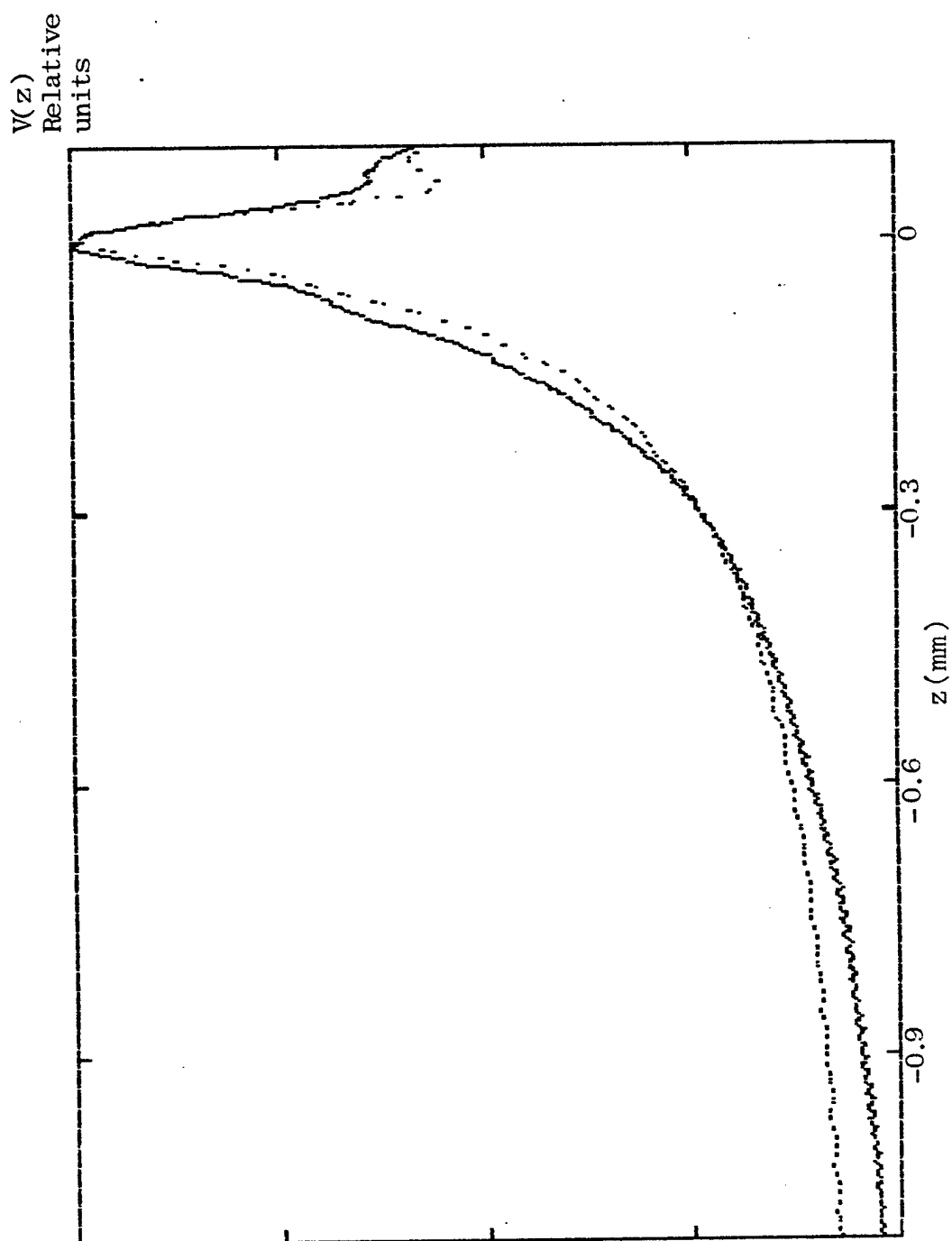


**Fig. 2.1**  $V(z)$  of Teflon for a circular aperture lens: observed (solid) and calculated using the angular spectrum approach (dotted).

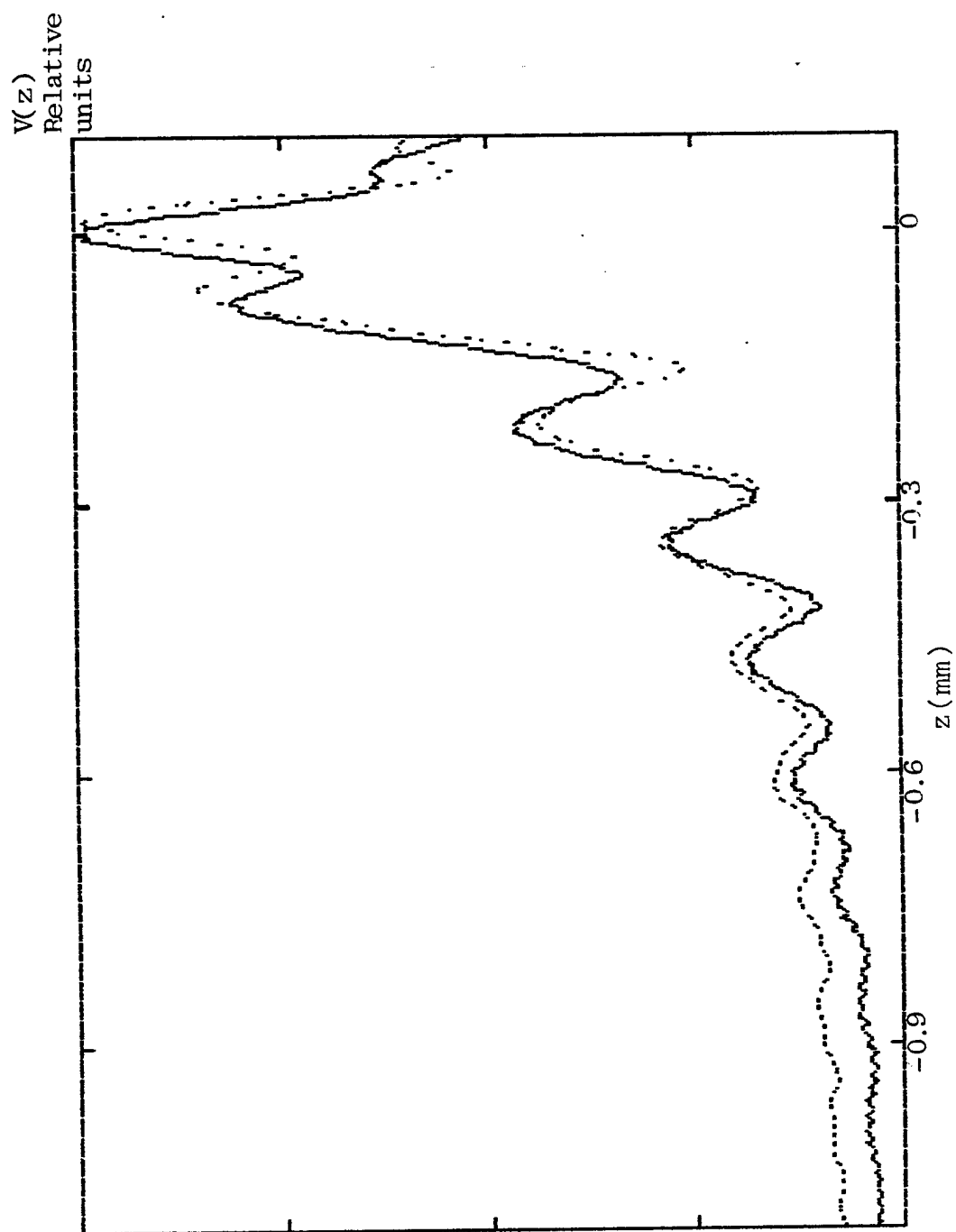


**Fig. 2.2**  $V(z)$  of glass for a circular aperture lens: observed (solid) and calculated using the angular spectrum approach (dotted).



respectively. The water-teflon interface does not support surface waves, while the water-glass interface does, as is evidenced by the interference-like structure in its  $V(z)$ . Comparisons are made with the measured values for these materials in Fig. 2.1 and 2.2 .

Strictly,  $T_{WL}$  is also a function of sample defocus  $z$ , as the transmission coefficient depends on the angular spectrum of the reflected field. In Fig. 2.3 a  $V(z)$  for teflon calculated using  $T_{WL}(z)$  is compared with a  $V(z)$  calculated while assuming  $T_{WL}(z) = T_{WL}(z=0)$ . As the  $z$  variation of  $T_{WL}$  apparently does not significantly effect the  $V(z)$ ,  $T_{WL}(z=0)$  will be used for all  $z$ , This simplification was used in producing Fig. 2.1 and 2.2. Both  $T_{LW}$  and  $T_{WL}$  are calculated using the method of acoustic equivalent networks for planar interfaces by Oliner, et. al. [10].

While the angular spectrum approach gives impressively good agreement with the experimental results, it is difficult to gain intuitive insight into the physical processes involved in determination of  $V(z)$  from the integral (2.1.2).

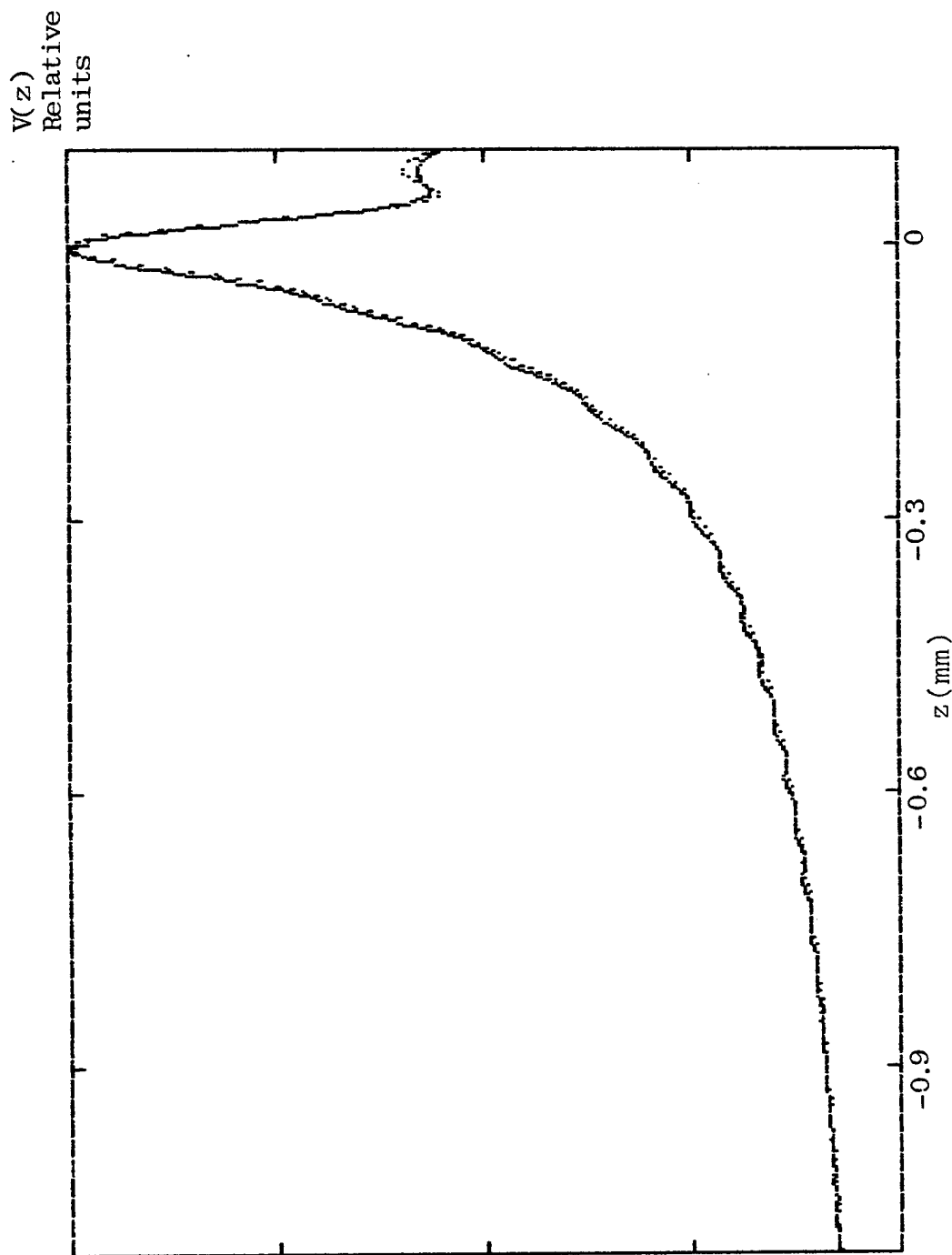


Fig. 2.3  $V(z)$  of Teflon calculated using (a)  $T_{WL}(z)$  (solid) and  
 (b) assuming  $T_{WL}(z) = T_{WL}(z = 0)$ .

## 2.2 The Ray approach

The following is a brief overview of the ray model of the  $V(z)$ , as developed by Bertoni [2].

The methods of ray optics used here are well described by James[11]. To conserve power, the field amplitude for spherically convergent or divergent beams varies inversely as the square root of the cross-sectional area of the beam. For cylindrically focussed beams this variation becomes inversely proportional to the square root of the distance from the focus. Furthermore, while propagating through focus, the beam suffers a phase change of  $-\pi$  for spherical (point) focus, and  $-\pi/2$  for a cylindrical focus.

The transducer response voltage  $V(z)$  consists of two parts: the specular (geometric) contribution  $V_G(z)$  and the leaky contribution  $V_L(z)$

$$V(z) = V_G(z) + V_L(z). \quad (2.2.1)$$

These two components are modelled separately:

### 2.2.1 The geometric component $V_G$

Neglecting diffraction, the transducer illumination of the back of the lens is a uniform compressional acoustic field. Assuming axial symmetry, the field returning from the sample and striking the plane of the transducer is found to be:

$$-T_{LW} T_{WL} R(0) \exp(i2k_w(D/n+f+z)) \frac{|f|}{|f+2z| |D-u|} \exp\left[\frac{ik_w \rho^2}{2n(D-u)}\right], \quad (2.2.2)$$

where  $u = f(f+2z)/2nz$ ,  $D$  is the distance between the transducer and the lens aperture,  $n$  is lens material index of refraction relative to water ( $n = v_l/v_w$ ), and  $f$  is the lens focal

length in water, which can be expressed in terms of the lens radius of curvature R

$$f = \frac{nR}{n-1} \quad (2.2.3)$$

The lens transmission coefficients  $T_{LW}$  and  $T_{WL}$  as well as the sample reflection coefficient  $\mathcal{R}$  are assumed here to be constant for all angles of incidence. The derivation of (2.2.2) will be considered in more detail in the next section. The voltage  $V_G$  is obtained by integrating the field (2.2.2) over the transducer and normalizing by the transducer area, resulting in

$$V_G = -T_{LW} T_{WL} \mathcal{R}(0) \exp [i 2 k_w (D/n+f+z)] \frac{2\pi n(D-u)}{i k_w} \cdot \left[ \exp \frac{i k_w r_T^2}{2n(D-u)} - 1 \right] / \pi R_T^2 \quad (2.2.4)$$

where

$$\begin{aligned} r_T &= R_a, & z_{\min} > z \text{ or } z > z_{\max} \\ &= R_a(1 - 2z(nD - f)/f^2), & z_{\min} < z < 0 \\ &= R_a |D-u|/u, & 0 < z < z_{\max} \end{aligned} \quad (2.2.5)$$

$$z_{\min} = - \frac{f^2 (R_T/R_a - 1)}{2n(D-f/n)} \quad [2.2.6]$$

$$z_{\max} = \frac{f^2 (1+R_T/R_a)}{2n[D-(1+R_T/R_a)f/n]} \quad .$$

Here  $R_a$  is the aperture radius. The expression (2.2.4) was evaluated numerically for a

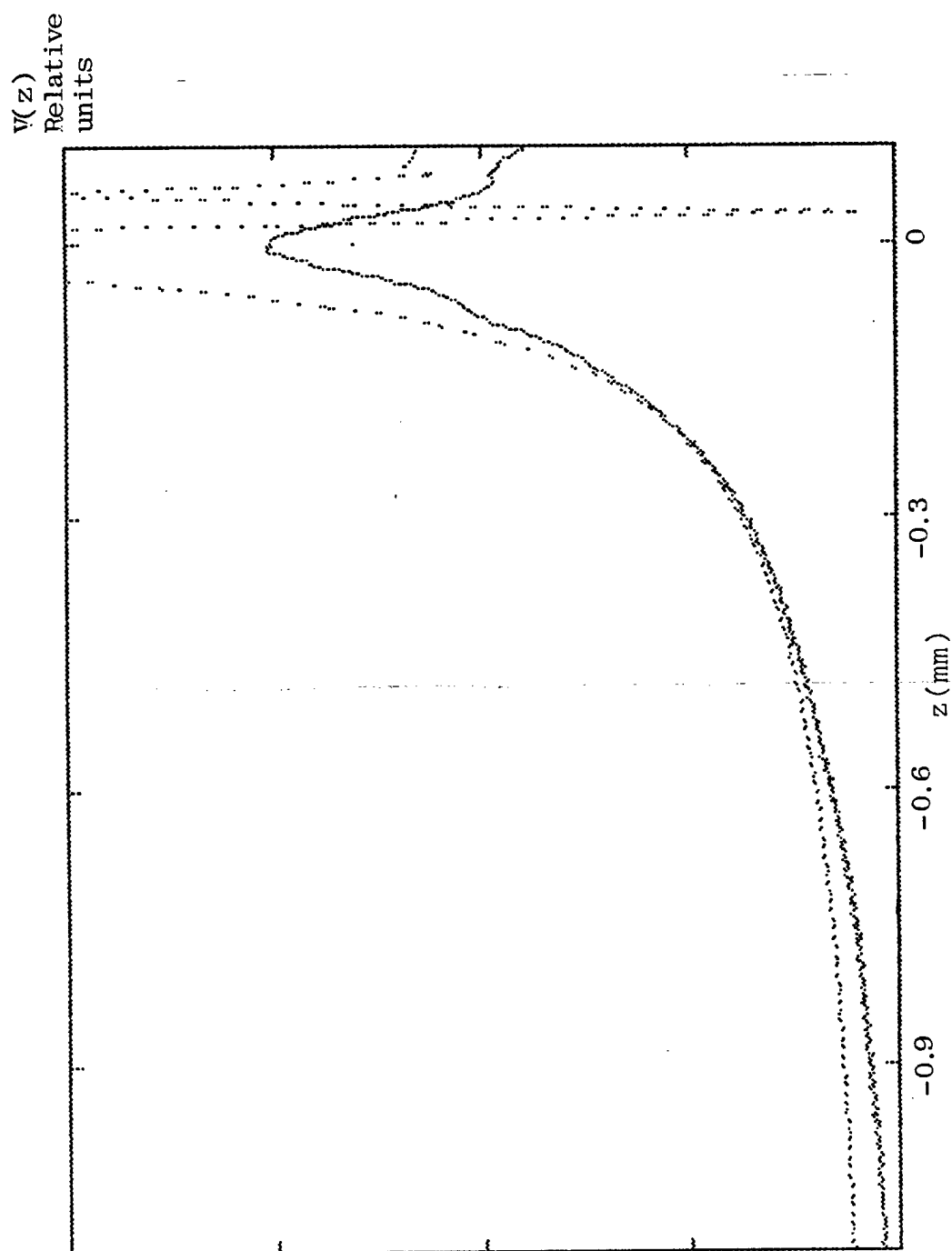


**Fig. 2.4**  $V(z)$  of Teflon for a circular aperture lens: observed (solid) and calculated using the geometric ray approach (dotted).

teflon sample and plotted in Fig. 2.4 along with the measured  $V(z)$  of teflon. Since Rayleigh waves cannot be excited on teflon from the water, there is no leaky contribution. One may observe in Fig. 2.4 that the agreement with the experiment deteriorates as  $|z|$  approaches focus as is expected when diffraction is neglected.

### 2.2.2 The leaky component $V_L(z)$

First, the behavior of  $V_L(z)$  for distances closer than geometric focus ( $z < 0$ ) is considered. Leaky waves are excited by rays that are incident on the sample surface at angle  $\theta_R$  or, equivalently, strike the lens surface at  $\rho = \rho_R$  (derived in Appendix A), from the lens axis, as shown in Fig. 2.5. The resulting surface wave propagates along the surface leaking a parallel family of rays at  $\theta_R$  with respect to the normal to the surface. Since the lens is axially symmetric, these leaky waves are launched in all directions on the sample surface passing through the center of symmetry defined by the lens axis. This center of symmetry thus becomes a cylindrical focus for the surface waves. In any radial plane, one of the leaked rays, called the principal ray, radiates in such a way as to cross the lens aperture plane at  $\rho = \rho_T$  and travel to the transducer along a path that is the mirror image of the incident ray. A bundle of rays neighboring the principal ray focus to a point in the radial plane located in the lens rod a distance  $f_x$  (derived in Appendix A) above the aperture. Due to the symmetry of the system with respect to the lens axis ( $z$ ) the entire family of leaky rays forms a ring focus of radius  $\rho_R$  between the lens surface and the transducer. The response voltage  $V_L$  is obtained by integrating the resulting field over the transducer and normalizing to the transducer area, resulting in

$$V_L = - T_{LW} T_{WL} \exp(i2k_w(D/n+f)) \left[ \frac{2\alpha_L \lambda_w (\sqrt{\pi} f^3 \sin \theta_R)^{1/2}}{(n \lambda_w D)^{3/4}} \right] e^{i\pi \cdot K} \cdot \exp(i2k_w(D/n+f+|z|\cos\theta_R)) \cdot \exp(-2\alpha_L |z| \tan \theta_R), \quad (2.2.7)$$

where

$$K = \frac{2e^{-i\pi/4}}{N_T^2} \int_0^{N_T} [\exp i(N-N_R)^2 + \exp(-i\pi/2) \exp i(N+N_R)^2] \sqrt{N} dN \quad (2.2.8)$$

In (2.2.8),

$$N_T = \sqrt{\frac{k_w}{2nD}} R_T \quad \text{and} \quad N_R = \sqrt{\frac{k_w}{2nD}} \rho_R.$$

The expressions (2.2.7) and (2.2.8) can be evaluated numerically to yield  $V_L(z)$  for  $z < 0$ .

For  $z > 0$  the leaky rays miss the transducer and, therefore:

$$V_L(z) = 0 \quad \text{for } z > 0. \quad (2.2.9)$$

### 2.2.3 The total voltage $V(z)$

The total voltage  $V(z)$  is found by adding  $V_G$  and  $V_L$ . The result of such calculation for a glass sample is compared in Fig. 2.6 with the measured  $V(z)$ . It is seen that, as in the case of teflon (Fig. 2.4), the agreement with the experiment deteriorates as  $|z|$  approaches focus.

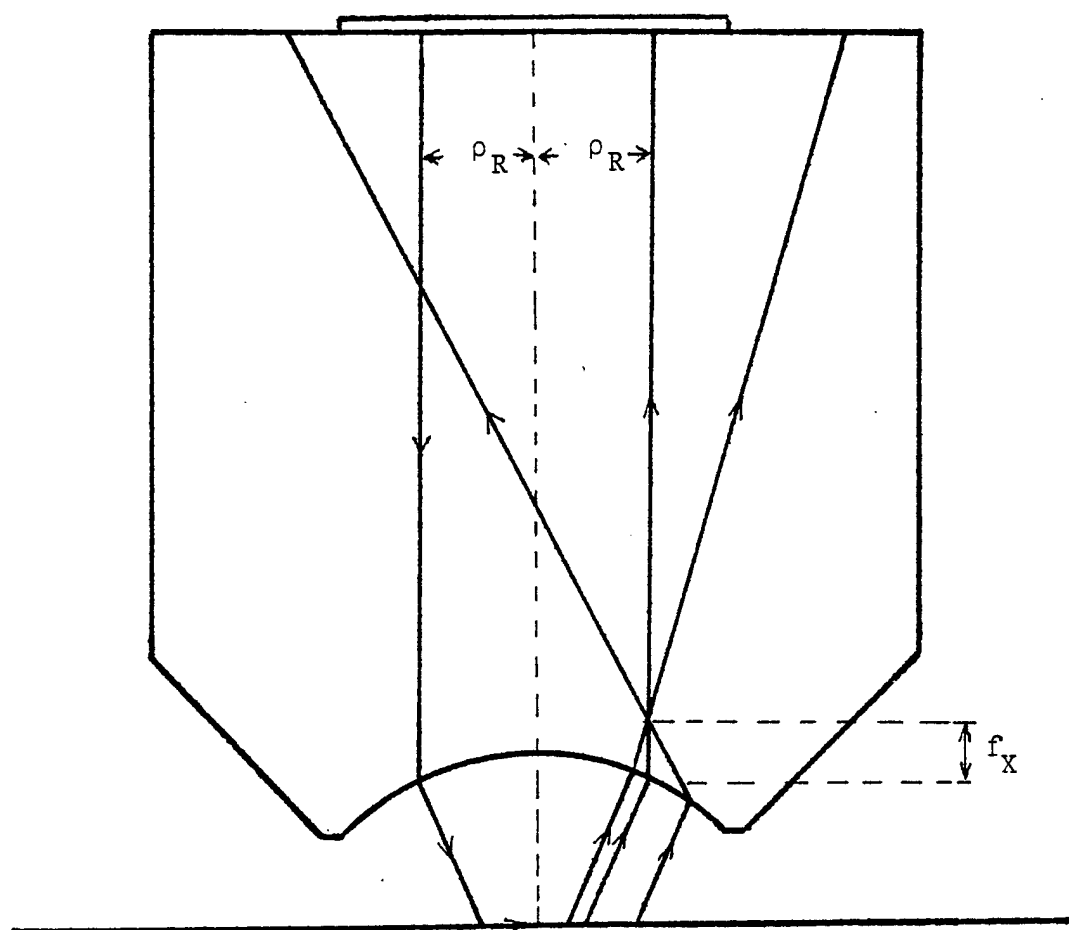


**Fig 2.5** Cross-sectional view of the lens showing a bundle of leaky rays forming a focus in the lens rod.



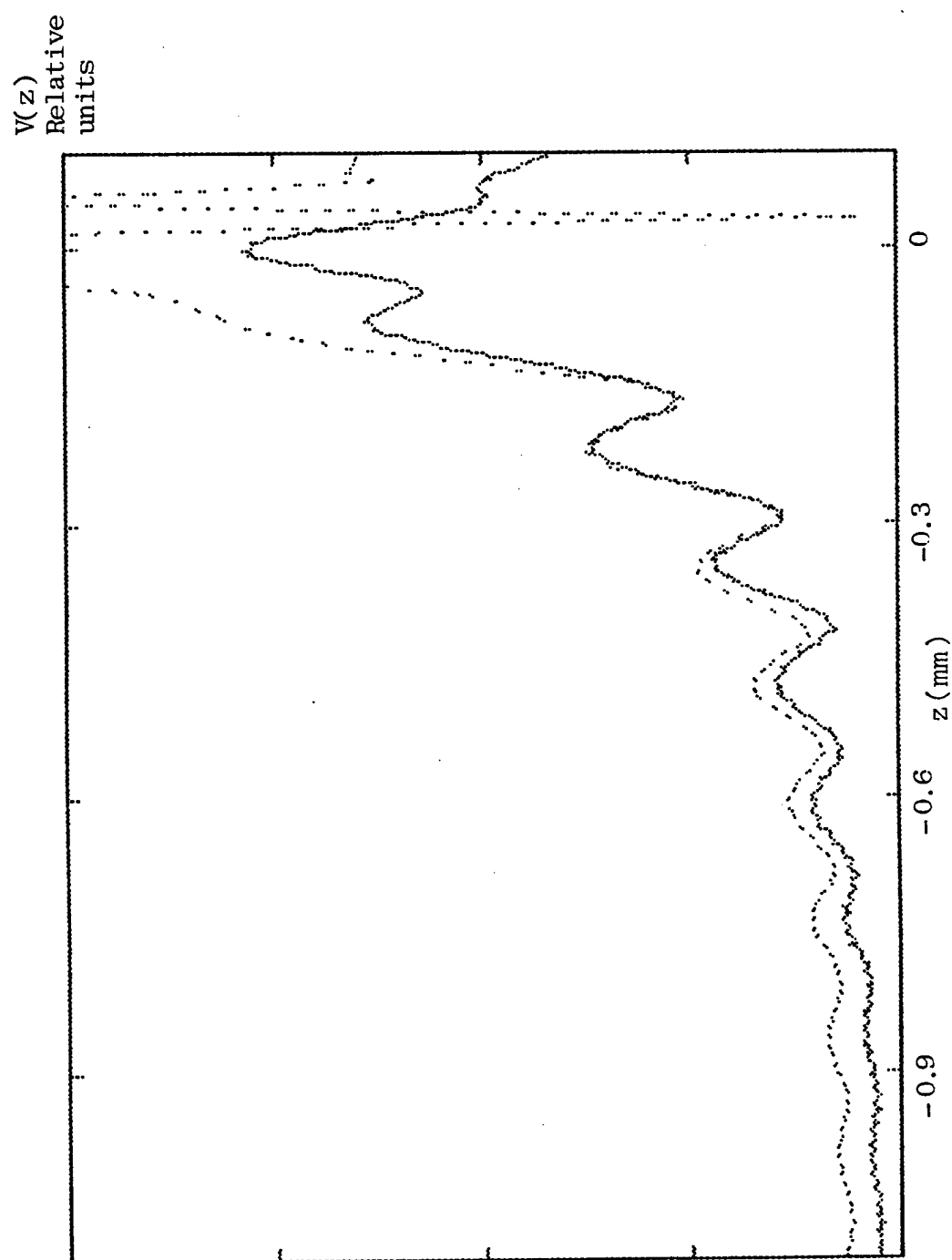


**Fig. 2.6**  $V(z)$  of glass for a circular aperture lens: observed (solid) and calculated using the geometric ray approach (dotted).

## 2.3 Diffraction correction to the ray model

### 2.3.1 Introduction

The theoretical  $V(z)$  obtained with the angular spectrum approach agrees much better with the experimental data than the ray model  $V(z)$ , especially near focus ( $|z|$  small), as can be seen in Figs. 2.4 and 2.6. Since the angular spectrum model takes diffraction into consideration, it may be suspected that diffraction effects in the lens rod play an important role in forming  $V(z)$ . Therefore it is desirable to compensate for these effects in the ray model of  $V(z)$ .

Assuming the transducer radiates as a uniform piston source, the diffracted field  $U$  at the back of the lens may be found by the method of Tjotta and Tjotta [12]. The amplitude and the phase of this field are plotted as a function of  $\rho$  in Figs. 2.7a and 2.7b.

Transmission and refraction at the lens-water interface will now be modelled by geometrical ray theory which assumes that the field behaves locally as a plane wave and treats the phase and amplitude variations of the field separately. The gradient of the phase of the field at a point determines the direction of the local wavevector and, thus, the local angle of incidence. The direction of the refracted ray may then be found using Snell's Law, thereby defining the location of focus. The angle of incidence also influences the lens-water transmission coefficient  $T_{LW}$ , thus effecting the amplitude profile of the transmitted field.

### 2.3.2 Approximation of phase variation of field $U(\rho)$

The local wavevector  $\underline{k}$  may be expressed as

$$\underline{k}(\underline{r}) = \nabla \phi(\underline{r}), \quad (2.3.1)$$

where  $\phi$  is the spatial component of the phase factor, i.e.

$$U(\underline{r}) = |U(\underline{r})| e^{i\phi(\underline{r})}, \quad (2.3.2)$$

In the lens rod which has axial symmetry about the  $z$  axis

$$\underline{r} = \rho \underline{\rho}_0 + z \underline{z}_0, \quad (2.3.3)$$

and  $|\underline{k}(\underline{r})| = k_L = \omega / v_L$  is the wavenumber in the lens medium. From (2.3.1) the component of  $\underline{k}$  along the  $\rho$  direction is

$$k_\rho = \frac{\partial \phi(\underline{r})}{\partial \rho}. \quad (2.3.4)$$

The angle of propagation  $\theta$ , measured with respect to the  $z$ -axis is then found as

$$\theta = \sin^{-1} (k_\rho / k_L), \quad (2.3.5)$$

The angle  $\theta$ , found from the phase of the field by numerically carrying out the above procedure is plotted as a function of  $\rho$  in Fig. 2.8. For lens considered here the maximum angular deviation of the incident ray from the vertical axis is about  $1.3^\circ$ . It is

therefore reasonable to assume that the acoustic field incident on the lens surface has no cross- sectional phase variation and thus strikes this surface as a well- collimated beam.

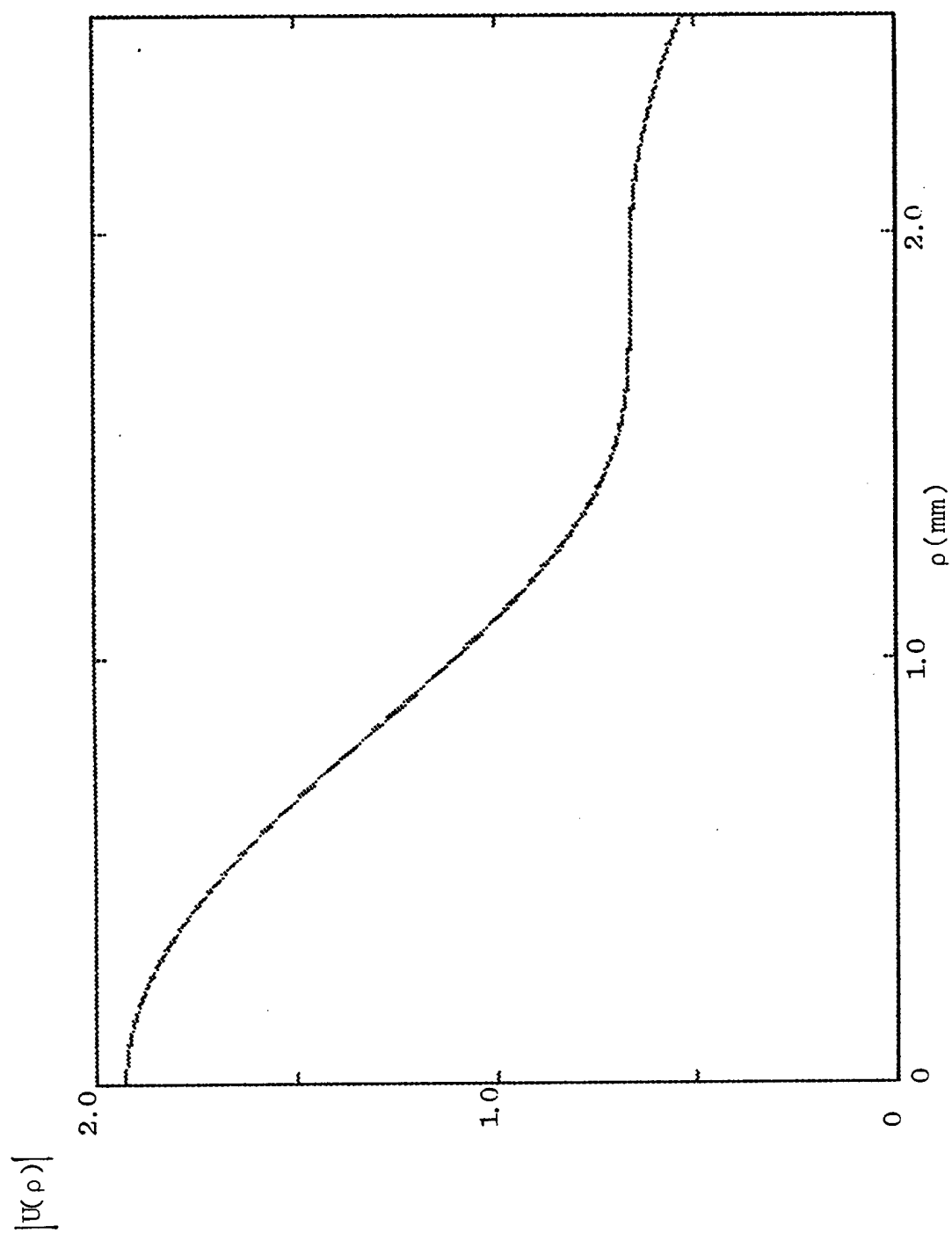


**Fig 2.7a** Amplitude profile of field  $U(\rho)$  illuminating the back focal plane. Calculated using the theory of Tjotta and Tjotta [12].

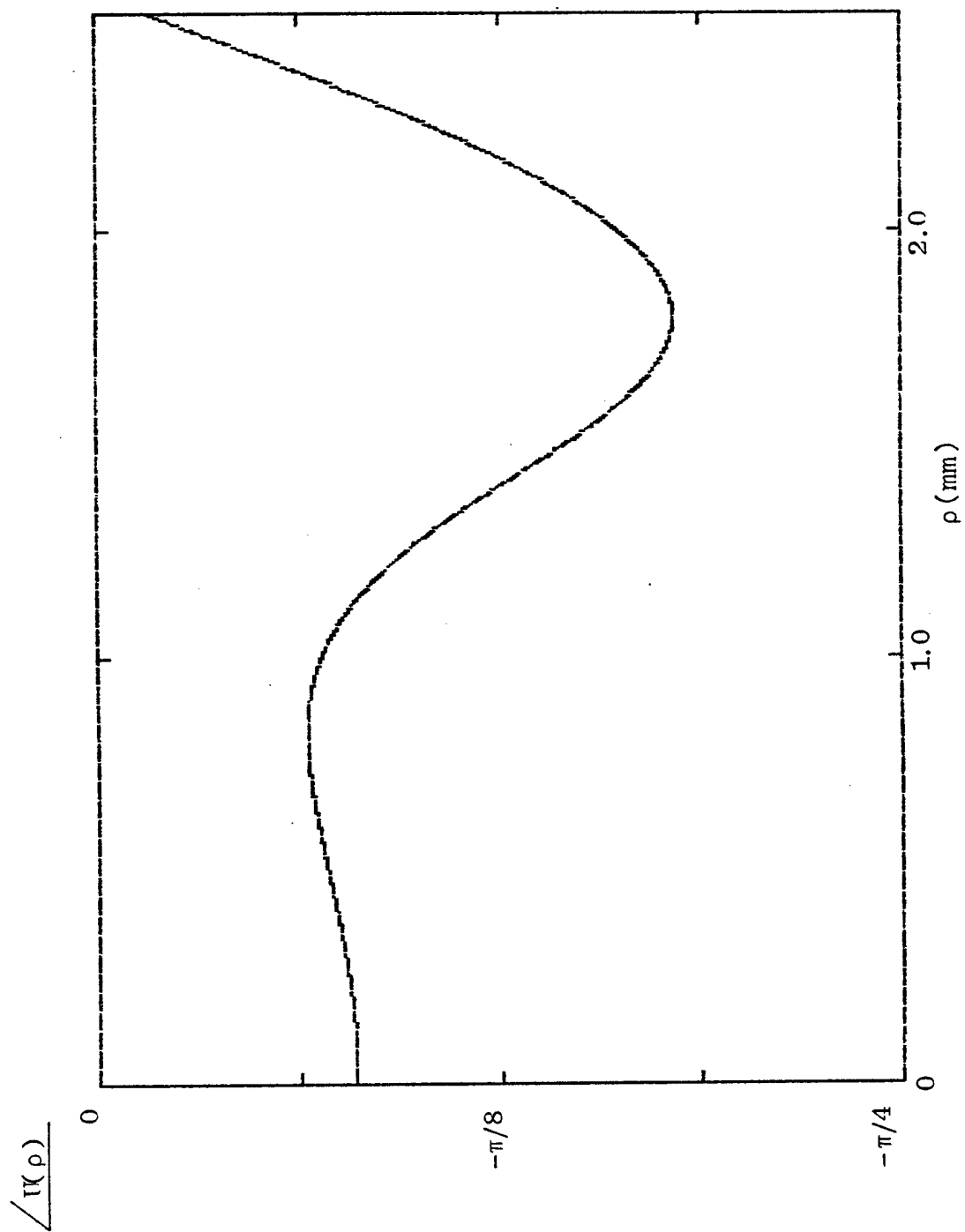


**Fig 2.7b** Relative phase profile of field  $U(\rho)$  illuminating the back focal plane.  
Calculated using the theory of Tjotta and Tjotta [12].

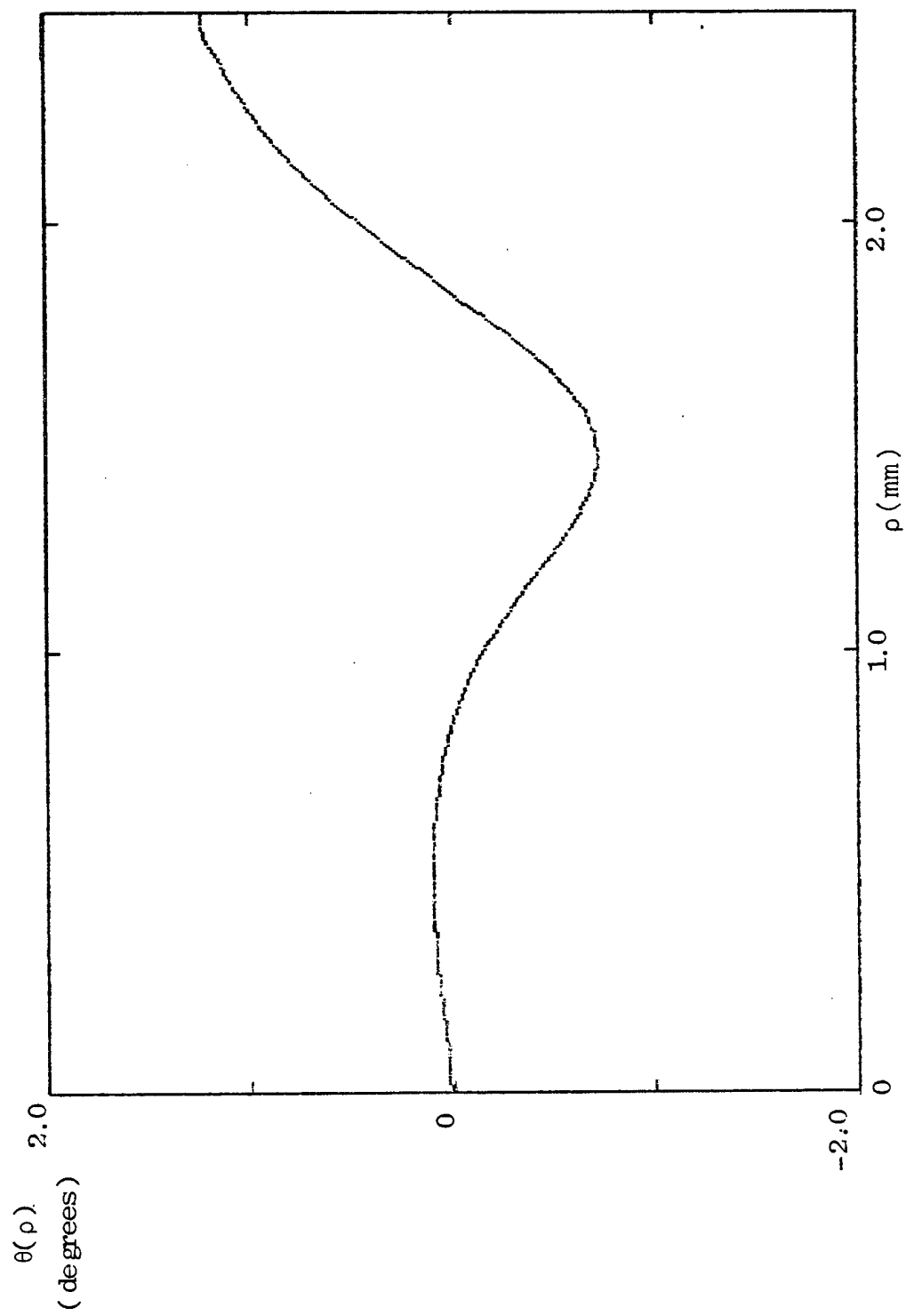


**Fig. 2.8** Angular deviation  $\theta$  from the vertical of rays illuminating the back focal plane.

### 2.3.3 Approximation of amplitude variation of field $U(\rho)$

The diffracted field  $U(\rho)$  is transmitted through the lens surface into water with a transmission coefficient  $T_{LW}(\rho)$ . The field reflected from the sample surface should similarly be scaled by the water-lens reflection coefficient  $T_{WL}(\rho)$ . As has been justified in the angular spectrum approach,  $T_{WL}$  is assumed to be independent of  $z$  and the field  $U(\rho)$   $T_{LW}(\rho)$  may therefore be multiplied by  $T_{WL}$  prior to scattering from the sample surface. Normalizing by  $T_{WL}(0)$   $T_{LW}(0)$ , the resulting field variation  $U_{eff}(\rho)$  is given by

$$U_{eff}(\rho) = \frac{U(\rho) T_{LW}(\rho) T_{WL}(\rho) \exp(k_W D/n)}{T_{WL}(0) T_{LW}(0)} \quad (2.3.6)$$

The amplitude of  $U_{eff}(\rho)$  is plotted in Fig. 2.9. The aperture pupil function  $P_1$  is defined as

$$P_1(\rho) = \text{circ}(\rho) . \quad (2.3.7)$$

It is possible to approximate the amplitude of  $U_{eff}$  with a superposition of Gaussians

$$U_{eff}(\rho) = \exp(ik_W D/n) \sum_i A_i \exp\left(\frac{-\rho^2}{B_i^2}\right) \quad (2.3.8)$$

The result of fitting with two Gaussians:

$$U_{eff}(\rho) = \exp(ik_W D/n) \sum_i A_i \exp\left(\frac{-\rho^2}{B_i^2}\right) \quad i=1,2 \quad (2.3.9)$$



is plotted in Fig. 2.9 for comparison with the exact field  $U_{\text{eff}}$ . The amplitudes  $A_i$  and widths  $B_i$  of these Gaussians were found by trial and error to be  $A_1 = 1.35$ ,  $B_1 = 1000 \mu\text{m}$ ,  $A_2 = .58$ , and  $B_2 = 2700 \mu\text{m}$  for the lens considered here (see Appendix B for lens dimensions). It is possible to use a least squares fit, as well as more terms in expansion (2.3.8) to improve the approximation to  $|U_{\text{eff}}|$ . However, it appears from Fig. 2.9 that for the lens considered here the use of these two Gaussians is a sufficiently good approximation of  $|U_{\text{eff}}|$  and, therefore, this representation will be used here.

### 2.3.4 Calculation of the transducer response $V_G(z)$

It is first important to summarize the microscope ray analysis as developed by Bertoni [2] for the case of uniform illumination of the lens. The source field  $U$  is transmitted through the lens and focused to a point at the front focal plane. The sample surface acts as a plane mirror located a distance  $z$  away from the front focal plane, and, therefore, creates an image of the focal point at a distance  $f+2z$  below the lens aperture (Fig. 2.10). The field suffers a phase change of  $\pi$  due to passage through focus. The resulting field, which now travels away from the sample, is imaged by the lens to form an effective point source illuminating the transducer. The location  $u$  of this source can be found from the lens imaging formula as

$$u = \frac{f(f+2z)}{2nz} . \quad (2.3.10)$$

The sample reflection coefficient is assumed to be constant, i.e.  $\mathcal{R}(\rho) = \mathcal{R}(0)$ , which is

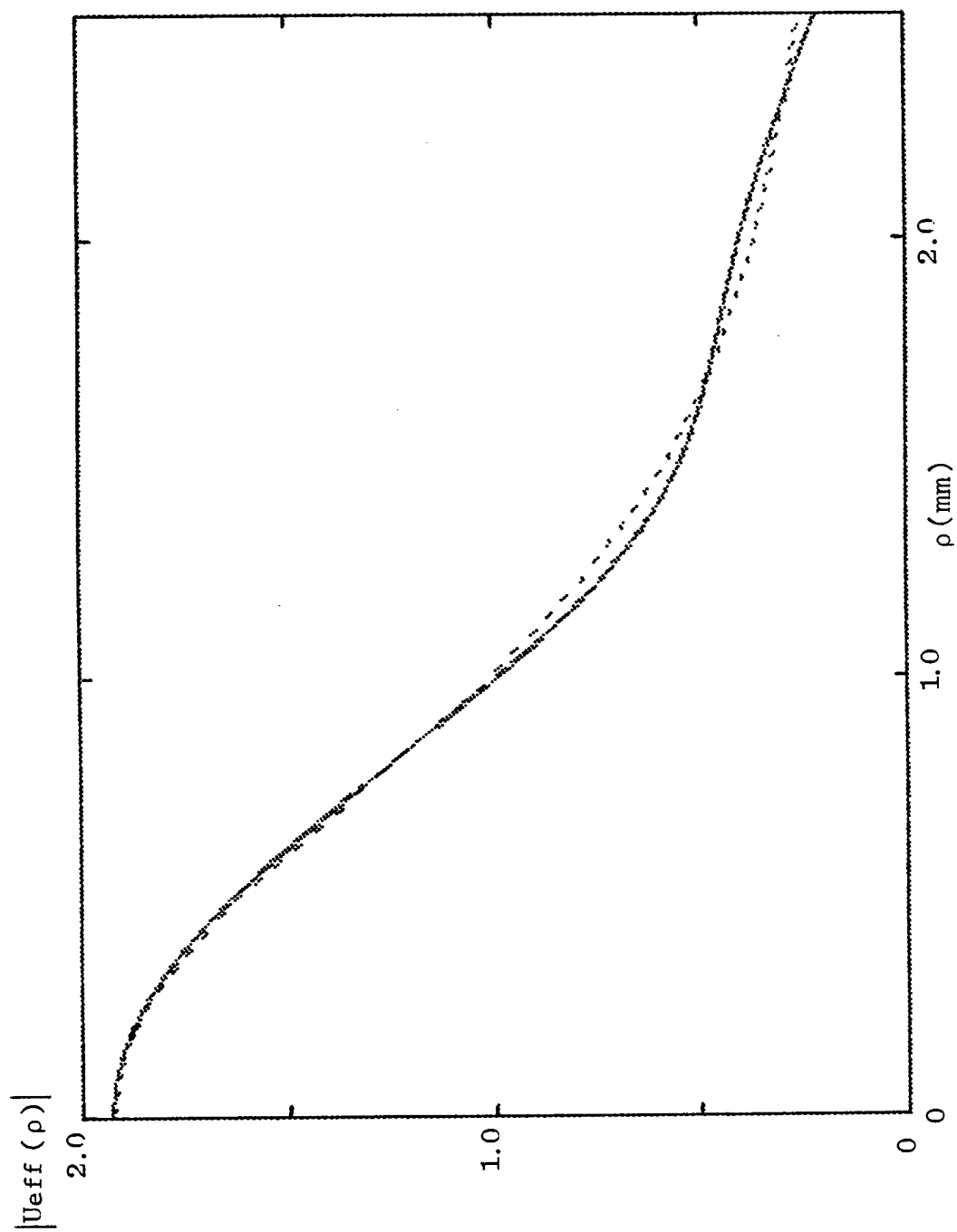


**Fig. 2.9** Amplitude profile of effective field  $U_{\text{eff}}(\rho)$  illuminating the back focal plane:

(a) Calculated using the theory of Tjotta and Tjotta [12] (solid) and

(b) two-Gaussian fit (dashed).

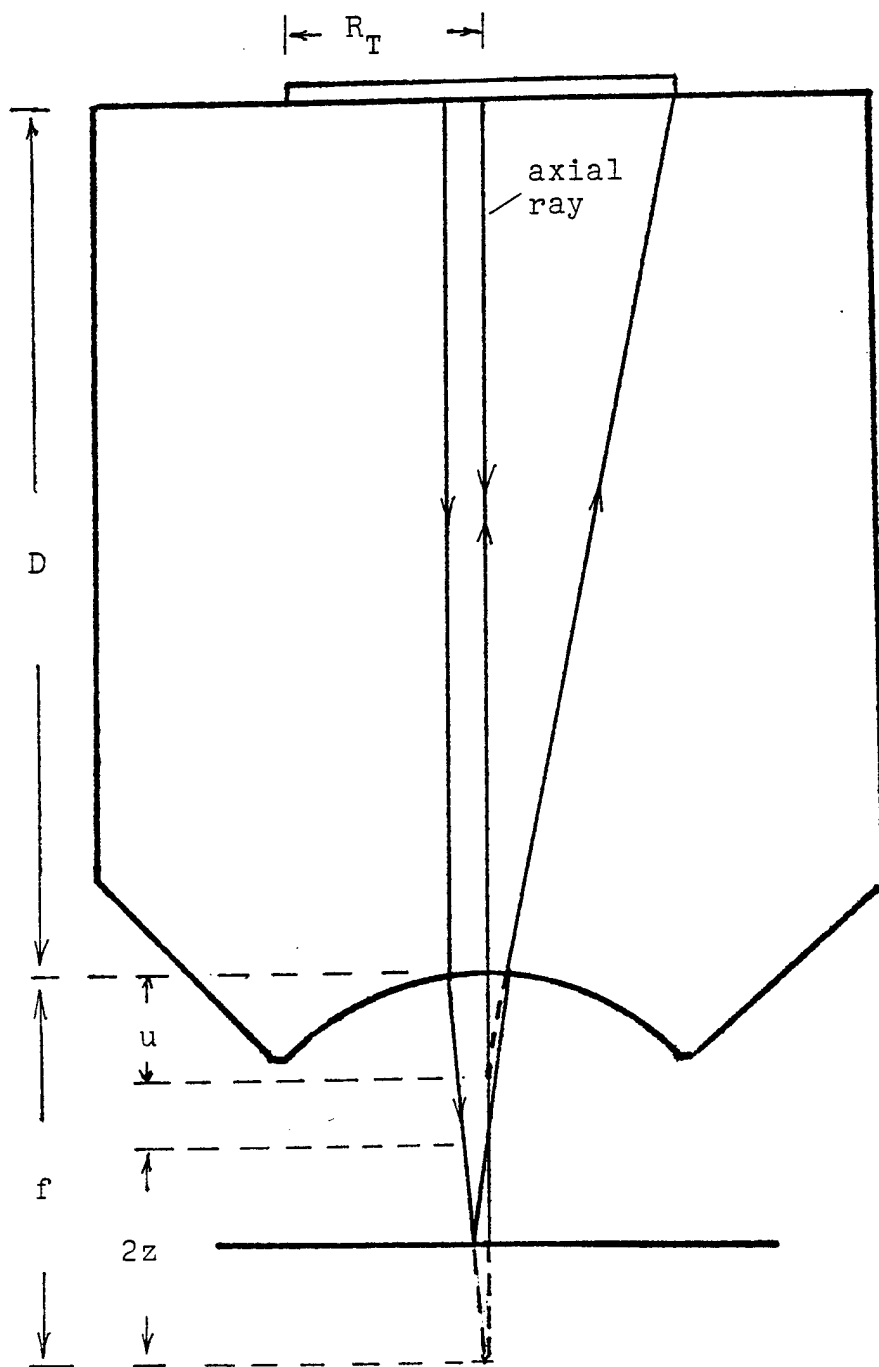


Fig. 2.10 Ray structure for specularly reflected component  $V_G$  for  $z < 0$ .

strictly true at normal incidence. Therefore the scattered field  $U_r(\rho)$  illuminating the back of the lens is given by:

$$U_r(\rho) = - \frac{T_{LW}(0) T_{WL}(0) R(0) \exp(2i k_w (f+z))}{M_1} \cdot \exp\left(\frac{ik_w \rho^2}{2n(-u)}\right) U_{\text{eff}}\left(\frac{\rho}{M_1}\right) P_1\left(\frac{\rho}{M_1}\right) P_2(\rho). \quad (2.3.11)$$

where  $M_1$  is the magnification / reduction scaling factor due to ray spreading in the water:

$$M_1 = \frac{|f + 2z|}{f}. \quad (2.3.12)$$

The aperture pupil functions  $P_1$  and  $P_2$  are defined as

$$P_1(\rho) = P_2(\rho) = \text{circ}(\rho/R_a) \quad (2.3.13)$$

$$\begin{aligned} \text{circ}(x) &= 1, & 0 < x < 1 \\ &= 0, & x > 1. \end{aligned}$$

The transducer response  $V_G$  can be found from (2.1.1). Here the effective source field  $u_1^+(\rho)$  is  $U_{\text{eff}}(\rho)$  and the scattered field  $u_1^-(\rho)$  is  $U_r(\rho)$ , given by (2.3.11). Using the Gaussian expansion (2.3.9) for  $U_{\text{eff}}(\rho)$  and normalizing by the transducer area:

$$V_G = - \frac{T_{LW}(0) T_{WL}(0) \ell(0) \exp(2i k_w (D/n+f+z))}{M_1 \pi R_T^2} \cdot 2\pi \cdot \int_0^{R_a} \exp\left(\frac{i k_w \rho^2}{2n(-u)}\right) \sum_{ij} A_i A_j \exp\left(\frac{-\rho^2}{B_i^2}\right) \exp\left(\frac{-\rho^2}{(B_j M_1)^2}\right) P_1\left(\frac{\rho}{M_1}\right) P_2(\rho) \rho d\rho. \quad (2.3.14)$$

The product of sums in (2.3.14) can be expanded:

$$\sum_q A_{1q} \exp\left(\frac{-\rho^2}{(B1_q)^2}\right) = \sum_{ij} A_i A_j \exp\left(\frac{-\rho^2}{B_i^2}\right) \exp\left(\frac{-\rho^2}{(B_j M_1)^2}\right), \quad (2.3.15)$$

$$A_{1q} = A_i A_j, \quad \frac{1}{(B1_q)^2} = \frac{1}{B_i^2} + \frac{1}{(B_j M_1)^2}$$

where  $q$  ranges from 1 to 4 (assuming two Gaussians are used in (2.3.8)).

Substituting (2.3.15) into (2.3.14) and carrying out the integration gives

$$V_G = - \frac{T_{LW}(0) T_{WL}(0) \ell(0)}{R_T^2 M_1} \exp(2i k_w (D/n+f+z)) \cdot \sum_i 2 A_{1i} \frac{n B_{1i}^2(-u)}{i k_w B_{1i}^2 - 2n(-u)} \cdot \left[ \exp\left(\frac{i k_w r_T^2}{2n(-u)}\right) \exp\left(\frac{-r_T^2}{B_{1i}^2}\right) - 1 \right], \quad (2.3.16)$$

where

$$\begin{aligned} r_T &= R_a M_1, & M_1 < 1 \\ &= R_a, & M_1 > 1 \end{aligned}$$

As can be seen from the above, the advantage of Gaussian expansion (2.3.8) of  $|U_{\text{eff}}(\rho)|$  is that this representation allows the integration to be carried out analytically.

The diffraction-corrected voltage  $V_G(z)$ , calculated by using (2.3.16), is plotted versus  $z$  in Fig. 2.11 along with  $V_G(z)$  obtained by the angular spectrum approach and in Fig. 2.12 for comparison with the experimental  $V_G(z)$  obtained for a Teflon sample, taking advantage of the fact that Teflon-water interface does not support leaky modes and thus only the specular component of  $V(z)$  exists. In Fig. 2.13 three  $V(z)$  curves are plotted:  $V_G(z)$  calculated assuming uniform lens illumination by the ray method,  $V_G(z)$  corrected for diffraction and the actual Teflon data. Note the significant improvement in agreement between the experimental and theoretical curves obtained by including diffraction effects in the lens rod.

### 2.3.5 Calculation of the leaky contribution $V_L(z)$

Now the effect of diffraction in the lens rod on the leaky contribution  $V_L(z)$  will be considered. As discussed in previous section,  $V_L$  arises from the leaky surface waves excited on the sample surface by those rays from the transducer that cross the lens surface at  $\rho = \rho_R$ . Thus the amplitude of  $V_L$  is directly proportional to the amplitude of the diffracted source field at  $\rho = \rho_R$ , i.e.  $|U(\rho)|$ . Since  $V_L$  in (2.2.7) was calculated using  $|U(\rho)| = 1$  for all  $\rho$ , it would therefore be proper to scale  $V_L$  by  $|U(\rho_R)|$  thereby taking diffraction in the lens rod into account.

The amplitude of resulting  $V_L(z)$  is shown in Fig. 2.14. If desired, the behavior of  $V_L(z)$  near  $z = 0$  can be modelled better by implementing a correction described by Bertoni in [2].

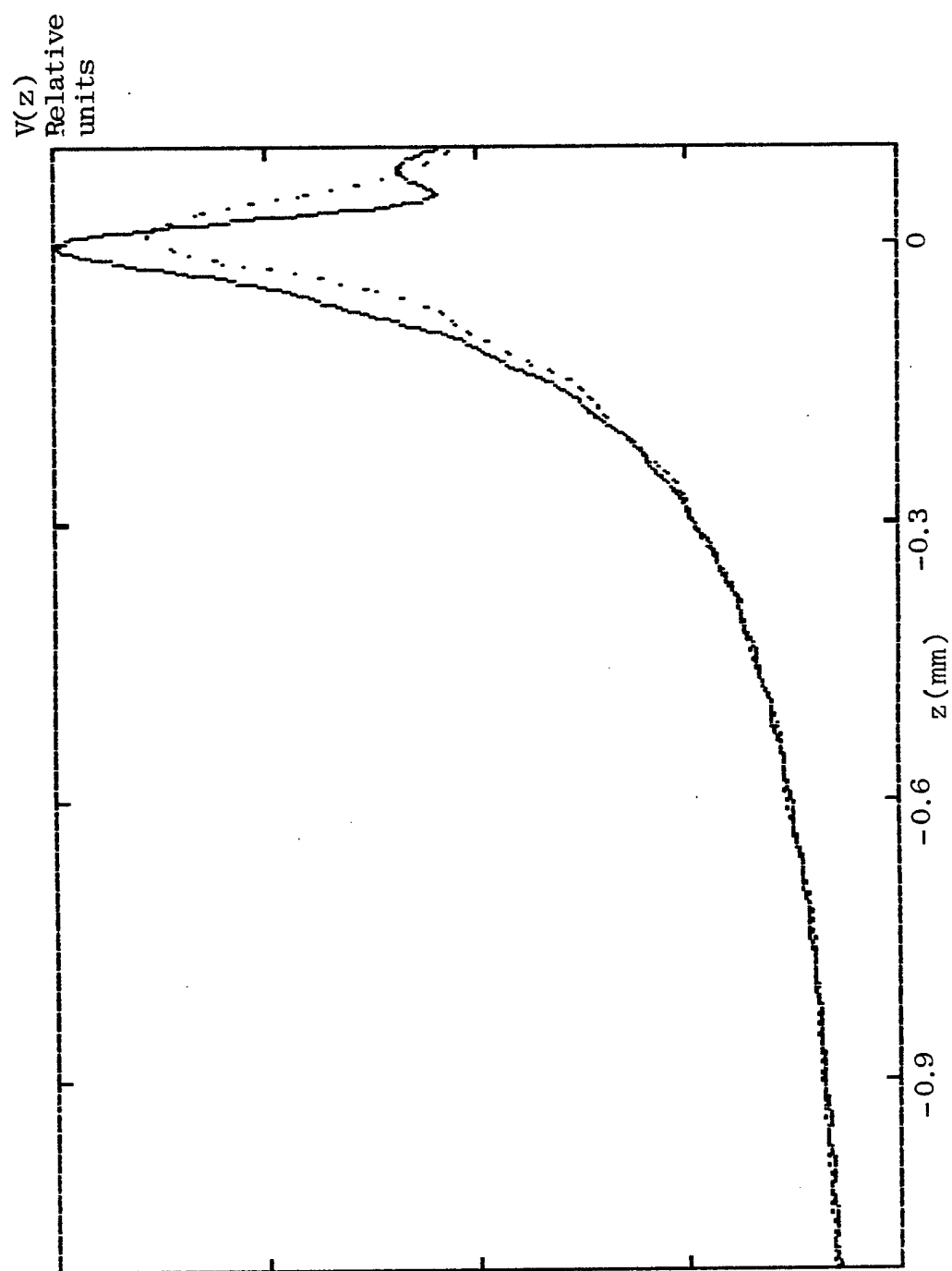


**Fig. 2.11**  $V(z)$  of Teflon for a circular aperture lens calculated using (a) the angular spectrum approach (solid) and (b) the diffraction-corrected ray approach (dotted).

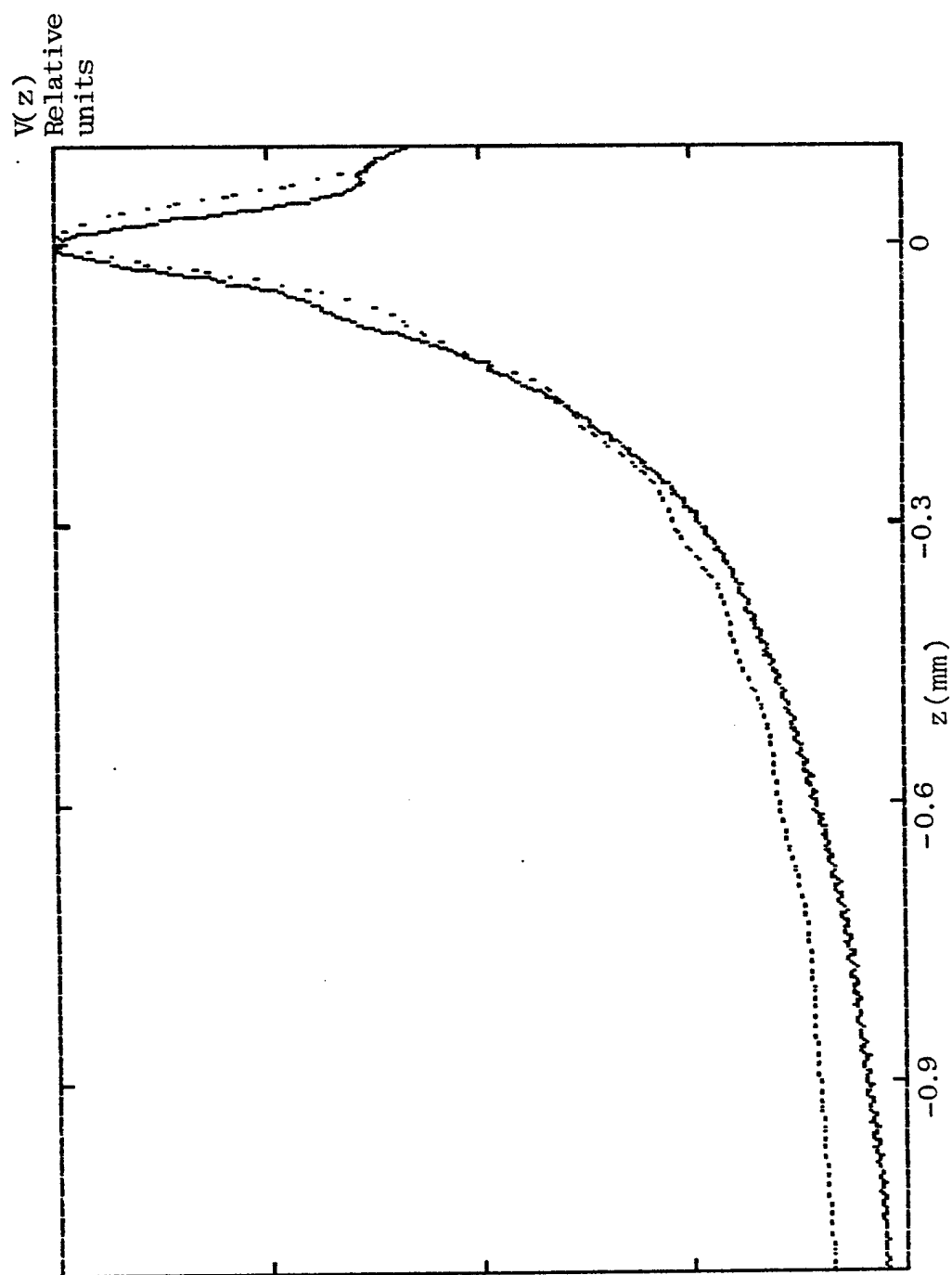


**Fig. 2.12**  $V(z)$  of Teflon for a circular aperture lens: observed (solid) and calculated using the diffraction-corrected ray approach (dotted).



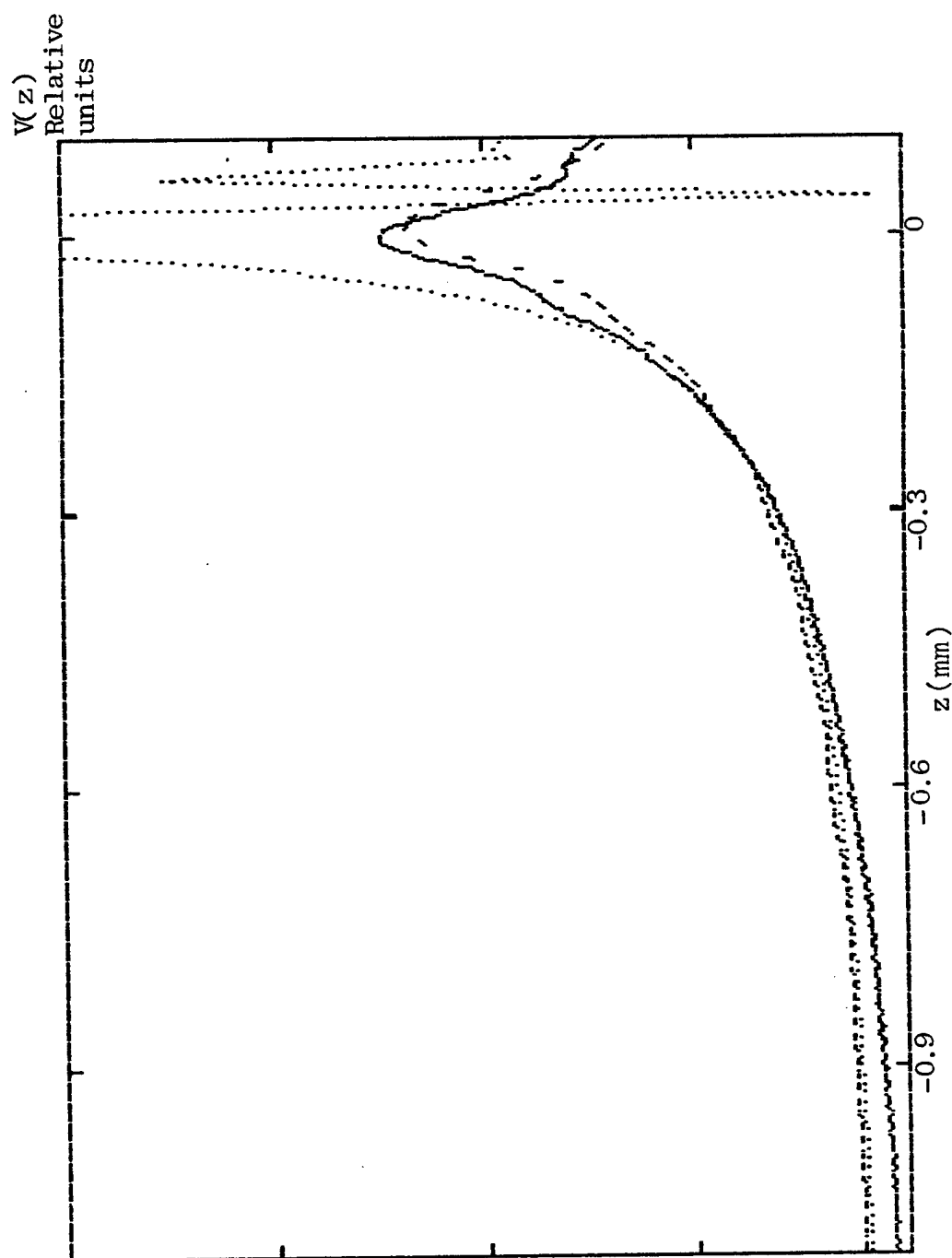


**Fig. 2.13**  $V(z)$  of Teflon for a circular aperture lens: (a) observed (solid), (b) calculated using the diffraction-corrected ray approach (dashed) and (c) calculated using the geometric ray theory (dotted).

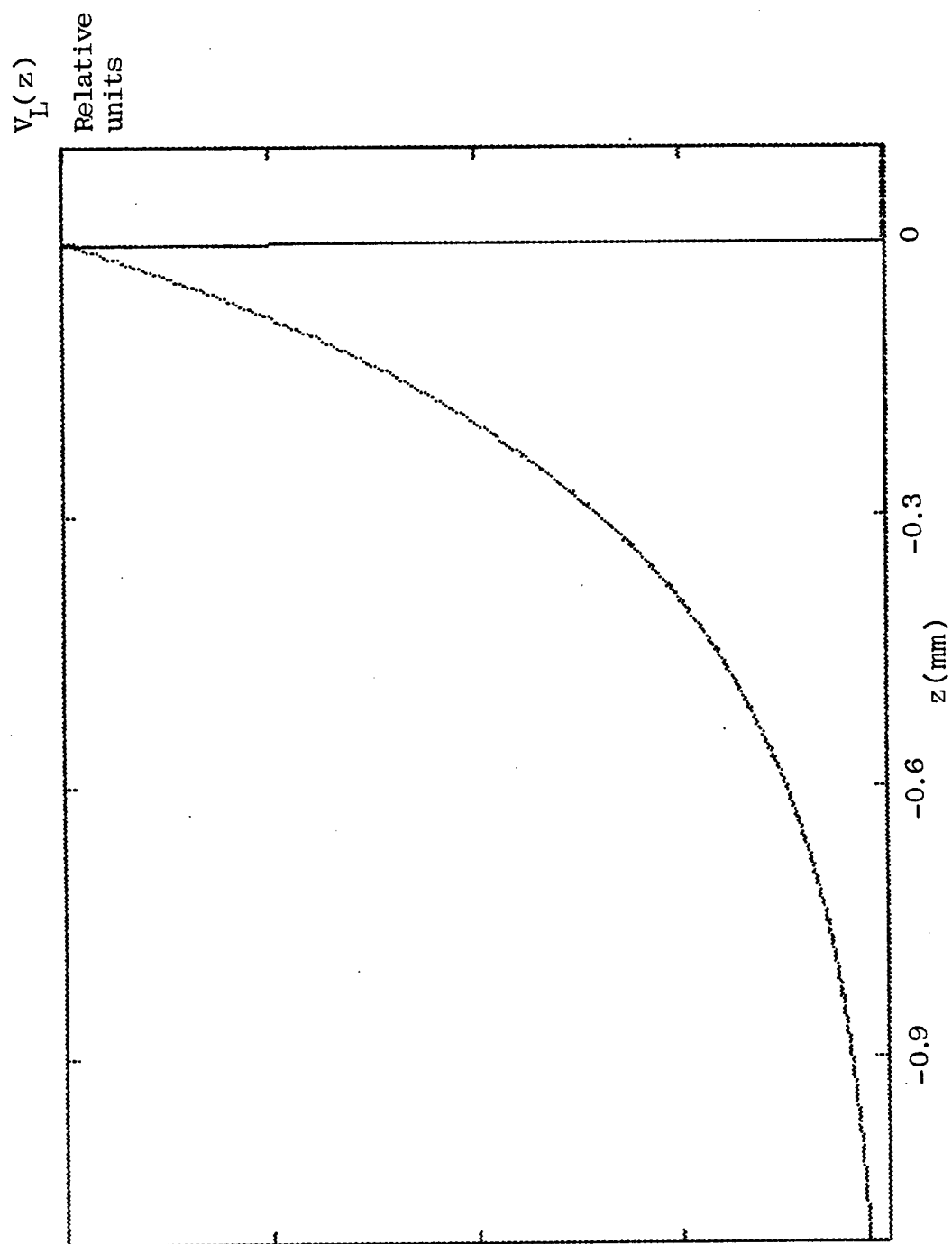
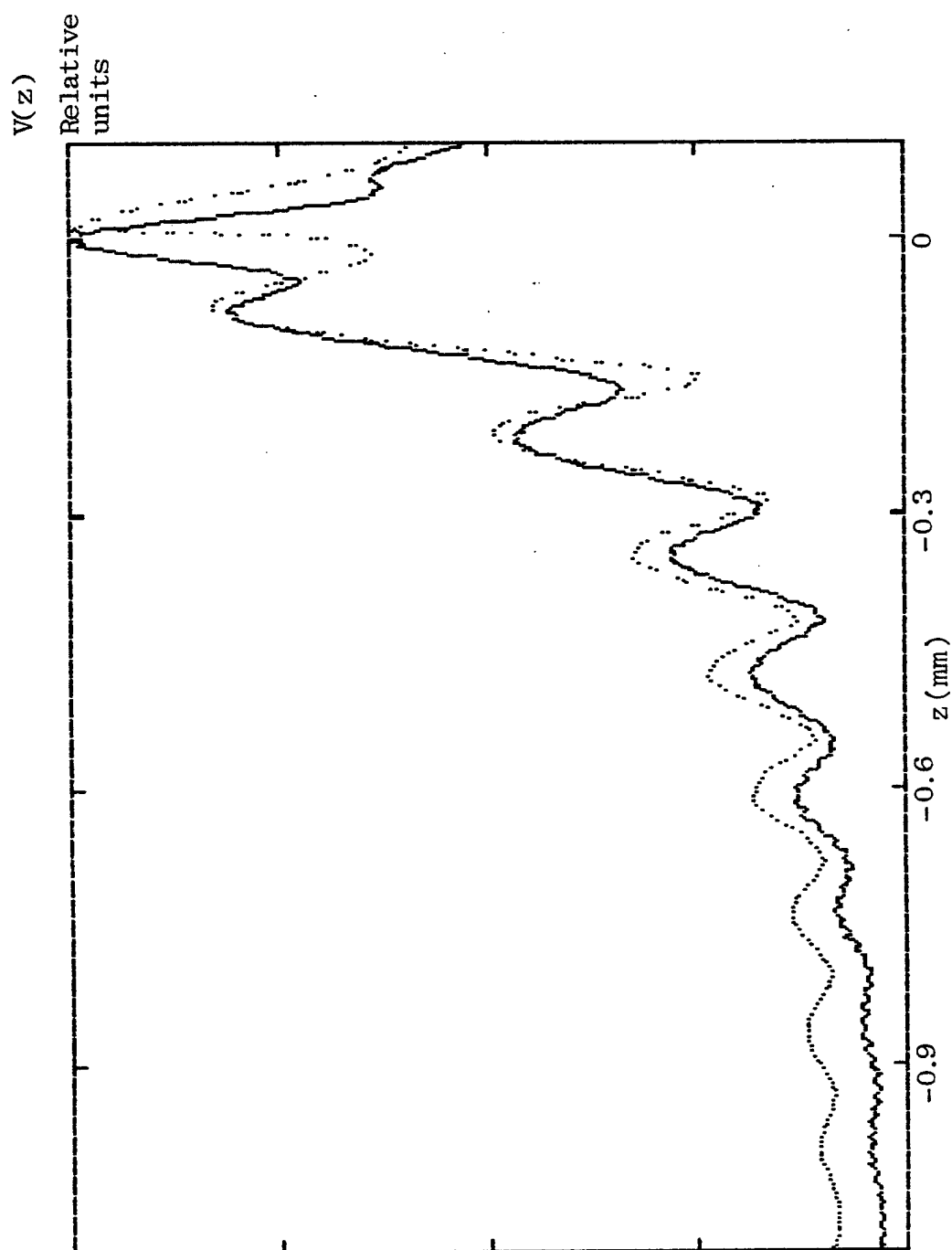


Fig. 2.14 Calculated leaky contribution  $V_L(z)$  for glass.

### 2.3.6 Calculation of the total transducer response $V(z)$

To calculate the final transducer response  $V(z)$ , diffraction-corrected components  $V_G$  and  $V_L$  are added in accordance with (2.2.1). The resulting  $V(z)$  is plotted along with the experimentally obtained  $V(z)$  in Fig. 2.15, and with the  $V(z)$  calculated using the angular spectrum approach in Fig. 2.16. Including diffraction effects significantly improves the agreement with the measured result, as can be seen by comparing Fig. 2.15 with Fig. 2.6, which displays the  $V(z)$  calculated while ignoring diffraction. Further improvements in modelling of  $V(z)$  near  $z = 0$  would require the corrections in  $V_L(z)$  mentioned above.



**Fig. 2.15**  $V(z)$  of glass for a circular aperture lens: observed (solid) and calculated using the diffraction-corrected ray approach (dotted).

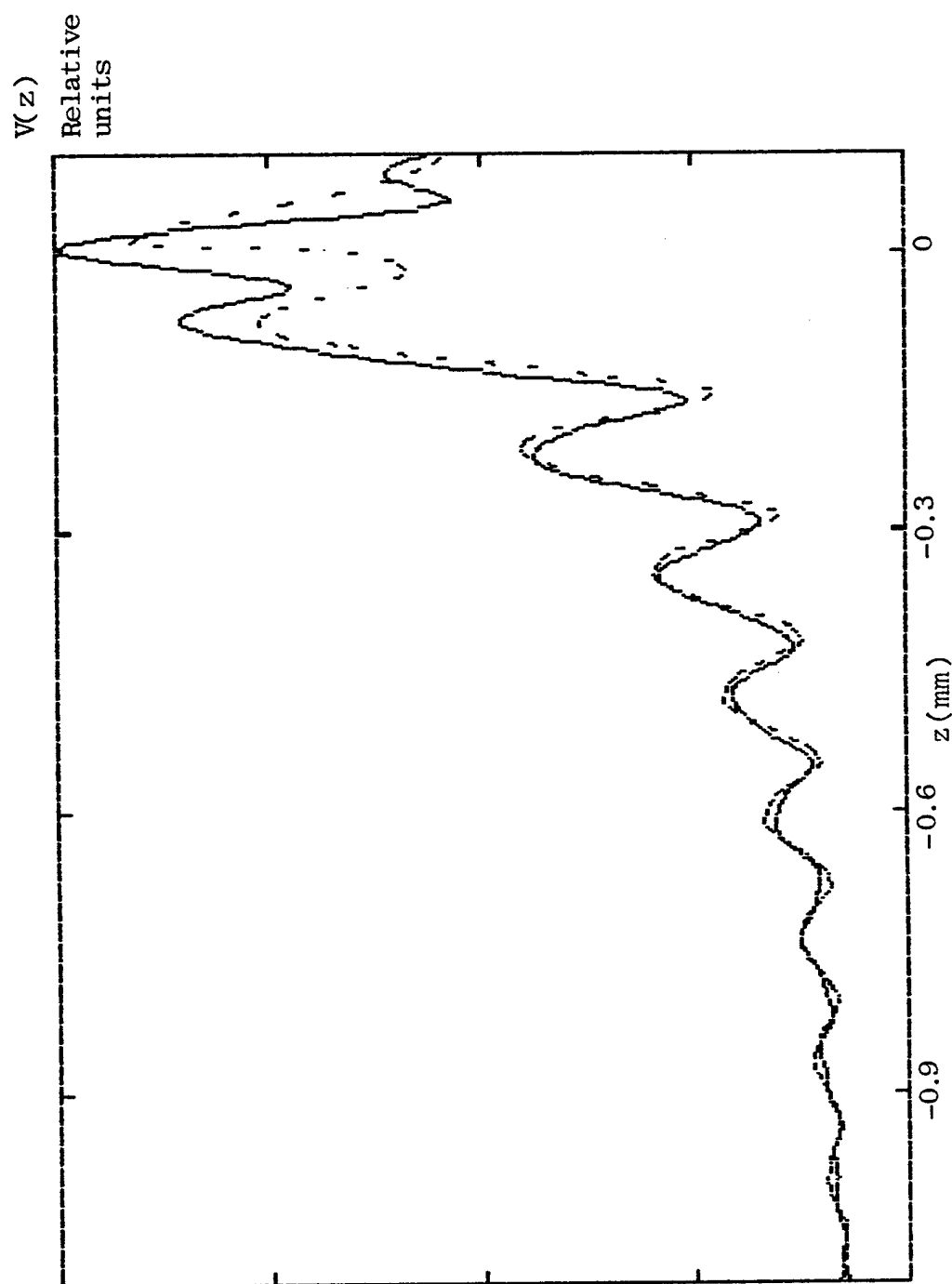


**Fig. 2.16**  $V(z)$  of glass for a circular aperture lens calculated using

(a) the angular spectrum approach (solid) and

(b) the diffraction-corrected ray approach (dashed).

## 2.4 Extraction of the Rayleigh wave velocity $v_R$ from the $V(z)$

It has been shown by Bertoni [2] that the spacing  $\Delta z$  between the  $V(z)$  minima is directly related to the Rayleigh velocity  $v_R$ :

$$\Delta z = \frac{\lambda_w}{2(1 - \cos \theta_R)} \quad (2.4.1)$$

This result follows from the ray model of the  $V(z)$  [2] and is valid for large  $|z|$  when the detected geometric fields have nearly planar phase fronts. It is possible to deduce  $v_R$  from the  $V(z)$  by simply measuring the separation between the neighboring minima of  $V(z)$ . This approach relies on only a few points and is, therefore, sensitive to the presence of noise in the  $V(z)$ . An alternative method, proposed by Kushibiki, et. al. [2], finds the  $\Delta z$  by Fourier transforming the pre-processed form of the  $V(z)$  to obtain the location of the spatial frequency peak corresponding to the periodicity in the ripple in the  $V(z)$ . This method has the advantage of using all of the collected  $V(z)$  data.

The following is a partial outline of an improved method of  $V(z)$  processing, proposed by Briggs[13], which will be implemented here.

The microscope used in this work measures only the amplitude and not the phase of the transducer voltage  $V$ . Thus, when  $V(z)$  data is collected, the measured quantity is

$$|V(z)| = |V_G(z) + V_L(z)|$$

The square of the amplitude becomes

$$|V(z)|^2 = |V_G|^2 + 2 |V_G| |V_L| \cos(\arg V_G - \arg V_L) + |V_L|^2 \quad (2.4.2)$$

The periodic component in the  $V(z)$  is due to the  $\cos(\arg V_G - \arg V_L)$  factor in the second term which is the result of the interference between the geometric and leaky contributions. It would therefore be useful to isolate this factor before attempting to determine the period of the ripple in  $V(z)$  since the other terms and factors would obscure the desired peak in the Fourier spectrum.

To remove  $|V_G|$  from (2.4.2) it should be noted that the functional form of  $V_G$  depends only on the lens geometry and is the same for all materials. It is therefore possible to determine  $V_G$  by measuring the  $V(z)$  of a material such as teflon, which has no leaky contribution. The measured  $|V(z)|$  of teflon must then be properly scaled to account for the difference in reflection coefficients of glass and teflon. One practical way to do so with measured data is to scale the  $|V(z)|$ 's of the two materials to match at a  $z$  location where the leaky component  $V_L(z)$  is negligible or zero, such as for  $z \ll 0$  or  $z > 0$ .

Once the desired  $|V_G(z)|$  of glass is obtained, a reduced form of  $|V(z)|$ , called  $V_I(z)$ , can be found from (2.4.2), where  $V_I(z)$  is defined as

$$V_I(z) = \frac{|V(z)|^2 - |V_G|^2}{|V_G|} + 2 |V_L| \cos(\arg V_G - \arg V_L) + \frac{|V_L|^2}{|V_G|}. \quad (2.4.3)$$

It will be assumed in this work that  $|V_L|$  is a slowly varying function of  $z$  and that it is small compared to  $|V_G|$  so that there is no significant spectral overlap between the  $\cos(\arg V_G - \arg V_L)$  term and the other terms in (2.4.3). As an illustration, a  $V_I(z)$  of glass is plotted in Fig. 2.17. The amplitude of the Fourier spectrum of  $V_I(z)$ , calculated by a Discrete Fourier Transform (DFT) routine, is displayed in Fig. 2.18. The location of the spectral peak in Fig. 2.18 is equal to  $1/\Delta z$ . The Rayleigh velocity  $v_R$  for glass, deduced with the aid of (2.4.1), is found to be 3164 m/s. When either the angular spectrum approach or the ray methods are used to theoretically predict the  $V(z)$  of glass,

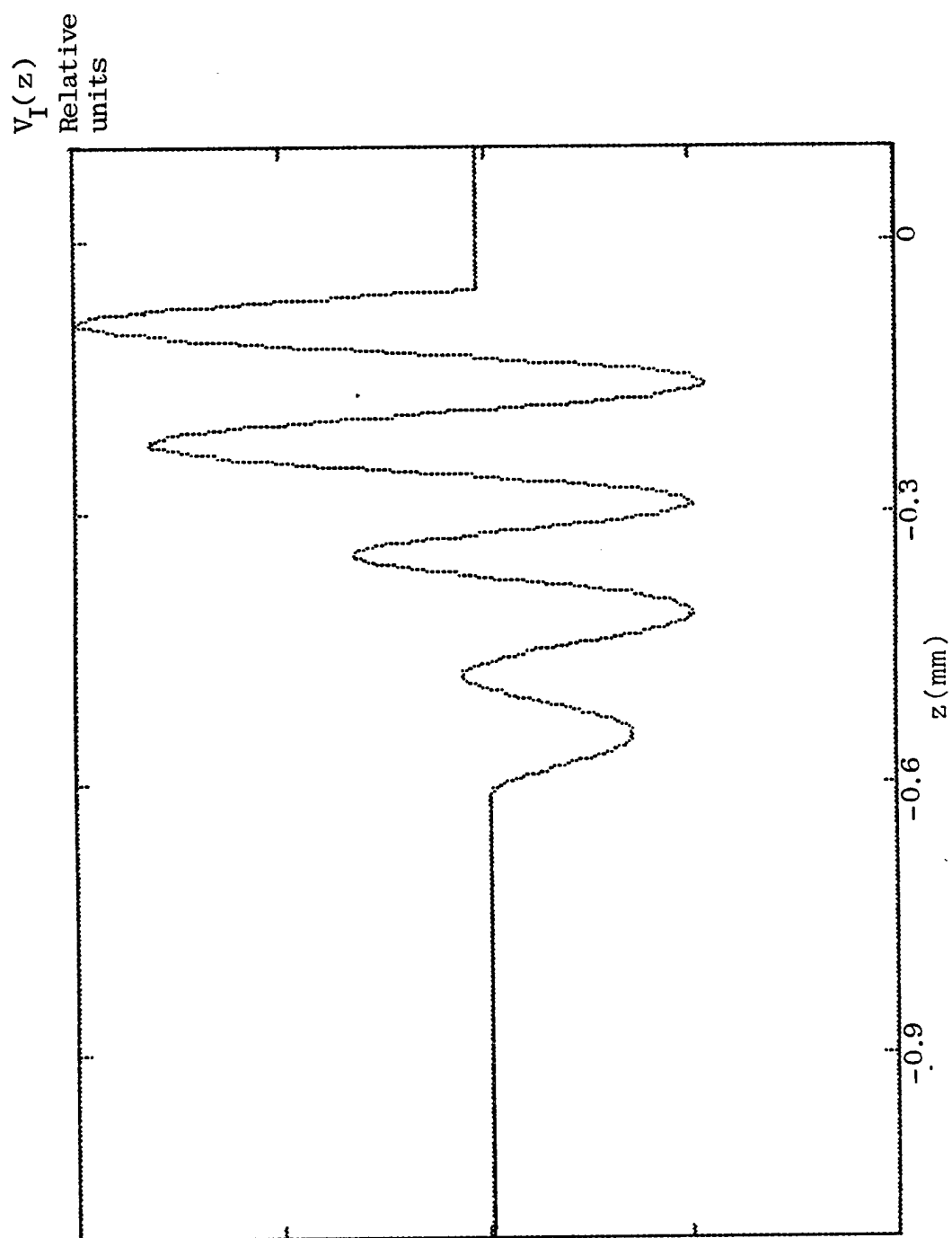


**Fig. 2.17**  $V_I(z)$  of glass obtained from measured data by

$$V_I(z) = (V^2(z) - V_G^2(z)) / V_G(z).$$



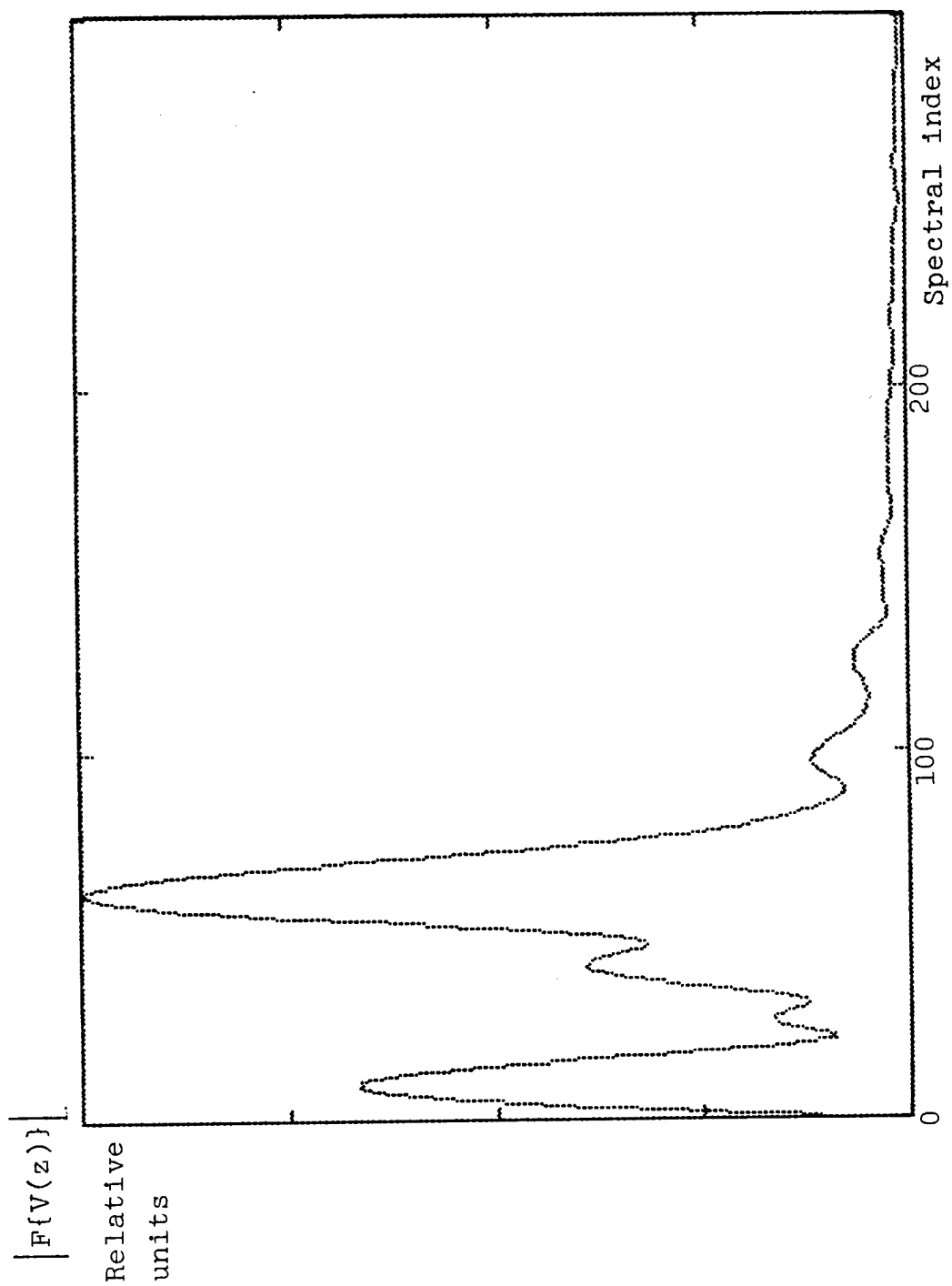


**Fig. 2.18** Amplitude of Fourier spectrum of  $V_1(z)$  of glass calculated by DFT.

the best fit is obtained for  $v_R = 3135$  m/s. which is assumed to be the nominal value of  $v_R$  for this particular glass sample. Thus, a  $v_R$  has been deduced from an experimental  $V(z)$  with an error of about 1%.

Applying the above procedure to a theoretically generated  $V(z)$  gives a value of  $v_R$  higher by about 1% than the value initially assumed during the generation, which demonstrates a bias consistent with the processing of the measured  $V(z)$ .

Several sources of this error have been found. First of all, as mentioned above, the expression (2.4.1] for the spacing between minima is strictly valid only for  $z \ll 0$ . For  $z$  near 0, the phase of the  $V_G$  exhibits other variations with  $z$  which alter the period in the interference pattern in  $V(z)$ . Thus, only the part of the  $V(z)$  far from the focus ( $z = 0$ ) should be used in the extraction of  $v_R$ . Another source of error in  $v_R$  is the residual  $z$ -dependent terms in (2.4.3), like  $|V_L(z)|$  and  $|V_L(z)|^2 / |V_G(z)|$ , which alter the spectrum of  $V_I$  and should therefore be removed prior to Fourier transformation. Implementing the above corrections in the processing of the calculated  $V(z)$  returns a Rayleigh velocity that is exactly equal to the initially assumed value.

It is difficult to implement these corrections for the processing of measured data since  $|V_L|$  is not a measured quantity and, therefore, cannot be easily removed from  $V_I$ . Furthermore, as  $|V(z)|$  decreases for large  $|z|$ , the signal-to-noise ratio deteriorates significantly, making the  $V(z)$  data far away from focus unusable for transformation into the frequency domain.

In summary, the above method can be used to find the Rayleigh velocity to within 1%.

## Chapter III

### Theoretical Modelling of $V(z)$ for the Slot Lens Acoustic Microscope

Both the angular spectrum and ray approaches are used to model the slot lens for determining  $V(z)$  and the results are compared with experiment for several materials. The slot lens is also used to obtain  $V(z)$  of Y-cut quartz for a number of slot orientations relative to the crystal X-axis. The Rayleigh wave velocity as a function of propagation direction is then deduced from these measurements and compared with accepted values.

#### 3.1 Angular Spectrum Approach

The angular spectrum approach, described in Chapter II, can be easily adapted for any lens, whose aperture plane can be described by a pupil function  $P(x,y)$ . Specifically, the pupil function for the slot lens is specified by

$$P(x,y) = \text{circ}\left(\frac{x}{w}\right) \text{circ}\left(\frac{\sqrt{x^2 + y^2}}{R_a}\right) \quad (3.1.1)$$

where  $w$  is the half-width of the slot ( $w \leq R_a$ ).

To find  $V(z)$ , the above  $P(x,y)$  is substituted into expression (2.1.2). The resulting  $V(z)$ , calculated for the case of a Teflon sample and a slot width  $w = 1.5$  mm is plotted in Fig. 3.1 together with the experimental result. A  $V(z)$  of a glass sample is compared with measurements of a microscope slide in Fig. 3.2.

It can be seen that calculated and measured results are in reasonable agreement.

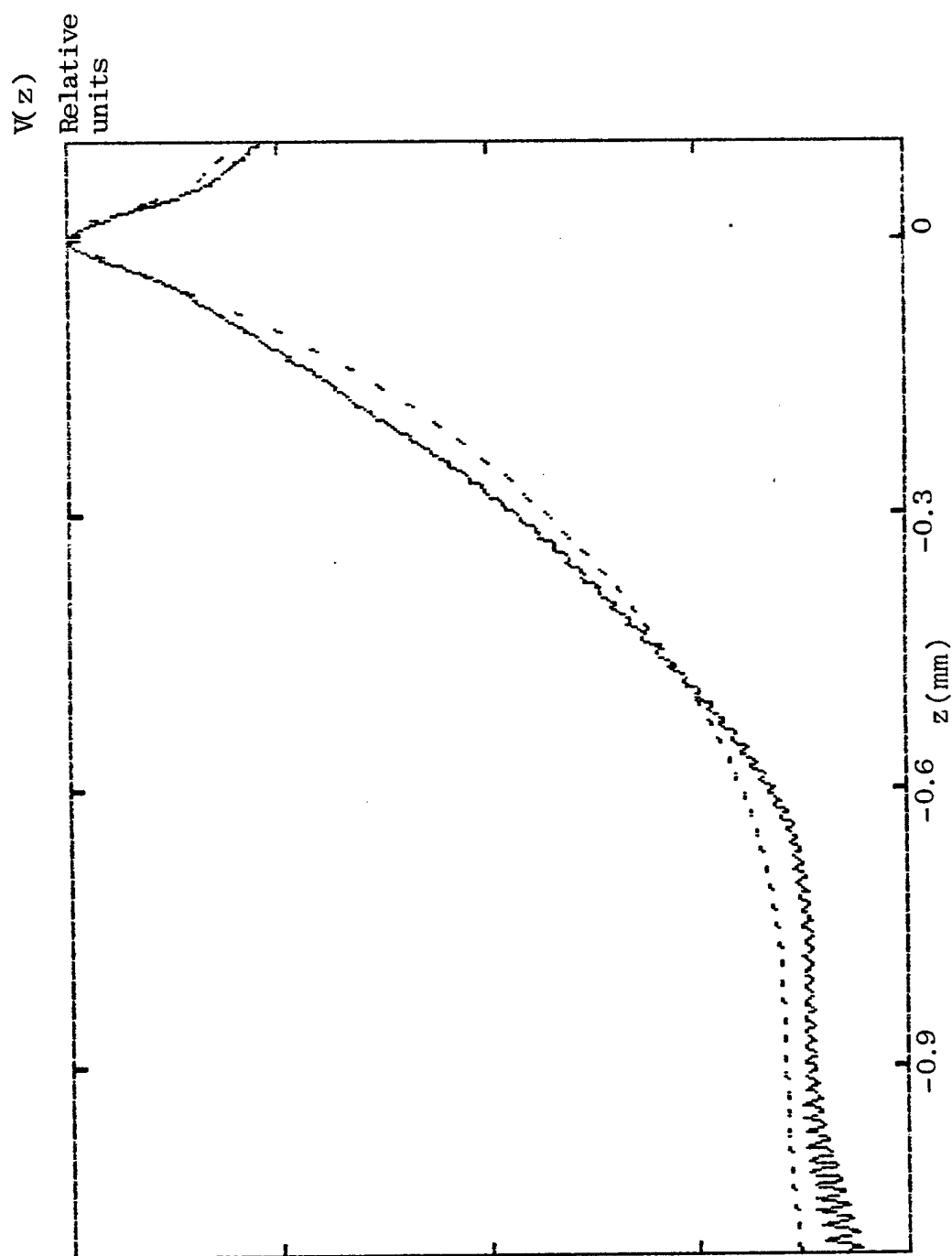
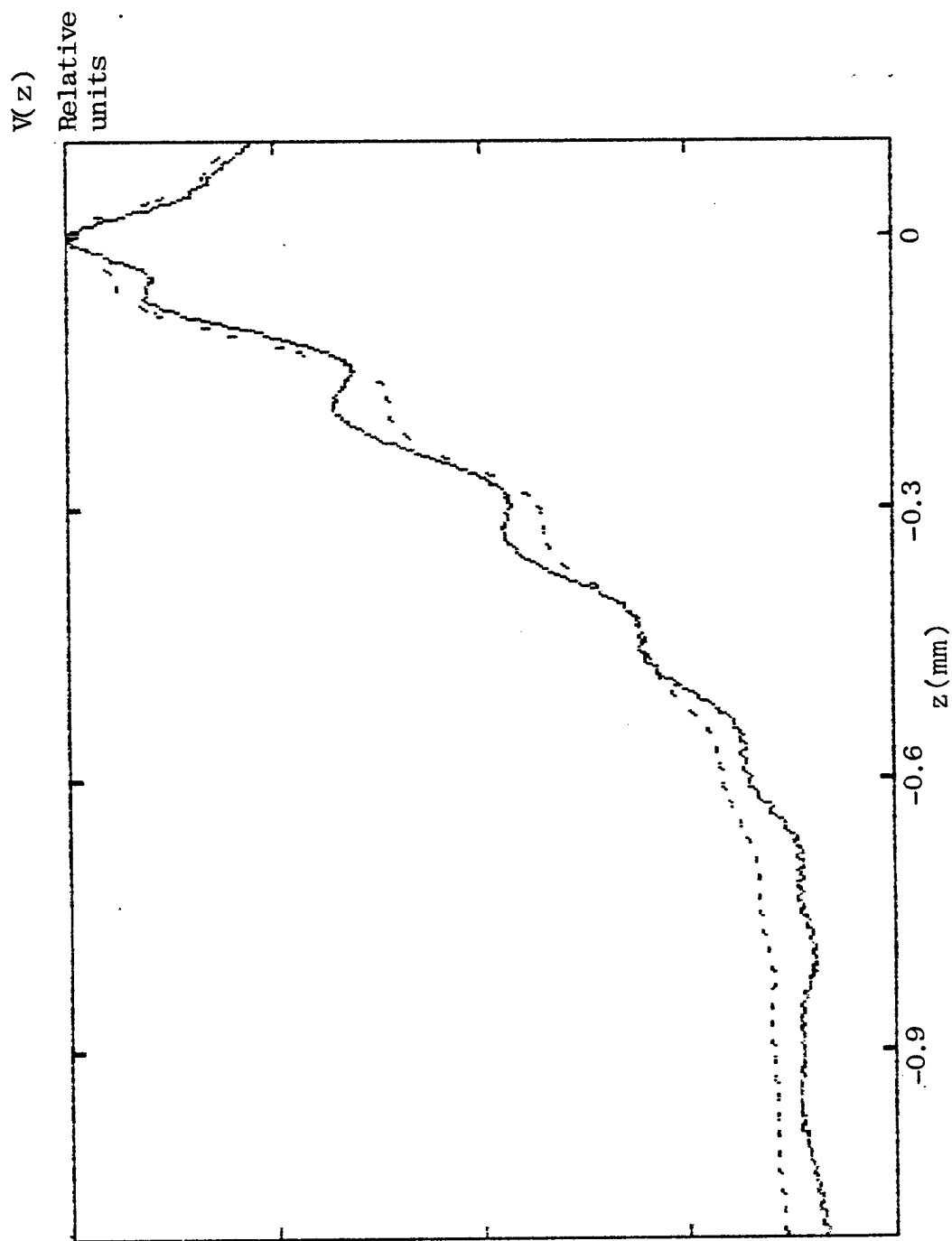


Fig. 3.1  $V(z)$  of Teflon for a slot aperture lens: observed (solid) and calculated using the angular spectrum approach (dashed).



**Fig. 3.2**  $V(z)$  of glass for a slot aperture lens: observed (solid) and calculated using the angular spectrum approach (dashed).

### 3.2 Ray approach

#### 3.2.1 Calculation of the specularly reflected contribution $V_G(z)$

The slot lens pupil function  $P(x,y)$  (3.1.1) can be expressed in terms of cylindrical coordinates  $(\rho, \phi)$  as

$$P(\rho, \phi) = \text{circ}\left(\frac{\rho \cos \phi}{w}\right) \text{circ}\left(\frac{\rho}{R_a}\right)$$

The geometric contribution for the slot lens may now be expressed in a manner similar to expression (2.3.14) as

$$V_G(z) = - \frac{T_{LW}(0) T_{WL}(0) \ell(0) \exp(2i k_w (D/n+f+z))}{M_1} \cdot \frac{4}{\pi R_a^2} \cdot \int_0^{\pi/2} \int_0^{R_a} \exp\left(\frac{ik_w \rho^2}{2n(-u)}\right) \sum_i A_{1i} \exp\left(\frac{-\rho^2}{B_{1i}^2}\right) P_1\left(\frac{\rho}{M_1}\right) P_2(\rho) \rho \, d\rho \, d\phi, \quad (3.2.1)$$

where  $A_{1i}$  and  $B_{1i}$  are defined in (2.3.15). In (3.2.1) integration over  $\phi$  need be carried out only from 0 to  $\pi/2$ , owing to the four-fold symmetry of the slot aperture lens. The factor of 4 is then introduced to account for the contribution of all four quadrants.

Using the slot lens pupil function, the integral over  $\rho$  in (3.2.1) can be carried out analytically, resulting in:

$$V_G(z) = - \frac{T_{LW}(0) T_{WL}(0) \ell(0) \exp(2i k_w (D/n+f+z))}{\pi R_a^2 M_1} \cdot 4 \cdot \int_0^{\pi/2} \sum_i A_{1i} \frac{n B_{1i}^2(-u)}{ik_w B_{1i}^2 - 2n(-u)} \cdot \left[ \exp\left(\frac{ik_w \rho_T^2}{2n(-u)}\right) \cdot \exp\left(\frac{-\rho_T^2}{B_{1i}^2}\right) - 1 \right] d\phi. \quad (3.2.2)$$

where

$$\begin{aligned} \rho_T &= \frac{w_1}{\cos \phi}, & \phi &< \cos^{-1} \left( \frac{w_1}{R_a} \right) \\ \rho_T &= R_a, & \phi &> \cos^{-1} \left( \frac{w_1}{R_a} \right) \end{aligned}$$

and

$$\begin{aligned} w_1 &= w M_1, & M_1 &< 1 \\ w_1 &= w, & M_1 &> 1. \end{aligned}$$

Introduction of the slot aperture reduces the symmetry of the lens, thus the above integral cannot be further evaluated analytically, and numerical integration is used instead. The result of this calculation is plotted in Fig. 3.3 and compared with experimental measurements. The ray-theoretical  $V_G(z)$  does not agree with measurement as well as the angular spectrum  $V_G(z)$  (Fig. 3.1). This could be due, in part, to the fact that the geometric approach ignores diffraction in water, which may be more significant for the slot aperture lens than for circular lens.

The advantage of the ray approach outlined above is that it requires only a single integration over  $\phi$ . The angular spectrum approach requires a double integral over  $(x,y)$ , which is much more computationally intensive.

### 3.2.2 Calculation of the leaky contribution $V_L(z)$

As discussed in Chapter II, leaky rays emanating from the sample surface form a ring focus of radius  $\rho_R$  in the lens rod of the circular lens. The slot aperture allows only portions of this ring to be formed. Thus, neglecting diffraction, the leaky contribution  $V_L(z)$  in the slot lens is the same as for circular lens but scaled by the ratio of the length of arc exposed by the slot to the total circumference of the focal ring or

$$V_L(z) = V_{Lcirc}(z) \cdot \frac{2 \sin^{-1}(w / \rho_R)}{\pi} \quad (3.2.3)$$

where  $w$  is the half-width of the slot.

### 3.2.3 The total voltage $V(z)$

The total voltage response  $V(z)$  of the slot aperture lens for a glass sample is obtained by adding  $V_G(z)$  and  $V_L(z)$  and plotted in Fig. 3.4 for comparison with the measurement.



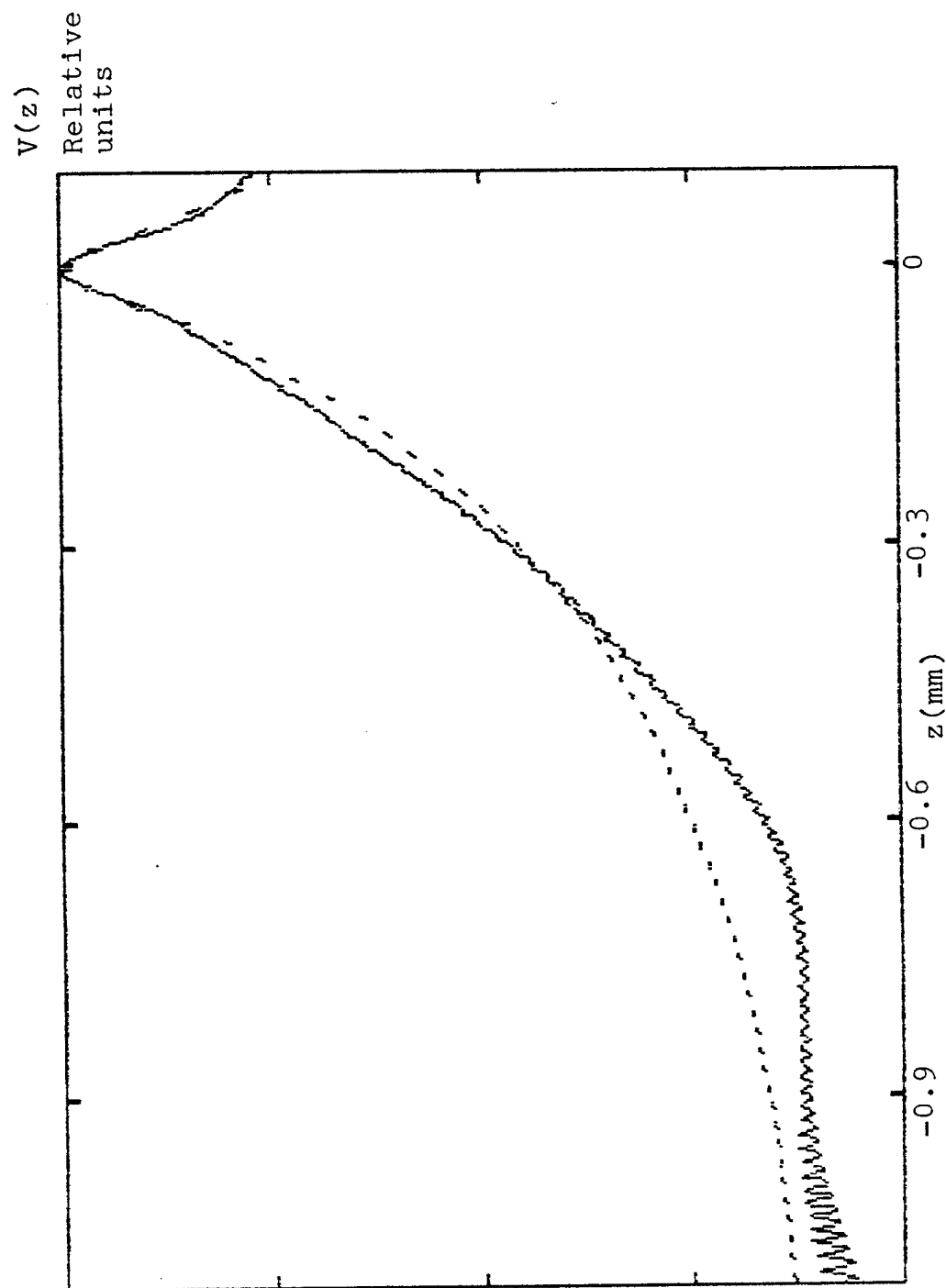


**Fig. 3.3**  $V(z)$  of Teflon for a slot aperture lens: observed (solid) and calculated using the diffraction-corrected ray approach (dashed).

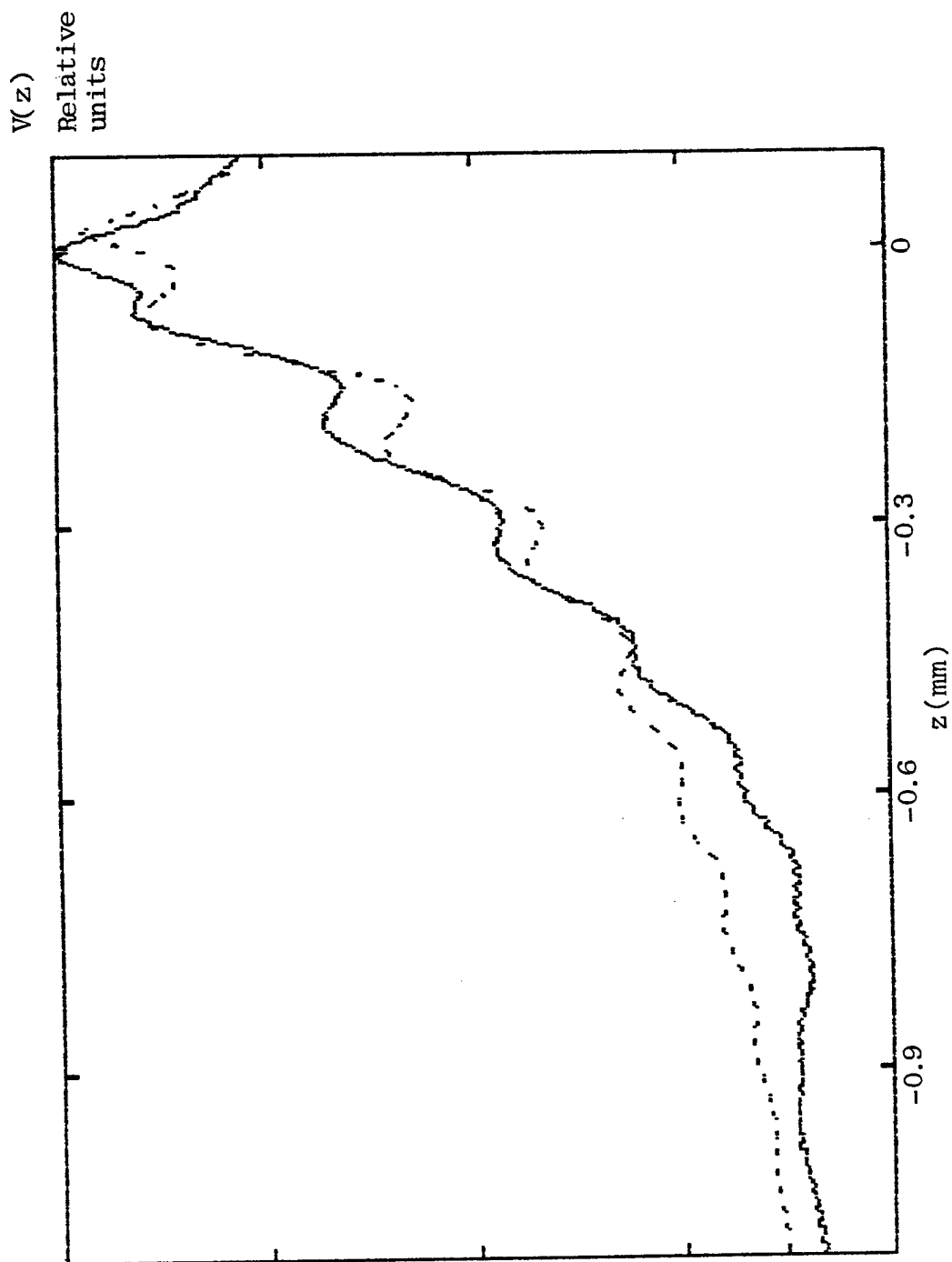


**Fig. 3.4**  $V(z)$  of glass for a slot aperture lens: observed (solid) and calculated using the diffraction-corrected ray approach (dashed).

### 3.3 Extracting $v_R(\phi)$ of an anisotropic material using the slot lens

A slot lens with a slot width  $w$  of 1 mm was constructed and used to obtain  $V(z)$  measurements of a Y-cut quartz sample for various orientation of the slot relative to the crystalline X-axis. The resulting  $V(z)$  curves for orientation angles of  $0^\circ$  and  $90^\circ$  are displayed in Figs. 3.5 and 3.6, respectively. To obtain the Rayleigh wave velocity  $v_R$  as a function of propagation direction  $\phi$ , these curves were processed using the algorithm described in Chapter II. The resulting values are plotted in Fig. 3.7 along with the accepted dispersion curve  $v_R(\phi)$  (Kushibiki [4]). For illustration, a processed  $V_I(z)$  curve, defined in Chapter II, is shown in Fig. 3.8 for  $\phi = 0^\circ$ . Higher precision in calculating  $v_R$  from experimental curves require more periods in  $V_I(z)$ . This occurs in materials with low Rayleigh wave velocities, since the period of the interference decreases with decreasing  $v_R$ , as can be seen from (2.4.1). For materials with high Rayleigh velocities higher acoustic wave frequencies should be used. Alternatively, it is possible to simply measure  $V(z)$  over a greater range in  $z$ , but this would require a higher signal-to-noise ratio and possibly a different lens geometry since the signal level drops off significantly for large defocus distance  $|z|$ .

It has been shown that a slot lens does indeed launch Rayleigh waves in a preferential direction and can be used to obtain Rayleigh wave velocities as a function of propagation direction in anisotropic crystals.

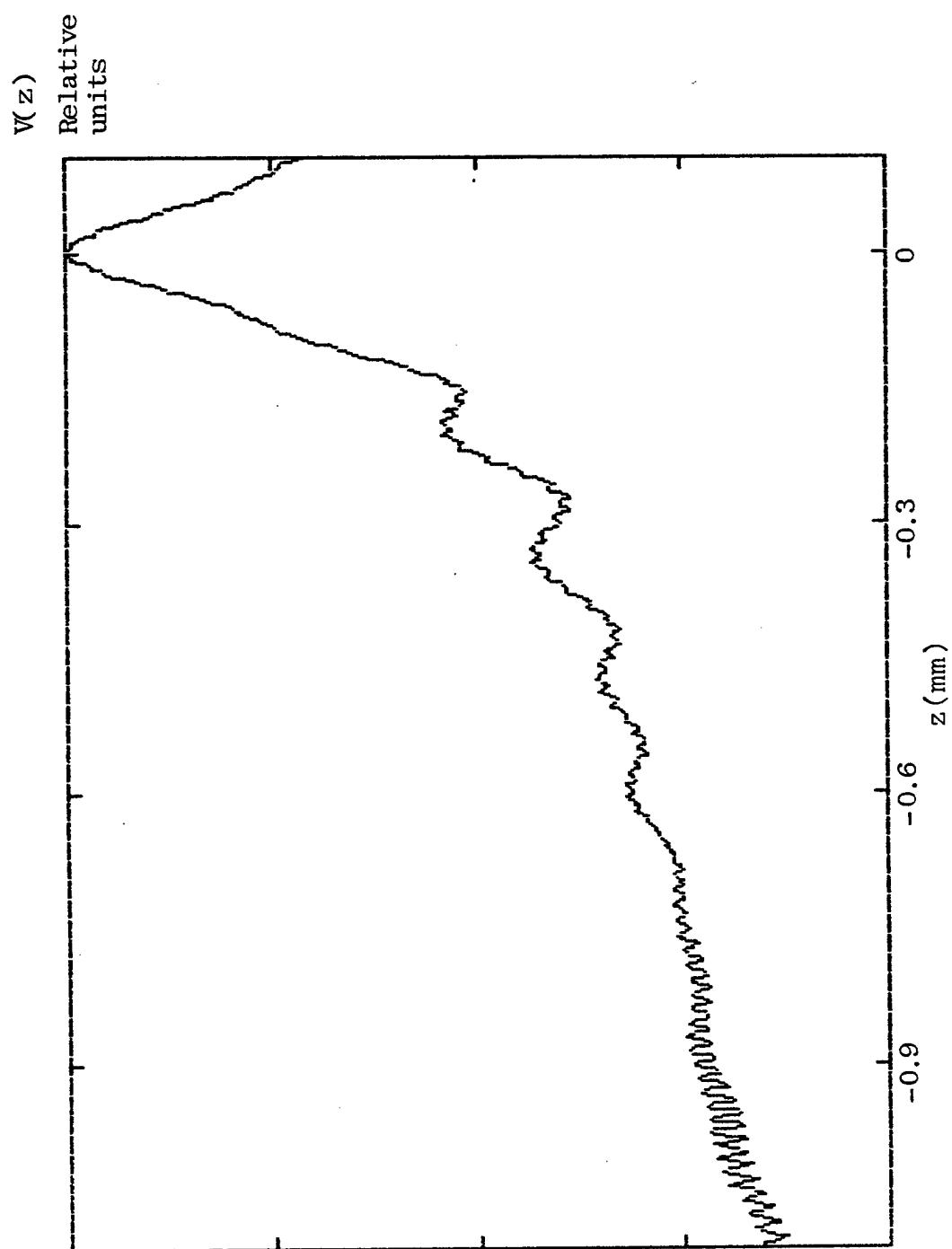


**Fig. 3.5** Observed  $V(z)$  of Y-cut quartz with slot oriented along the crystalline x-axis  
 $(\phi = 0)$ .

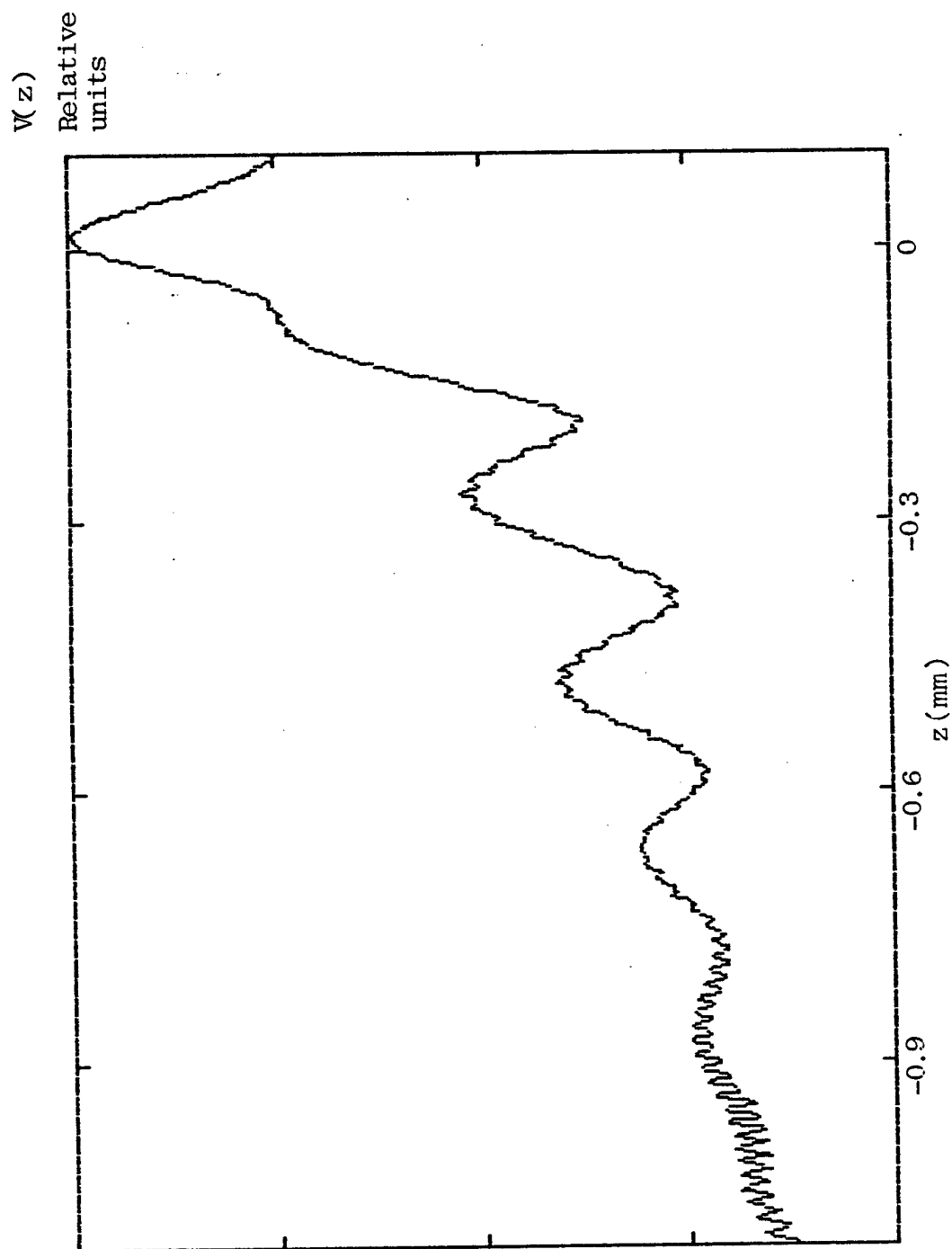
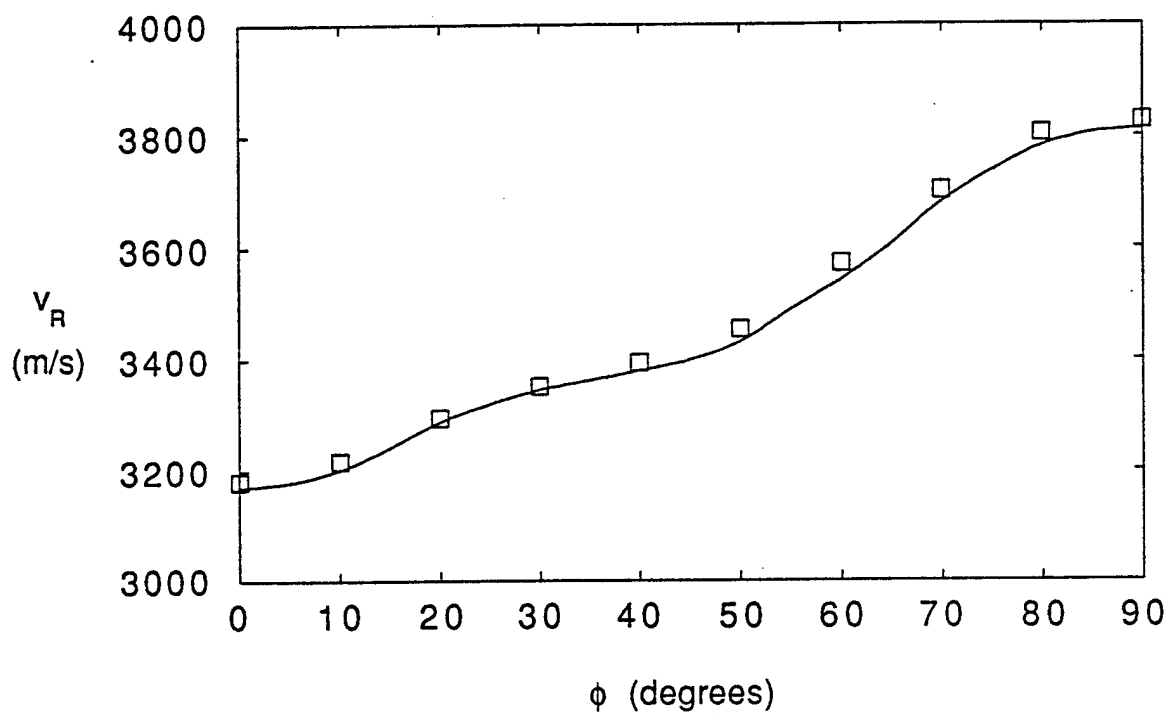
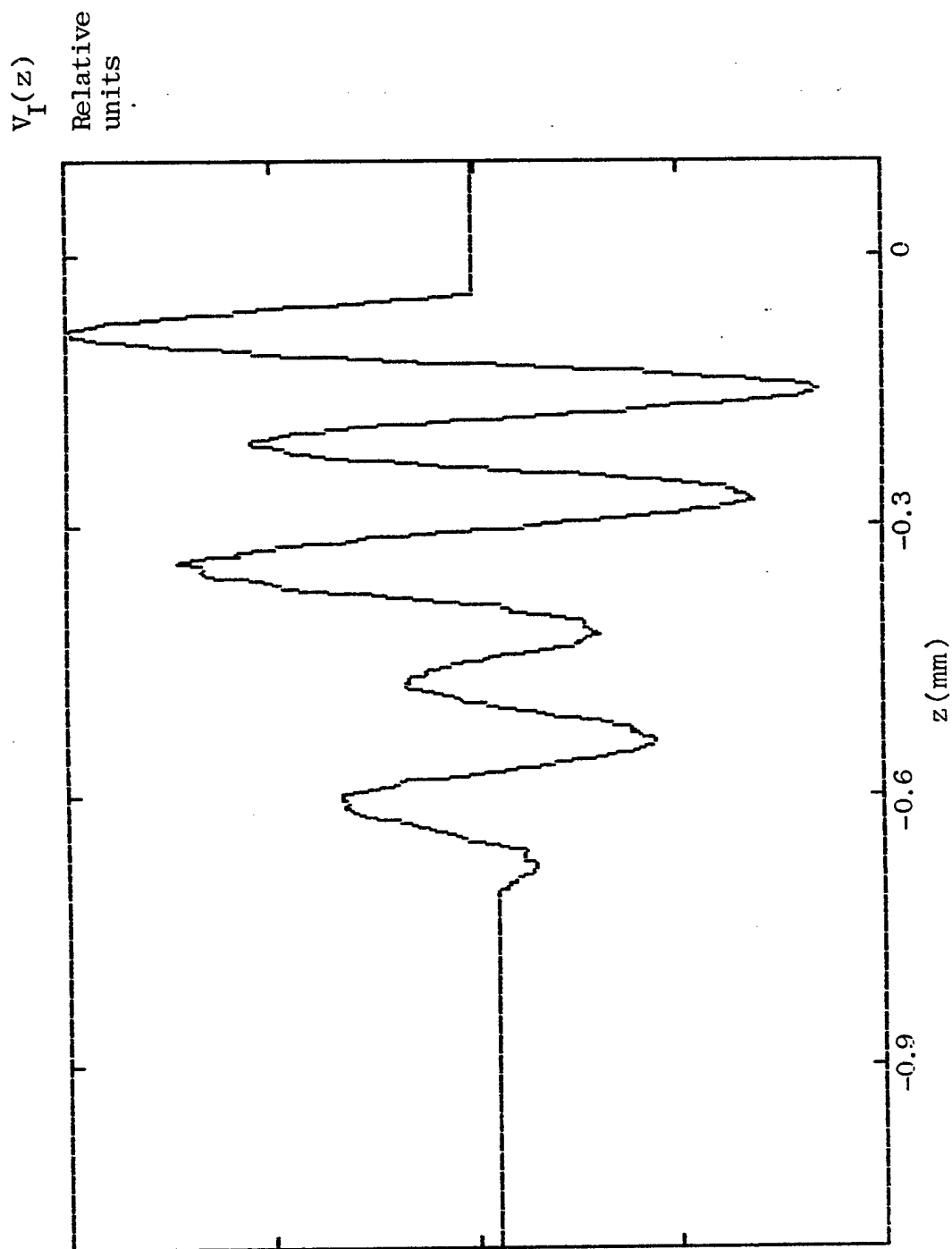


Fig. 3.6 Observed  $V(z)$  of Y-cut quartz with slot oriented at  $90^\circ$  to the crystalline x-axis.



**Fig. 3.7** Rayleigh wave velocity  $v_R$  of Y-cut quartz as a function of direction of propagation  $\phi$  measured from the crystalline x-axis: accepted (solid line) and measured using the slot lens (open boxes).



**Fig. 3.8**  $V_I(z)$  of Y-cut quartz obtained from data measured with slot oriented along the crystalline x-axis ( $\phi = 0$ ).

## Chapter IV

### Modelling of $V(x)$ measurements across a surface breaking crack using ray theory.

This chapter is concerned with a theoretical treatment of the microscope response of a sample surface containing a discontinuity such as a surface-breaking crack. This defect will be assumed to be of infinitesimal thickness, straight, symmetrical in a planar surface and long compared with the diameter of the spot produced by the incident acoustic beam. Of particular interest are line-scan measurements, called  $V(x)$ , obtained by keeping the lens at a constant defocus distance  $z$  and scanning in  $x$  perpendicular to the discontinuity (see Fig. 1.5). Crack displacement  $x$  is defined as the distance between the lens axis and the crack, with  $x = 0$  corresponding to the lens being centered directly above the crack. The analysis will first involve the slot lens, where the angular range of surface ray paths is restricted, and then the circular lens can be viewed as simply a special case of the slot lens with slot half-width  $w$  equal to the aperture radius  $w = R_a$ .

The total response  $V(x,z)$  of the microscope to a surface containing a crack may be expressed as

$$V(x,z) = V_G(z) + V_T(x,z) + V_{\text{refl}}(x,z), \quad (4.1)$$

where  $V_G(z)$  is the specularly reflected component,  $V_T(x,z)$  is due to the leaky waves transmitted through the crack as well as those leaky waves that propagate unimpeded by the crack, and  $V_{\text{refl}}(x,z)$  is the contribution of the leaky waves scattered from the crack. The ray paths involved in determining these contributions are shown in Fig. 4.1. Here both the crack and the lens are assumed to have inversion symmetry,  $V(x,z) = V(-x,z)$ , i.e. the same response is detected on either side of the crack. It will be assumed that when a surface wave strikes a crack, a portion of the incident wave is transmitted with a field



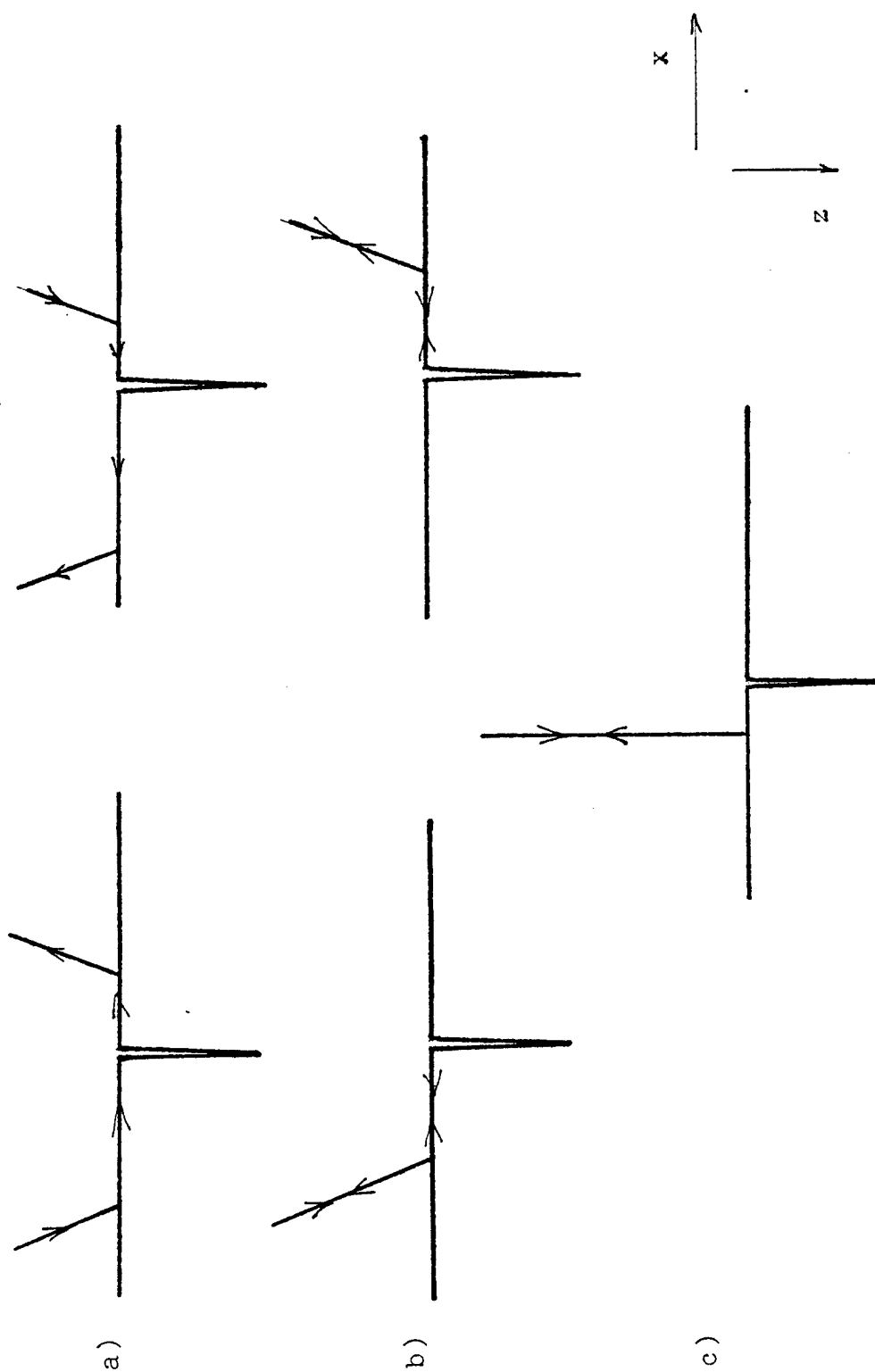


**Fig. 4.1** Surface-wave and specular ray paths for various contributions to  $V(x,z)$ :

(a) transmitted through the crack , (b) reflected from the crack, and

(c) specularly reflected from the surface.

transmission coefficient  $T_c$ , and a portion is reflected with a field reflection coefficient  $R_c$ . The dependence of  $T_c$  and  $R_c$  on the angle of incidence of the surface wave will be ignored on the basis that the predicted variation near normal incidence is weakly dependent on angle, as shown by Angel and Achenbach in [3].

#### 4.1 Specularly reflected component $V_G(z)$

The crack is assumed to be of infinitesimal thickness, therefore the specularly reflected component  $V_G$  is unperturbed by the crack. Since  $V_G$  is the same as for the defect-free surface, it is independent of the crack position  $x$  and only depends on defocus distance  $z$ . Thus,  $V_G(z)$  is evaluated by the methods described in Chapters II and III that were developed for defect-free substrates.

#### 4.2 Transmitted component $V_T(x,z)$

It is instructive first to review the leaky ray structure for the defect-free surface when the lens is closer than focus or  $z < 0$ . Some rays cross the lens surface at  $\rho = \rho_R$  and strike the sample surface at the Rayleigh critical angle  $\theta_R$ , thus launching Rayleigh surface waves in the plane of incidence. The locus of all such launch points forms a circle, called Rayleigh circle, in the case of a circular lens, or restricted circular arcs in the case of the slot lens. The radius  $c$  of the Rayleigh circle is found from

$$c = |z| \tan (\theta_R) . \quad (4.2.1)$$

The surface waves focus at the intersection with the lens axis and diverge beyond. As discussed in Chapter II, the leaky rays form a circle-shaped focus of radius  $\rho_R$  within the

lens rod, located at  $f_x$  above the lens surface, which is limited to circular arcs for the slot lens. The leaky-ray bundle reaching the transducer is defined by rays that cross the lens surface from  $\rho = \rho_{Rmin}$  to  $\rho = \rho_{Rmax}$ , as shown in Fig. 4.2. This ray bundle originates from points on the sample surface in the radial plane lying between  $\rho = c_{min}$  and  $\rho = c_{max}$ . The geometric quantities  $c_{min}$ ,  $c_{max}$ ,  $\rho_{min}$ ,  $\rho_{max}$  are derived in Appendix A. Thus, the contribution  $V_L(z)$  is due to a distribution of effective leaky ray sources on the sample surface, whose locus, shown in Fig. 4.3, is two sections of a ring, bounded by circles of radii  $c_{min}$  and  $c_{max}$  and the projection of the slot aperture onto the sample surface.

When the crack is sufficiently displaced from the lens axis, some surface rays are leaked into water without interacting with the crack, and therefore their contribution to the transducer voltage is the same as in the defect-free case. Voltage due to those rays that are transmitted through the crack is scaled by the crack transmission coefficient  $T_c$  (see Fig. 4.4).

Transmitted contribution  $V_T(x,z)$  is given by

$$V_T = V_L(z) \cdot (Q_R(x,z) + Q_L(x,z)), \quad (4.2.2)$$

where  $V_L(z)$  is the contribution to the  $V(z)$  due to the leaky surface waves for the defect-free surface, and  $Q_R(x,z)$  and  $Q_L(x,z)$  are fractional contributions to  $V(x,z)$  from the rays re-radiated into water on the right and left sides of the lens, respectively, as shown in Fig. 4.1a. In the absence of a crack  $Q_R = Q_L = 0.5$ .

First, only rays launched on the left side of the crack and propagating to the right will be considered. The  $V_T(x,z)$  contribution to the  $V(x,z)$  will be assumed to be proportional to the total field flux leaked into water from the area shown shaded in Fig. 4.3. This assumption is most valid for a long lens rod where the phase variation of the field at the transducer is small. The factor  $Q_R$  can be seen to be

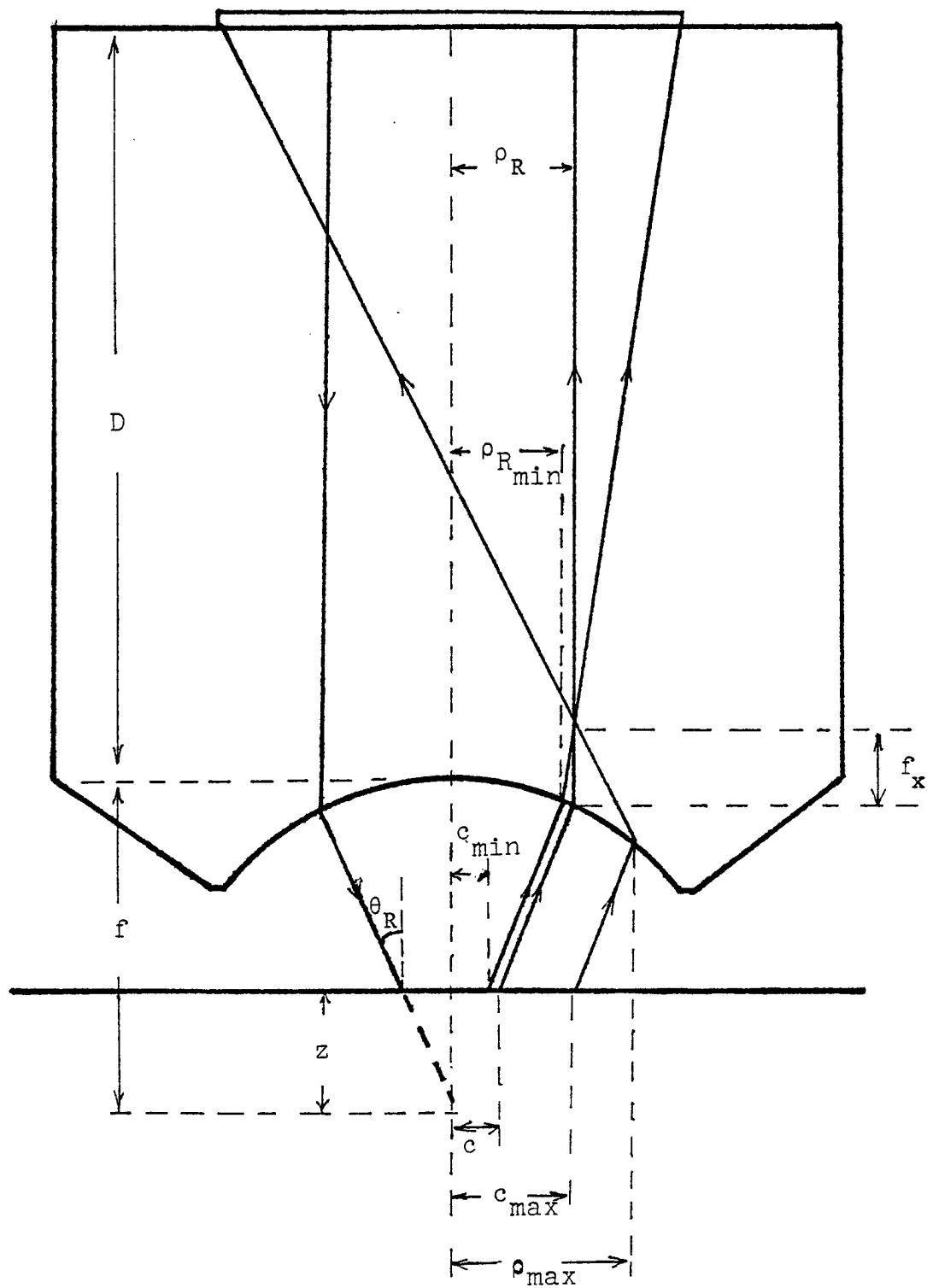
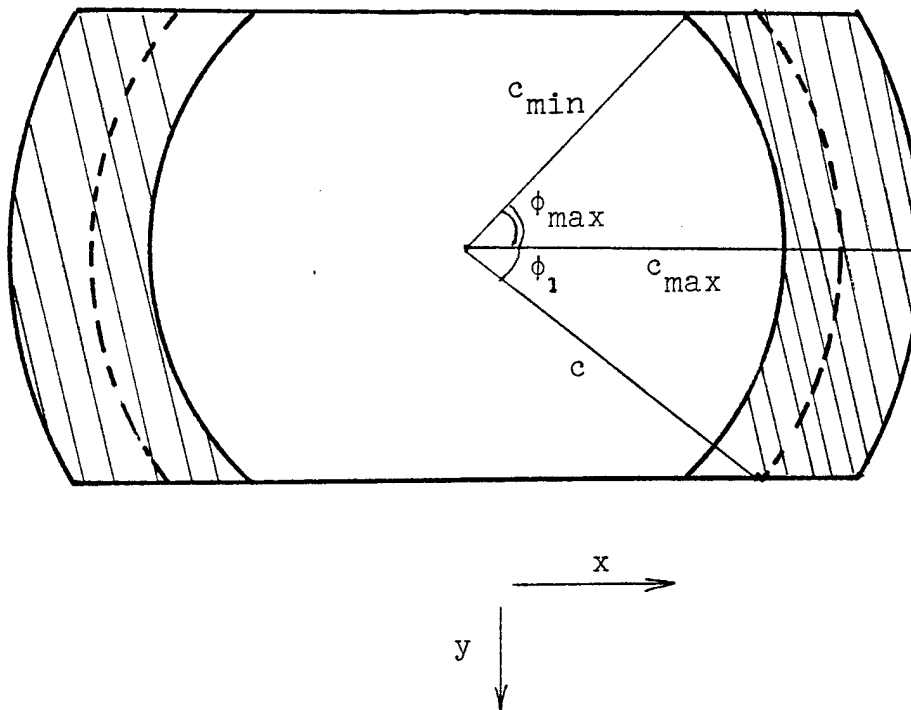
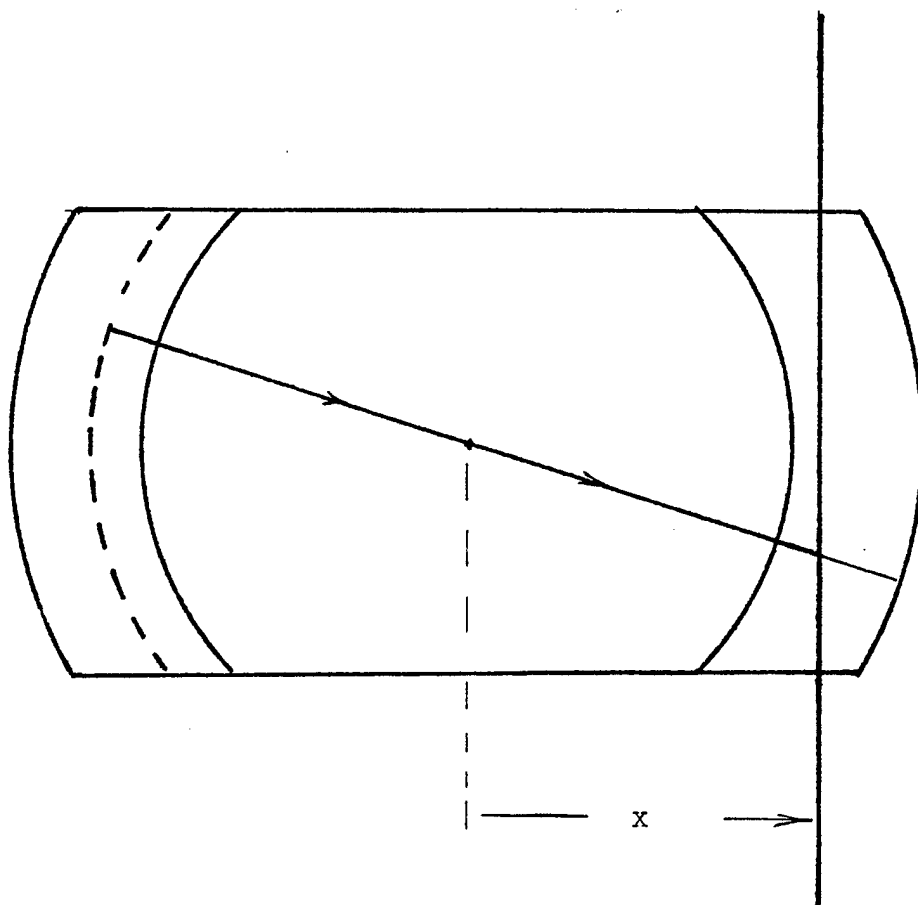


Fig. 4.2 Leaky ray bundle in the  $x$ - $z$  plane.



**Fig. 4.3** Distribution of the leaky ray flux (shaded) that excites the transducer, defined on the sample surface. Note also the definition of  $\phi_1$  and  $\phi_{\max}$  in the sample plane.



**Fig. 4.4** Geometry of a surface ray is excited on the left and leaks energy to the right of lens axis . After the ray crosses the crack the leaky field is reduced by the factor  $T_c$ .

$$Q_R = \frac{Q_1 T + 1 - Q_1}{2}, \quad (4.2.3)$$

where  $Q_1$  is the fraction of the ray flux intercepted by the crack and therefore scaled by  $T_c$ , and  $(1 - Q_1)$  is the fraction of the ray flux that is unobstructed. It can be seen from Fig. 4.4 that the factor  $Q_1$  can be expressed as:

$$Q_1 = \frac{\text{Area of obstructed part of Rayleigh ring}}{\text{Total area of Rayleigh ring section}}. \quad (4.2.4)$$

The above relation simply views all leaky launch points as equally contributing to  $V_T(x,z)$ . Total area of the Rayleigh ring may be found approximately from the relation

$$\frac{2\phi_1}{\pi} \cdot \frac{\pi(c_{\max}^2 - c_{\min}^2)}{2} = \phi_1 (c_{\max}^2 - c_{\min}^2). \quad [4.2.5]$$

where  $\phi_1$ , illustrated in Fig. 4.3 is the effective half-angle of the ring arc, defined in terms of the slot half-width  $w$  at the lens aperture by

$$\begin{aligned} \phi_1 &= \sin^{-1}(w / \rho_R), & w < \rho_R \\ &= \pi / 2, & w > \rho_R. \end{aligned} \quad (4.2.6)$$

The second equality in (4.2.6) applies to situation where none of the area defined by  $c_{\min} < \rho_R < c_{\max}$  is obstructed by the slot. All azimuthal angles  $\phi$  are defined relative to the direction of the  $x$ -axis. As the lens is translated to the left along the  $x$ -axis, there are four distinct ranges of crack position  $x$ , shown in Fig. 4.5. In Fig. 4.5  $\phi_{\max}$  is the azimuthal angle coordinate which forms one of the boundaries of the Rayleigh ring arc, whose value when defined at the lens aperture is

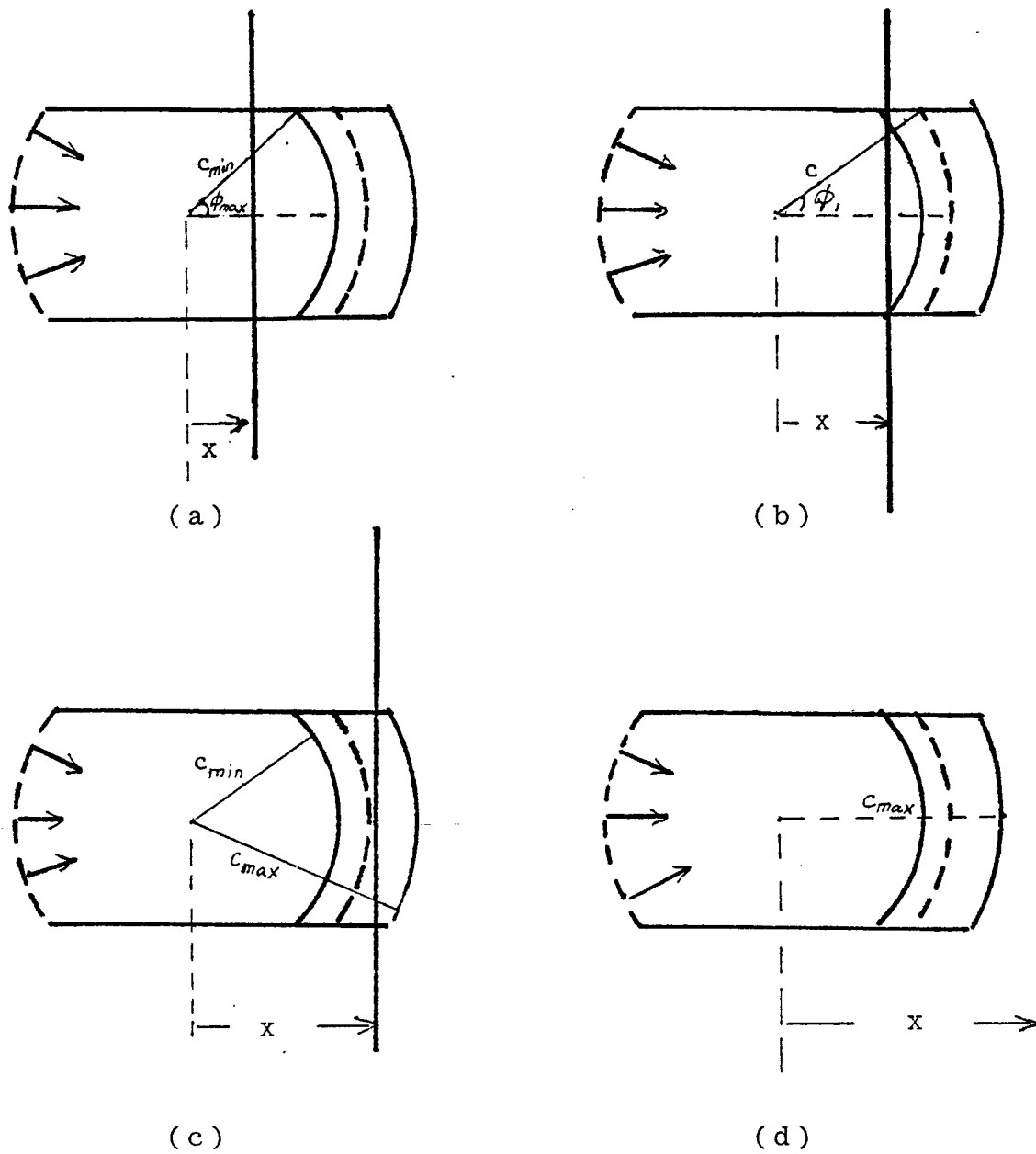


**Fig. 4.5** Distinct ranges of crack displacement that lead to different geometric relations in determining  $Q_R$ :

- (a)  $0 < x < c_{\min}$ ,      (b)  $c_{\min} \cos \phi_{\max} < x < c_{\min}$   
(c)  $c_{\min} < x < c_{\max}$ ,      (d)  $x > c_{\max}$ .



$$\begin{aligned}
\phi_{\max} &= \sin^{-1}(w / \rho_{\min}), & w < \rho_{\min} \\
&= \pi / 2, & w > \rho_{\min}
\end{aligned} \tag{4.2.7}$$

For Range 1, where  $0 < x < c_{\min} \cos \phi_{\max}$ , all surface rays are intercepted by the crack before leaking into water and, therefore,  $Q_1 = 1$ . Substituting  $Q_1$  into (4.2.3) gives  $Q_R = T_0/2$ .

For Range 2, where  $c_{\min} \cos \phi_{\max} < x < c_{\min}$ , some ray paths are no longer obstructed by the crack. Upon examination of Fig. 4.5b and in accordance with (4.2.4),  $Q_1$  may be found approximately from the expression

$$\begin{aligned}
Q_1 &= \frac{2}{\phi_1 (c_{\max}^2 - c_{\min}^2)} \int_{c_{\min}}^{c_{\max} \cos^{-1}(x/\rho)} \int_0^{\phi} d\phi \rho \, d\rho = \\
&= \frac{2}{\phi_1 (c_{\max}^2 - c_{\min}^2)} \cdot \int_{c_{\min}}^{c_{\max}} \rho \cos^{-1}(x/\rho) \, d\rho .
\end{aligned} \tag{4.2.8}$$

Similarly, for Range 3, where  $c_{\min} < x < c_{\max}$ , it follows from Fig. 4.5c and (4.2.4) that

$$Q_1 = \frac{2}{\phi_1 (c_{\max}^2 - c_{\min}^2)} \cdot \int_x^{c_{\max}} \rho \cos^{-1}(x/\rho) \, d\rho . \tag{4.2.9}$$

For Range 4, where  $x > c_{\max}$ , all surface rays propagate unobstructed by the crack, thus  $Q_1 = 0$ , and  $Q_R = 0.5$ .

Surface rays that are excited on the right and detected on the left will be now considered. As can be seen in Fig. 4.6 there are three distinct ranges of crack position  $x$ .

For Range 1, where  $x < c \cos \phi_1$ , all rays are intercepted by the crack, so that  $Q_L = T_c / 2$ .

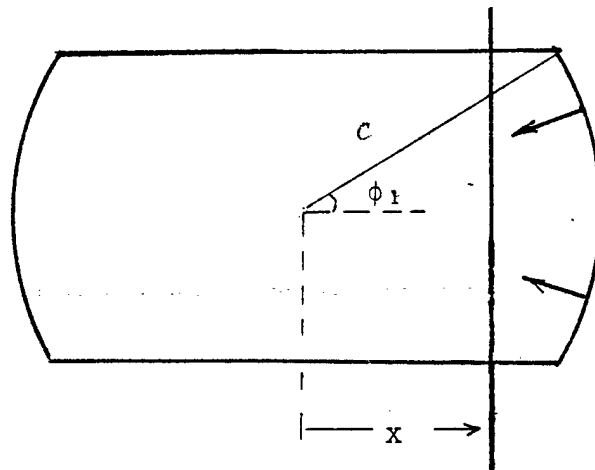
For Range 2, where  $c \cos \phi_1 < x < c$ , it can be seen from Fig. 4.6b that

$$Q_L = 0.5 \frac{2\phi T + 2(\phi_1 - \phi)}{2\phi_1} = \frac{\phi T + \phi_1 - \phi}{2\phi_1}, \quad (4.2.10)$$

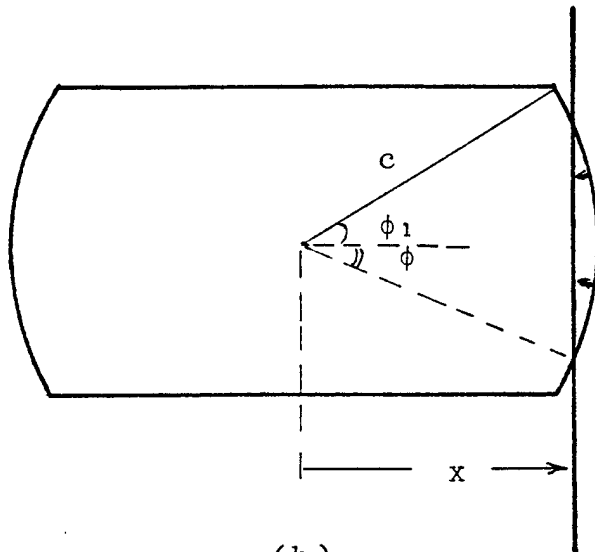
where  $\phi$  in Fig. 4.6b is defined as  $\phi = \cos^{-1}(x / c)$ .

For Range 3, where  $x > c$ , all rays pass unobstructed, so that  $Q_L = 0.5$ .

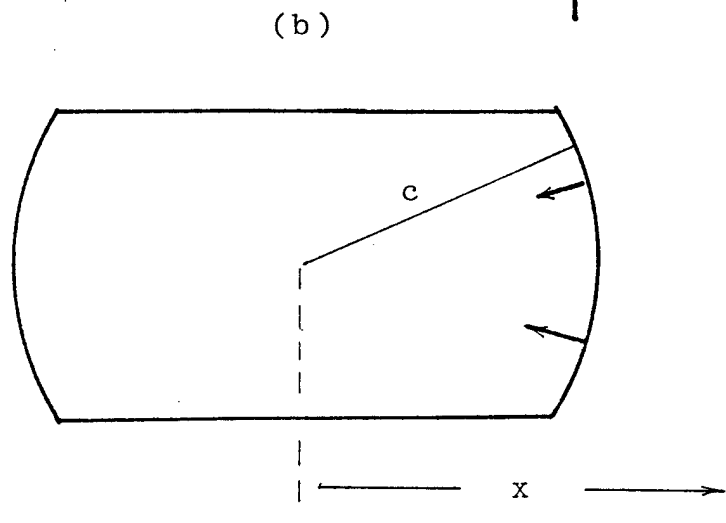
The transmitted component  $V_T(x, z)$  can be viewed as a reduction of the leaky component  $V_L(z)$  due to the presence of the crack. The above analysis enables the determination of  $V_T(x, z)$  for  $z < 0$ . When  $z > 0$ , the surface waves diverge away from the lens and, thus, there is no leaky component  $V_L(z)$  intercepted by the transducer, as discussed in Chapter II. Consequently,  $V_T(x, z) = 0$  for  $z > 0$ .



(a)



(b)



(c)

**Fig. 4.6** Distinct ranges of crack displacement that lead to different geometric relations in determining  $Q_L$ : (a)  $0 < x < c \cdot \cos \phi_1$ , (b)  $c \cdot \cos \phi_1 < x < c$ , (c)  $x > c$

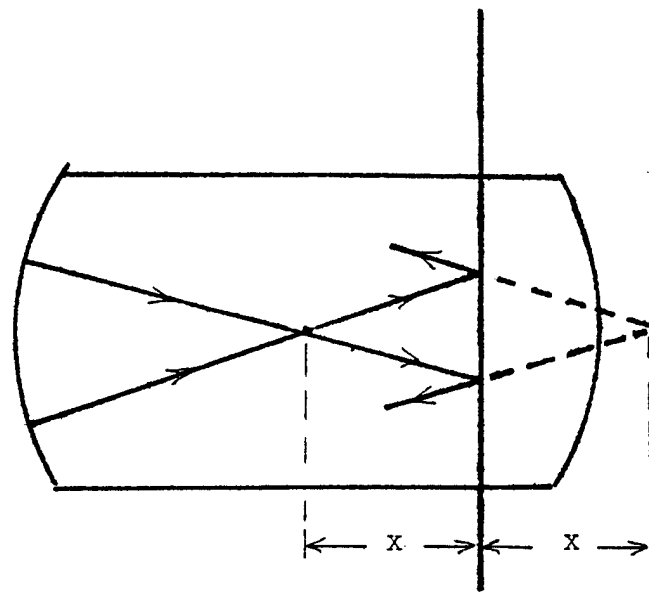
### 4.3 Reflected surface wave contribution $V_{\text{refl}}(x)$ :

In Fig. 4.7, the reflected contribution to  $V(x,z)$  has two components, defined by

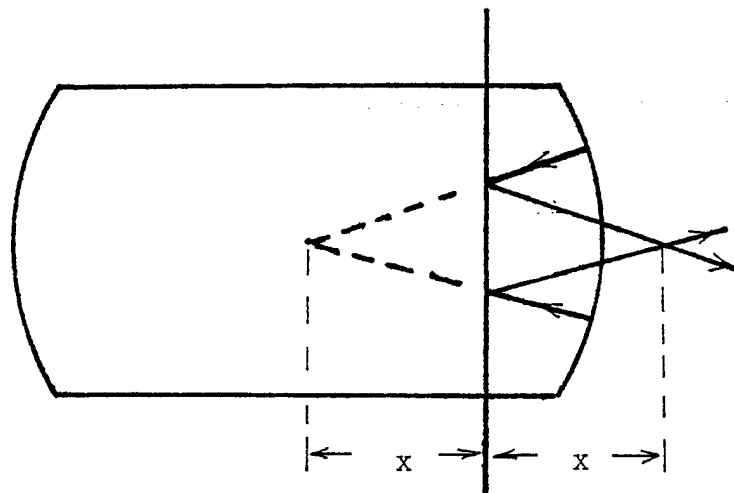
$$V_{\text{refl}}(x,z) = V_{\text{RR}}(x,z) + V_{\text{RL}}(x,z) . \quad (4.3.1)$$

where  $V_{\text{RR}}$  is the contribution due to the surface waves incident on the discontinuity from the right (Fig. 4.7a) and  $V_{\text{RL}}$  is due to the waves incident from the left (Fig. 4.7b). Further examination of the figure reveals that  $V_{\text{RR}} = 0$  for  $x > c$  and  $z < 0$ . In this case the only contribution to  $V_{\text{refl}}$  is from the left. Let  $V_{\text{refl}}(x,z) = V_{\text{R}}(x,z)$  in this range. First,  $V_{\text{R}}(x,z)$  will be found and then both  $V_{\text{RR}}(x,z)$  and  $V_{\text{RL}}(x,z)$  will be expressed in terms of  $V_{\text{R}}(x,z)$  for all  $x$  and  $z$ .

The various field amplitude factors due to focusing and phase delays due to propagation are now to be determined. Recall that in Chapter II determination of the leaky component  $V_{\text{L}}(z)$ , a ray field of amplitude  $|U(\rho_{\text{R}})|$  is incident on the lens surface at the critical radius  $\rho = \rho_{\text{R}}$  where it is refracted into the water to strike the sample surface at  $\rho = c$ . Spherical focusing by the lens and propagation in the lens rod and water introduces the amplitude factor  $\rho / c$  and the phase factor  $\exp i k_{\text{w}} (D/n + f + z \sec \theta_{\text{R}})$  (see Fig. 4.2). Propagation along the surface to the crack results in the phase factor  $\exp i k_{\text{p}}(x - z \tan \theta_{\text{R}})$ , where  $k_{\text{p}}$  is the pole of the water-substrate reflection coefficient:  $k_{\text{p}} = k_{\text{R}} + i\alpha_{\text{L}}$  ([2]). Reflection from the crack introduces the factor  $R_{\text{c}}$ . Traversing the return path to the transducer causes the repetition of the phase changes involved in forward propagation as well as an additional amplitude term  $\exp -\alpha_{\text{L}} (x - z \tan \theta_{\text{R}})$  due to leakage into water. Transmission through the lens-water interface is taken into account by using the field transmission coefficients  $T_{\text{LW}}(\rho_{\text{R}})$  and  $T_{\text{WL}}(\rho_{\text{R}})$  mentioned in Chapter II. In addition, as shown by Bertoni [2], there is a coefficient  $E$  associated with the excitation and re-radiation of the surface waves, given by



( a )



( b )

**Fig. 4.7** Focusing of surface rays reflected from the crack on the (a) left and (b) right side of the Rayleigh circle.

$$E = -2 \alpha_L \sqrt{\frac{2 \pi |z|}{k_w \cos^3 \theta_R}} \exp(-i\pi/4). \quad (4.3.2)$$

When the distance between the excitation and re-radiation of surface waves is small:  $(x - x_i) < \sqrt{|z| \lambda_w / \cos^3 \theta_R}$ , this coefficient must be modified, as described by Bertoni [2]. Usually, in modelling surface wave-crack interaction, such correction will become necessary only when the crack is near the edge of the Rayleigh circle, i.e.  $x \approx c$ . In this region, the Rayleigh wave is launched, scattered from the crack, and re-radiated within a very short distance. In this work expression (4.3.2) will be used to determine  $E$  for all  $x$ .

The focusing and spreading of surface wave rays for several Rayleigh wave ray paths is depicted in Fig. 4.8. The surface waves pass through a focus where the lens axis intersects the sample surface and then strike the crack, located at a distance  $x$  from the lens axis, which acts as a plane mirror with a field reflection coefficient  $R_C$ . The surface waves reflected from the crack appear to come from a point source located at a distance  $2x$  from the lens axis denoted by the point  $F$  in the Fig. 4.8. This point source is thus located at the mirror image of the point defined by the lens axis intersection. These reflected waves propagate to the left until they reach the neighborhood of the Rayleigh circle, where the ray fields that leak into the water are refracted by the lens and strike the transducer. Since the surface waves are launched with a radius of curvature of  $c$  and are re-radiated with a radius of curvature  $c + 2x$ , the field amplitude is modified by a factor  $\sqrt{c / (c + 2x)}$ . In addition, the planar focus at the lens axis introduces a phase change of  $-\pi/2$ .

Each of the surface wave rays ( e.g. FB, FA, and FC in Fig. 4.8) radiate into water thereby creating a parallel family of rays at angle  $\theta_R$  with respect to the normal to the surface. Since parallel rays do not spread, there is only angular spreading along the arc BAC. When the radiated ray bundle reaches the lens, it will have a radius of

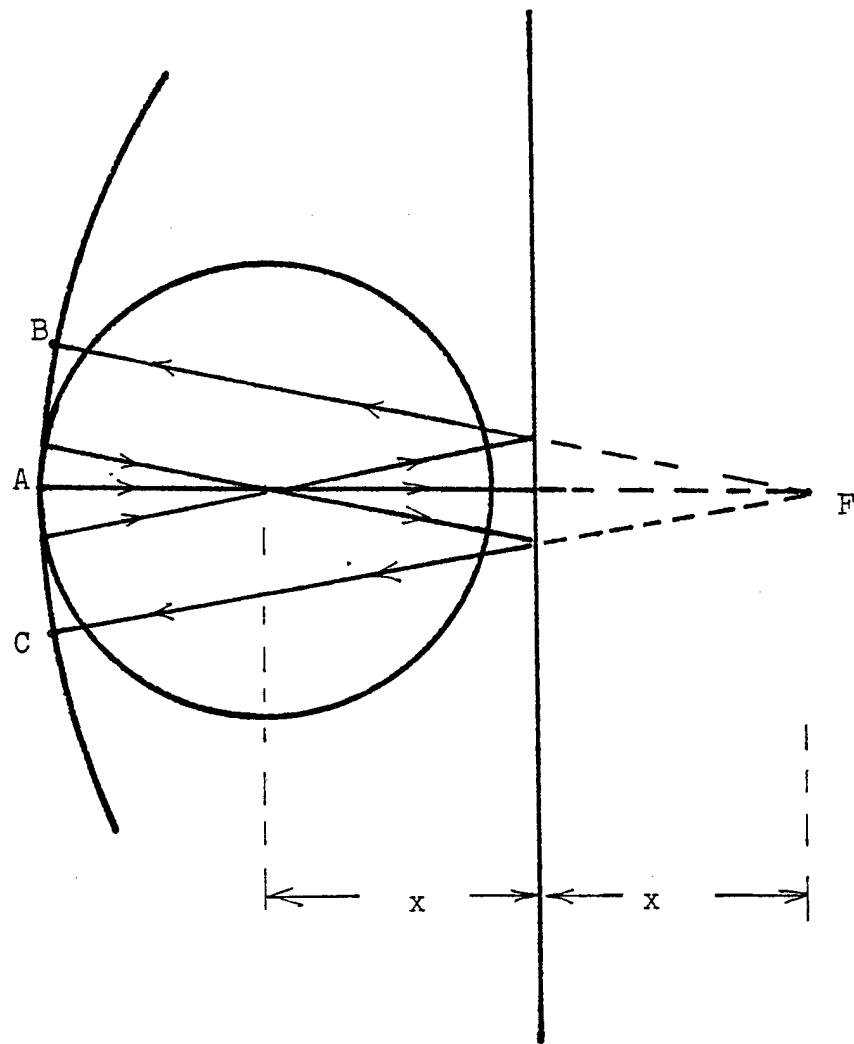


**Fig. 4.8** Divergence of reflected surface waves at the edge of the Rayleigh circle.

curvature of  $\rho_R + 2x$ , and thus a change of amplitude of  $\sqrt{(c+2x)/(\rho_R+2x)}$  resulting from ray spreading in the water.

Since the bundle of radiated rays spreads only in the angular direction, passage through the spherical lens results in two astigmatic foci. The rays radiated along FB, FA, and FC in Fig. 4.8 are parallel to each other and therefore focus at  $f_x$  above the lens surface. For the direction FA the focal length  $f_x$  is the same as  $f_x$  described in Chapter II (see Fig. 2.5). For the focusing of leaky rays in the case of the defect-free surface

$$f_x = \frac{\rho_R}{\tan \theta_R} + \sqrt{R^2 + \rho_R^2}. \quad (4.3.3)$$

See Appendix A for derivation of (4.3.3). It is assumed here that  $f_x$  is the same for all directions. This approximation is most valid for ray paths close to FA, i.e. nearly normal to the crack. The rays that strike the crack at large oblique angles are strongly refracted by the lens and are likely to miss the transducer. For the slot lens all rays incident on the crack strike at nearly normal incidence.

Those rays that were radiated along arcs parallel to BAC in Fig. 4.8 appear to originate from a point on a vertical line going through F, shown in Fig. 4.9. The lens forms an image of this point source at  $f_y$  above the lens surface, where  $f_y$  is shown in Appendix A to be

$$f_y = \frac{(f - R) \rho_R}{2x} + f_x. \quad (4.3.4)$$

For the lens used in this work and for  $x > c$  it follows that  $0 < f_y < D$  and, thus, there is a focus in the lens rod. The ray field therefore suffers a phase change of  $-\pi/2$  due to propagation through each of the two foci at  $f_x$  and  $f_y$  from the lens surface as well as additional factors of  $\sqrt{f_x / (D - f_x)}$  and  $\sqrt{f_y / |D - f_y|}$  due to the spreading in the lens rod.



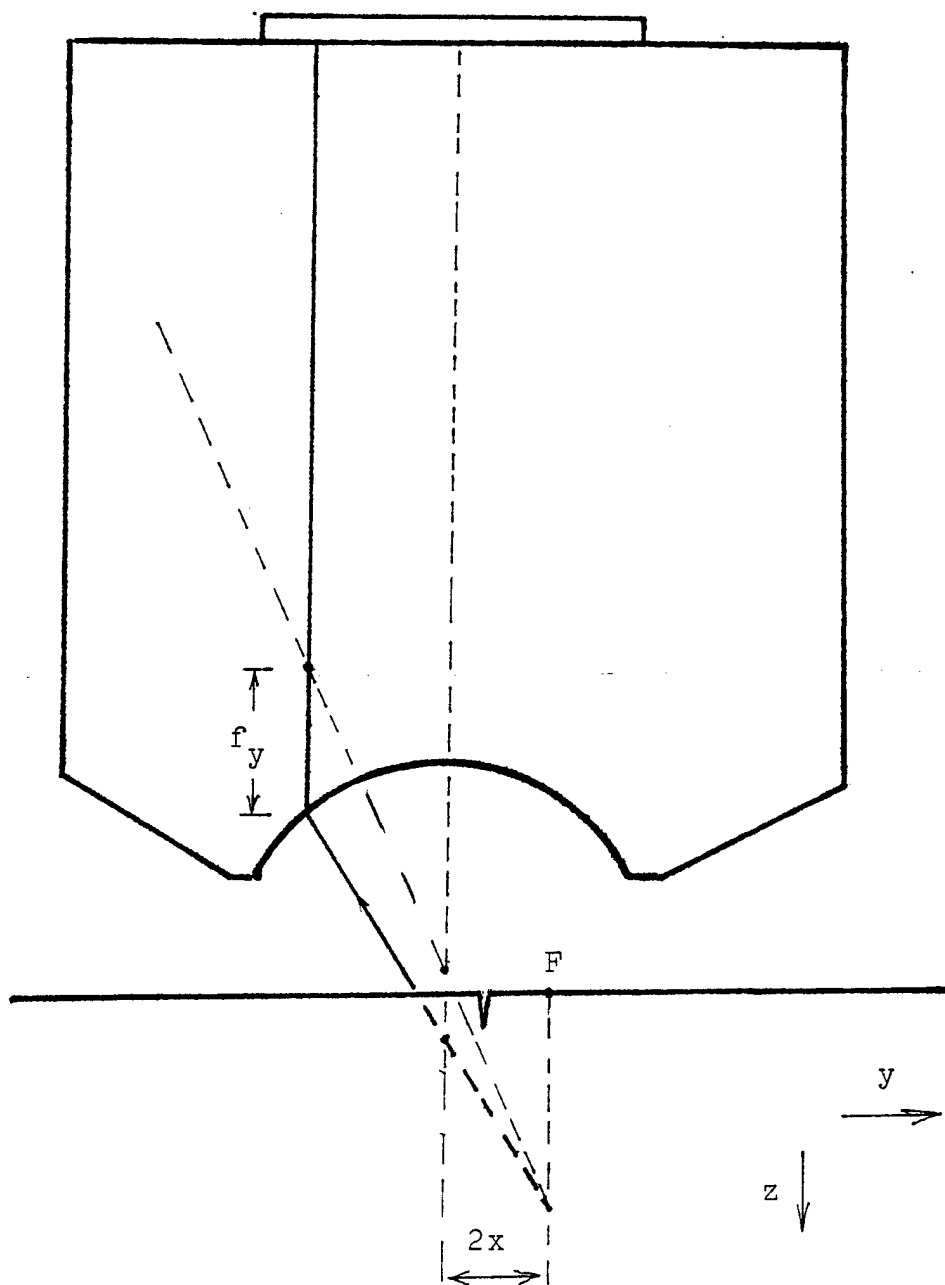


**Fig. 4.9** Focus formed in the lens rod by the rays re-radiated along the arc BAC in Fig. 4.8.

These factors may be approximated using  $f_x \ll D$  and  $f_x \approx f/n$  by

$$\sqrt{f_x / (D - f_x)} \approx \sqrt{f_x / D}$$

$$\sqrt{f_y / |D - f_y|} \approx \sqrt{f_c / n |D - f_y|}$$

Finally, the astigmatic beam illumination of the transducer has a phase curvature of

$$\exp \frac{ik_w (x - \rho_R)^2}{2nD} \cdot \exp \frac{ik_w y^2}{2n(D - f_y)}$$

Combining and simplifying algebraically all of the above factors gives the field illuminating the transducer as

$$\begin{aligned} & R_c T_{LW}(\rho_R) T_{WL}(\rho_R) E \exp 2i(k_w D/n + k_w f + z \sec \theta_R) \\ & \cdot \exp 2i k_p (x - z \tan \theta_R) \cdot \exp (-i 3\pi/2) \sqrt{\frac{f f_x}{n}} \\ & \cdot \frac{\rho_R}{D \sqrt{2 |x| c}} \sqrt{\frac{D}{D - f_y}} \cdot \exp \frac{ik_w (x_1 - \rho_R)^2}{2nD} \cdot \exp \frac{ik_w y_1^2}{2n(D - f_y)} \text{Gate}\left(\frac{y}{y_{\max}}\right), \end{aligned} \quad (4.3.5)$$

where the function

$$\begin{aligned} \text{Gate}(y) &= 1, & |y| < 1 \\ &= 0, & \text{otherwise.} \end{aligned}$$

takes into account the spatial bounds imposed on the beam by the lens aperture. Using the divergence of the beam to project the aperture onto the transducer plane (Fig. 4.10),  $y_{\max}$  is found to be

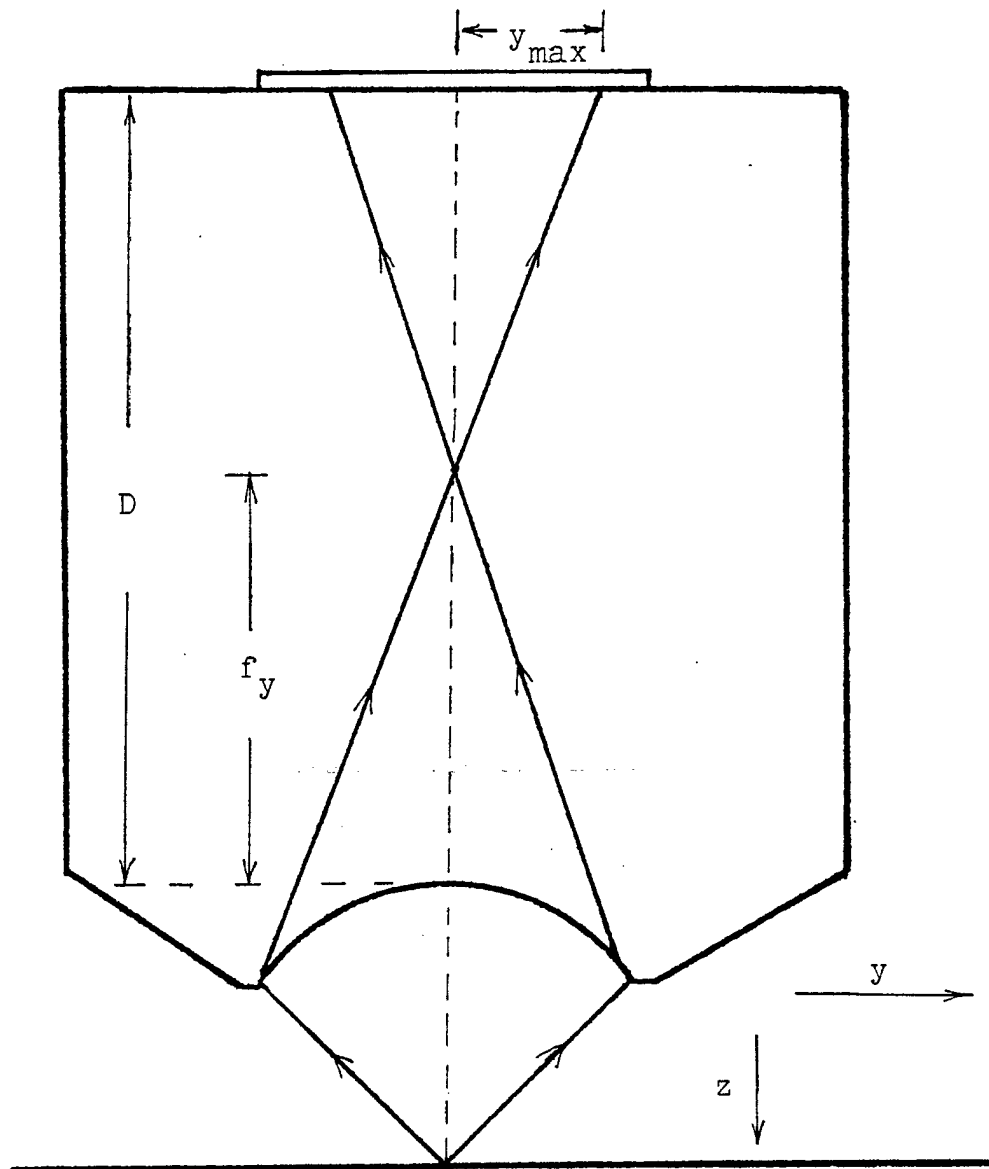


**Fig. 4.10** Illumination of the transducer by a bundle of leaky rays, shown in  $y$ - $z$  plane, reflected from the crack.

$$y_{\max} = R_a \frac{|D-f_y|}{|f_y|}. \quad (4.3.6)$$

The aperture radius  $R_a$  is equal to transducer radius  $R_T$  for the circular lens used in this study. It follows from (4.3.6) that  $y_{\max} > R_T$  and the transducer is fully illuminated for  $f_y < D/2$ . To find  $y_{\max}$  for the slot lens, the half-width  $w$  of the slot should be used in (4.3.6) instead of  $R_a$ . It then follows that in the case of the slot lens, the transducer is fully illuminated for  $f_y < D/(R_T/w + 1)$ .

Integrating the field (4.3.5) over the transducer and normalizing to the transducer area, the voltage response  $V_R$  is found to be

$$V_R(x) = R_c T_{LW}(\rho_R) T_{WL}(\rho_R) E \exp 2i(k_w D/n + k_w f + z \sec \theta_R) \cdot \exp 2i k_p(x - z \tan \theta_R) \cdot \exp(-i3\pi/2) \sqrt{\frac{f f_x}{n}} \cdot \frac{\rho_R}{D \sqrt{2|x|} c} \cdot K_1(x), \quad (4.3.7)$$

where

$$K_1(x) = \frac{1}{\pi R_T^2} \cdot \int_{\text{transducer}} \sqrt{\frac{D}{D-f_y}} \exp \frac{ik_w(x_1 - \rho_R)^2}{2nD} \cdot \exp \frac{ik_w y_1^2}{2n(D-f_y)} dx_1 dy_1 \quad (4.3.8)$$

The  $x$ -dependent factor in (4.3.7) is  $K_1(x) \exp(2ik_p x) / \sqrt{|x|}$ .

As  $K_1(x)$  is not a function of  $z$  it can be pre-calculated once and used for all  $z$  in obtaining numerical solutions. The amplitude and phase of  $K_1(x)$  were evaluated numerically and plotted in Figs. 4.11 and 4.12 for the case of a glass substrate and dimensions of the lens used in the measurements. Since both amplitude and phase of  $K_1$  are nearly constant except for small  $x$ , the value of  $K_1(x)$  at any  $x$  sufficiently far from the origin can be evaluated just once for a particular lens and used for all large values of

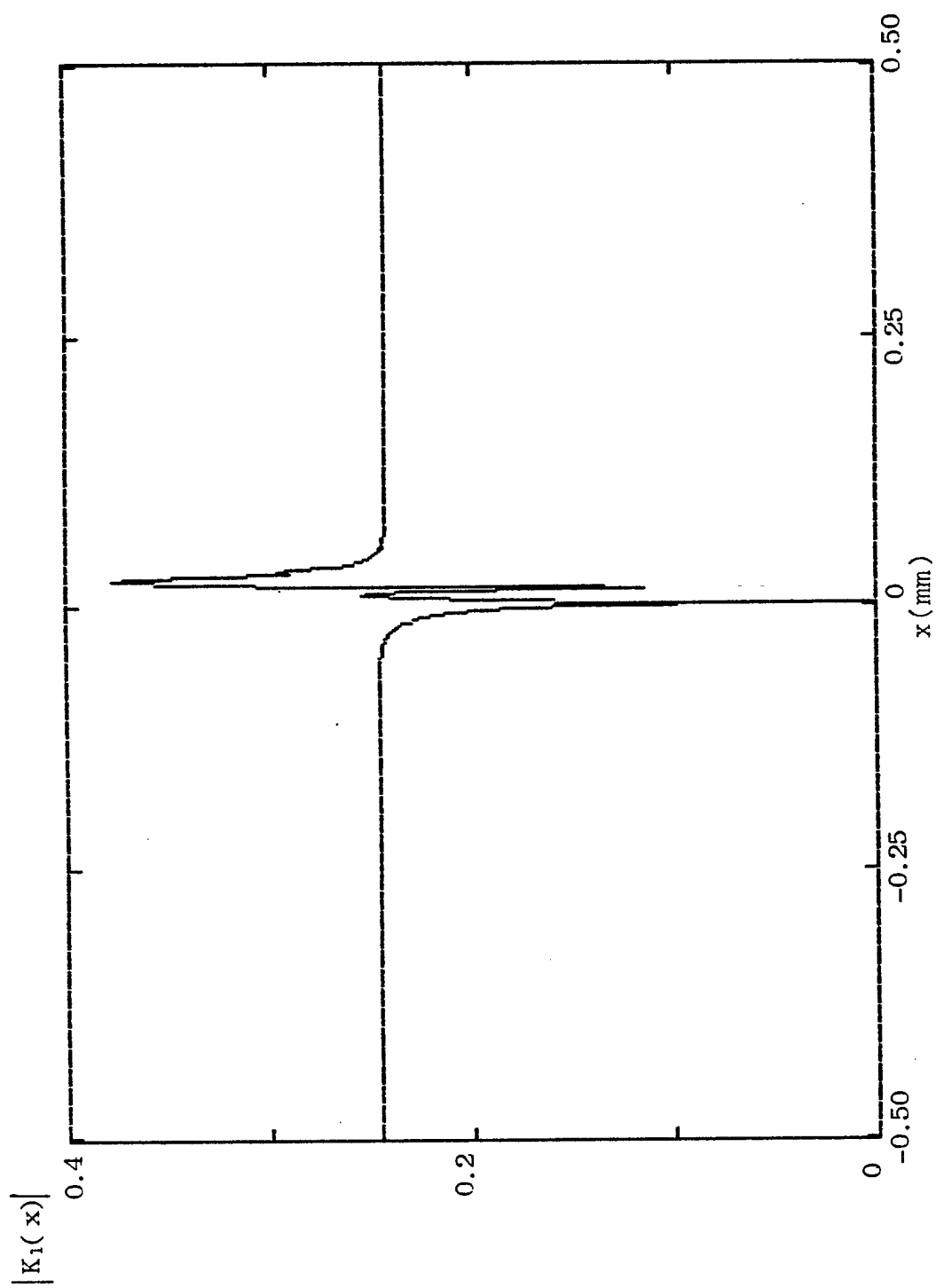


Fig. 4.11a Amplitude of  $K_1(x)$  calculated for a circular lens.

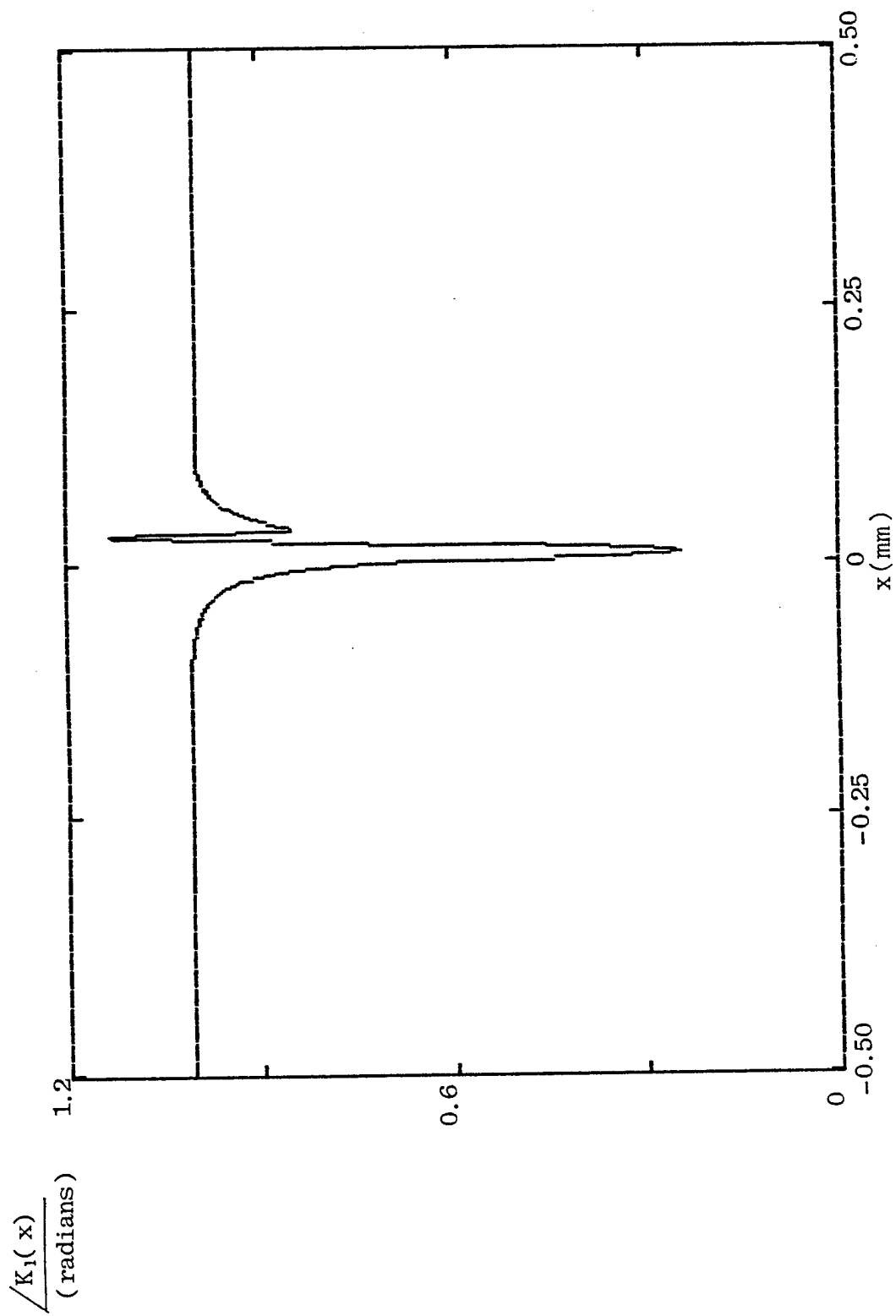


Fig. 4.11b Phase of  $K_1(x)$  calculated for a circular lens.

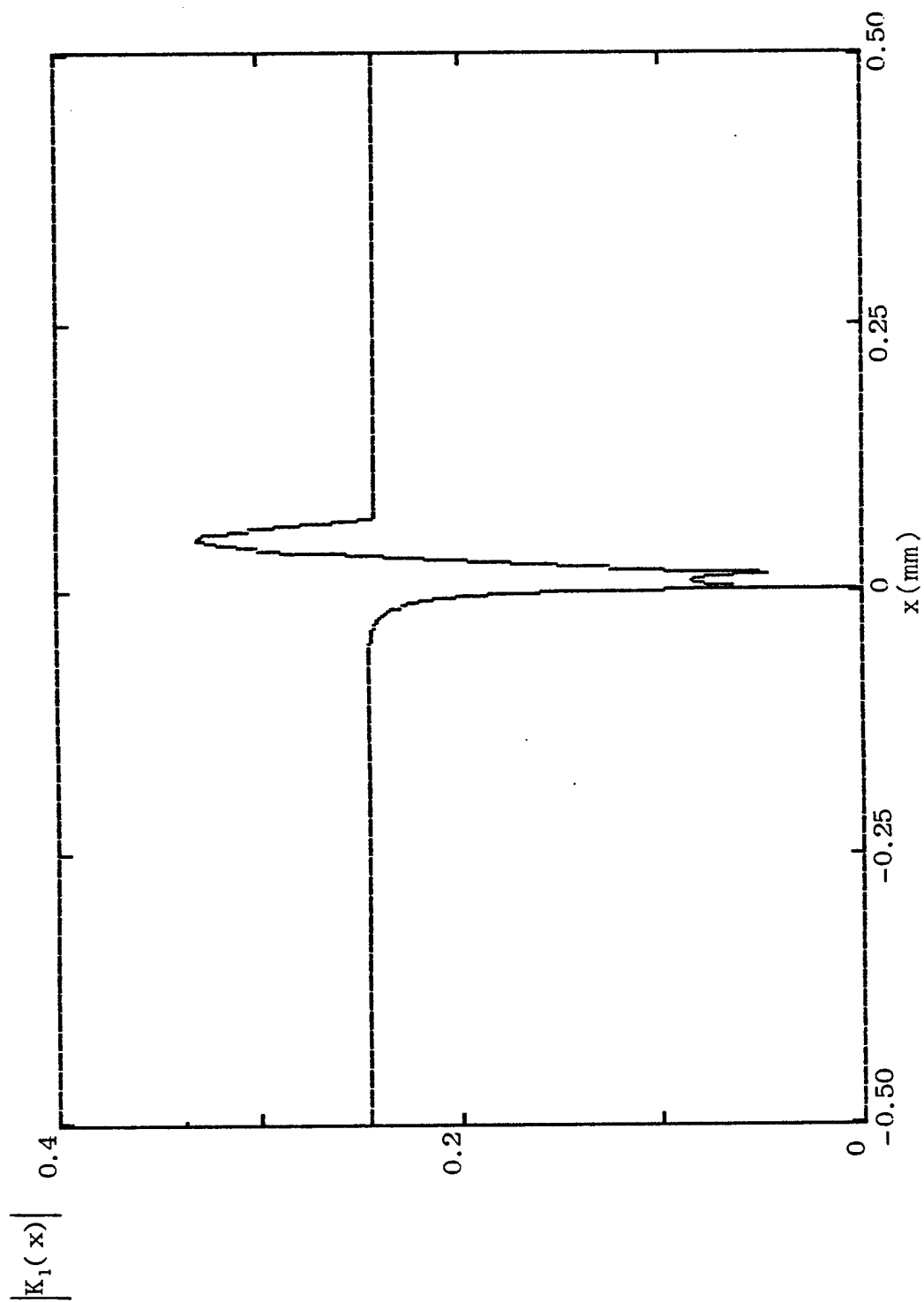


Fig. 4.12a Amplitude of  $K_1(x)$  calculated for a slot lens.

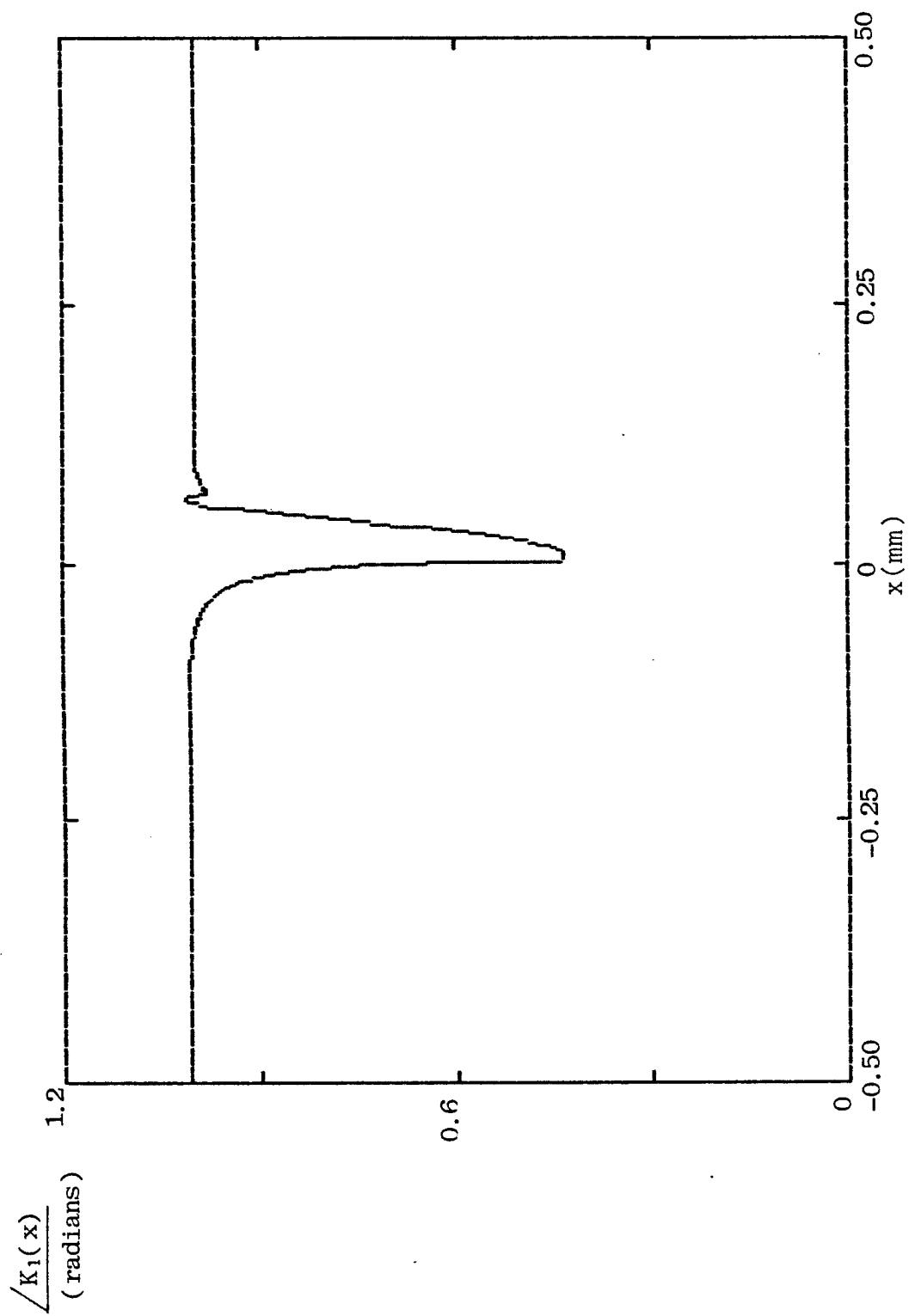


Fig. 4.12b Phase of  $K_1(x)$  calculated for a slot lens.



x. It follows that  $V(x)$  varies as  $\exp(2ik_p x) / \sqrt{|x|}$  for large  $x$ .

At  $f_y = D$ , which corresponds to

$$x = \frac{(f - R) \rho_R}{2(D - f_x)}, \quad (4.3.9)$$

the focal point lies in the plane of the transducer, resulting in rapid phase variations of the integrand in (4.3.8). At this singular point geometric ray approximations fail and diffraction effects must be considered. However, as is evident from (4.3.4),  $f_y$  is a rapidly varying function of  $x$  (for small  $x$ ) and, thus, the approximations quickly become reasonable only a small distance from this critical point.

#### The reflected contribution $V_{\text{refl}}(x, z)$ for $z < 0$

The entire reflected voltage contribution  $V_{\text{refl}}(x, z)$  will now be considered when the crack lies within the Rayleigh circle, i.e.  $z < 0$  and  $x < c$ , shown in Fig. 4.7a. The rays incident from the left give exactly the same expression as found for  $V_R(x)$  except that for  $f_y > D$  there is only one astigmatic focus in the lens rod, which corresponds to  $0 < x < 2(D - f_x) / (f - R) \rho_R$ . In this case the ray field does not suffer a  $-\pi/2$  phase shift due to passing through the focus in the corresponding range of  $x$ , or explicitly

$$\begin{aligned} V_{\text{RL}}(x) &= V_R(x) \exp(i\pi/2), & 0 < x < 2(D - f_x) / [(f - R) \rho_R] \\ V_{\text{RL}}(x) &= V_R(x), & \text{otherwise.} \end{aligned} \quad (4.3.10)$$

To find the contribution due to rays incident on the right,  $-x$  should replace  $x$  in the expression (4.3.7). As shown in Fig. 4.7b, the Rayleigh waves are reflected from the crack before reaching the focus at the lens axis. The reflected rays will still converge to a focus located a distance  $2x$  from the lens axis. If  $2x > c$ , the rays will leak into water

and focus above the sample surface. In either case, a real focus is formed and the previous expression derived for  $V_R(x,z)$  applies. It should also be noted that since  $f_y < 0$  for  $|x|$  small and  $x < 0$ , there is only one real focus in the lens rod and therefore:

$$V_{RR}(x,z) = V_R(-x,z) \exp(i\pi/2). \quad (4.3.11)$$

As  $|x|$  increases,  $f_y$  for  $V_{RR}(x,z)$  determination will eventually become positive, however, in this case the crack will be outside the Rayleigh circle for practical defocus distances  $z$  and moreover  $V_{RR}(x,z) = 0$  for  $|x| > c$ .

**The reflected contribution  $V_{\text{refl}}(x,z)$  for  $z > 0$**

It can be seen from Fig. 4.13 that

$$\begin{aligned} V_{RR}(x,z) &= 0, \quad \text{for } z > 0, x > 0 \\ V_{RL}(x,z) &= 0 \quad \text{for } z > 0, |x| < c. \end{aligned} \quad (4.3.12)$$

For  $z > 0$  and  $x > c$ , the diverging beam incident on the sample surface has passed through the spherical lens focus and has therefore suffered a phase shift of  $-\pi$ . However, there is no real Rayleigh wave focus on the sample surface in this case since the incident beam is diverging when it strikes the sample surface and the phase shift of  $-\pi/2$  included in derivation of  $V_R(x,z)$  no longer applies. Thus, for  $z > 0$

$$\begin{aligned} V_{\text{refl}}(x,z) &= V_L(x,z) = V_R(x,z) \exp(-i\pi/2), & x > c \\ &= 0, & x < c. \end{aligned} \quad (4.3.13)$$

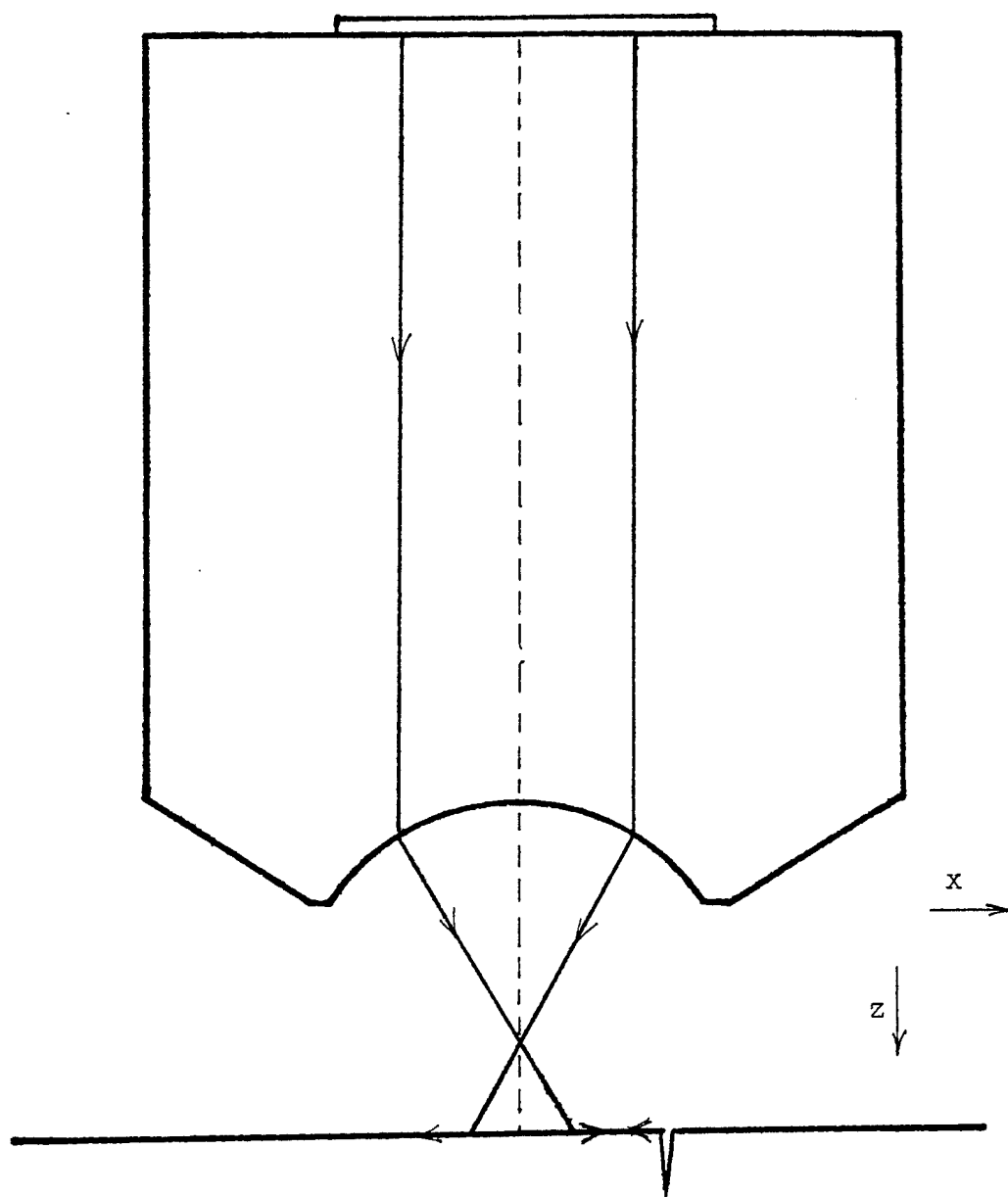


Fig. 4.13 Surface wave interaction with a crack for  $z > 0$ .

#### 4.4 The total voltage response $V(x,z)$

The total transducer voltage response function  $V(x,z)$  is found by adding the specularly reflected, transmitted and crack-scattered contributions as per expression (4.1). Typical  $V(x,z)$ , calculated for circular and slot lenses for defocus distance  $z = -400$   $\mu\text{m}$  and crack-lens displacement  $0 < x < 500$   $\mu\text{m}$ , are plotted in Figs. 4.14 and 4.15, respectively.

As mentioned earlier, it is assumed here that the surface wave reflection and transmission coefficients of the crack,  $R_c$  and  $T_c$ , respectively, are constant for all angles of incidence. It is therefore necessary to use proper effective values for  $R_c$  and  $T_c$ . Angel and Achenbach [3] have carried out the analysis to find the scattering coefficients for various angles of incidence and crack depths. Some of their results are plotted in Fig. 4.16. The crack used in this work was very deep and, thus, the crack depth was assumed to be infinite. Since the circular lens excites surface waves that strike the crack over a large range of incident angles, it was decided to use  $R_c = 1$  and  $T_c = 0$  as the effective values in the calculations for this lens. This assumption is most valid for small  $x$ . As  $x$  increases, the rays incident at oblique angles that have a large  $R_c$  miss the transducer so only rays that are nearly normal with lower effective  $R_c$  and larger effective  $T_c$  are detected.

The surface waves launched by the slot lens propagate in a narrower range of directions where the largest angle of incidence on the crack is given by  $\tan^{-1}(w/\rho_R)$ . For the lens used here, the above angle is  $22^\circ$ . The effective values for the slot lens are therefore chosen as  $R_c = .54$  and  $T_c = 0$ , which are strictly valid only for normally incident surface waves.

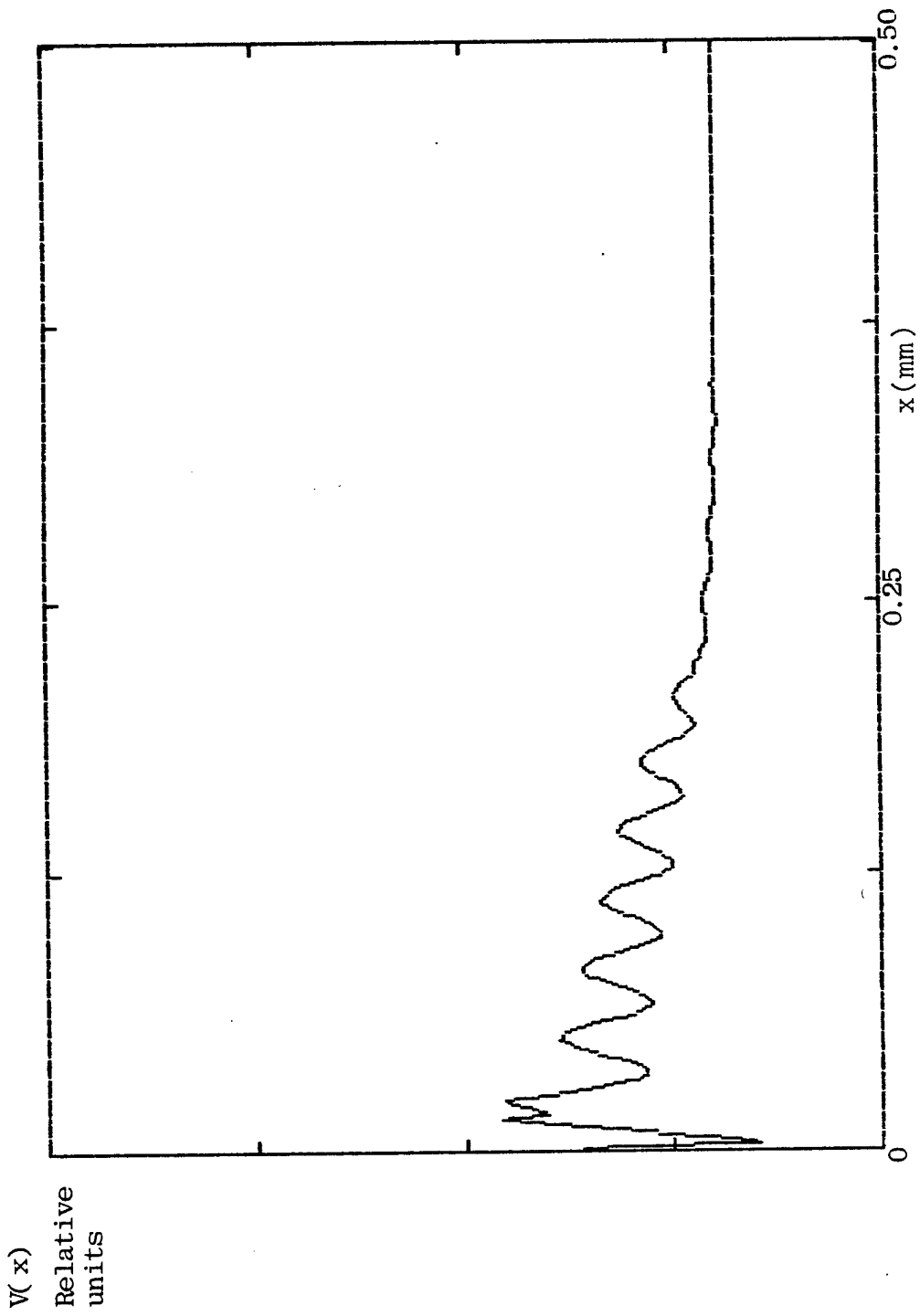


**Fig. 4.14**  $V(x, z = -400 \mu\text{m})$  calculated for a circular lens.

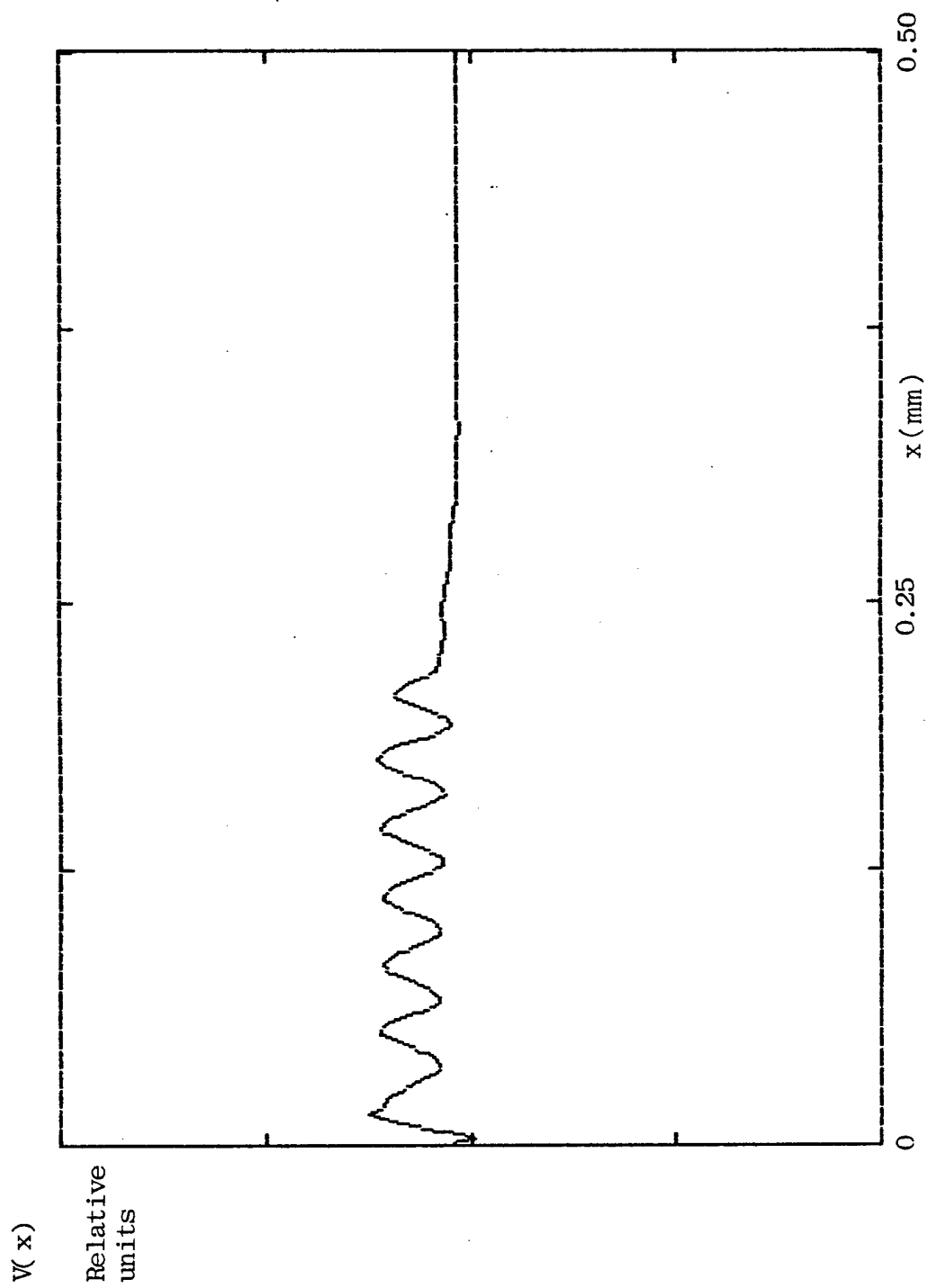


**Fig. 4.15**  $V(x, z = -400 \text{ } \mu\text{m})$  calculated for a slot lens.

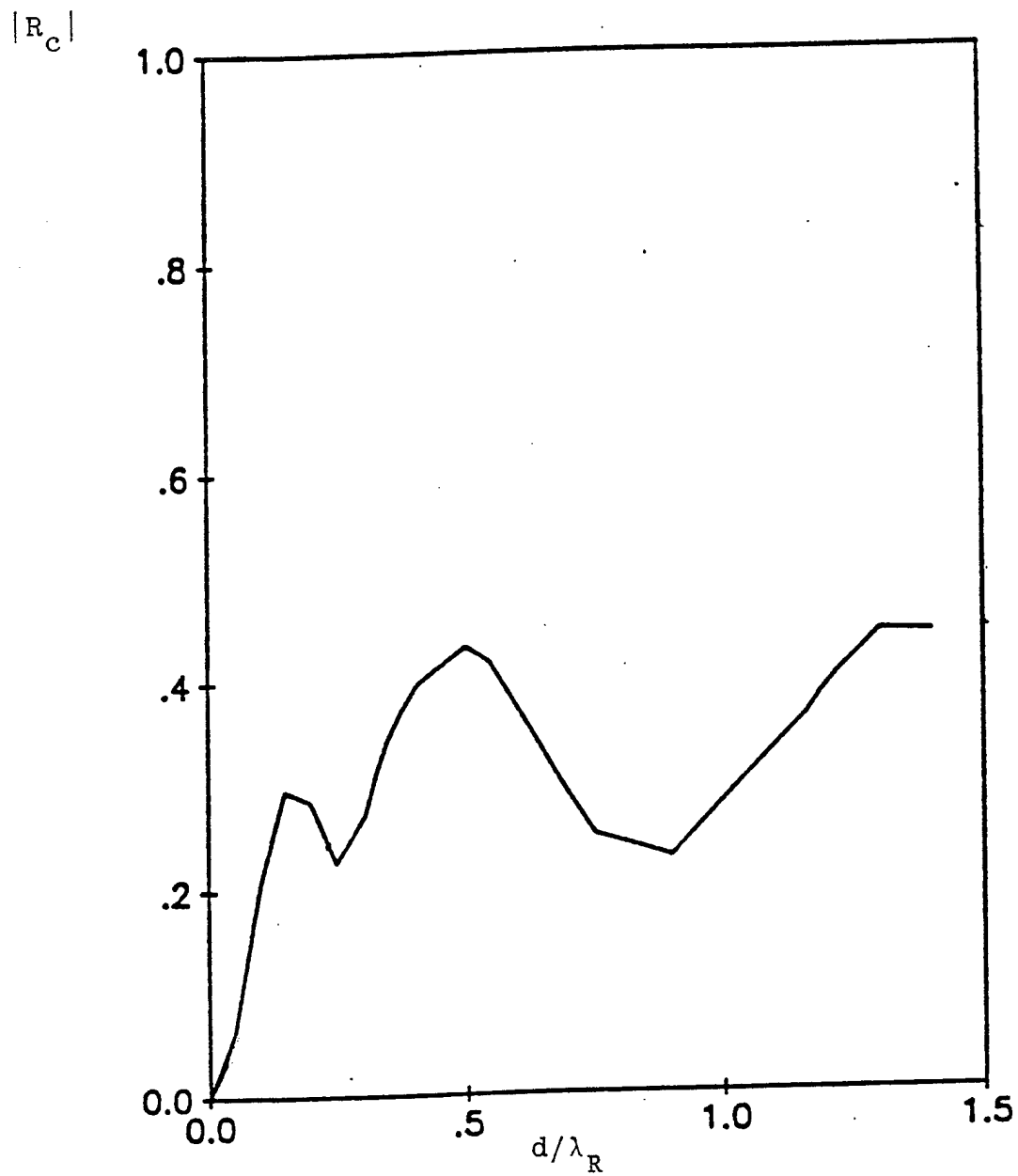


**Fig. 4.16** Variation of amplitude of the crack reflection coefficient  $R_c$  with crack depth  $d$  normalized to the Rayleigh wavelength  $\lambda_R$  for normally incident surface waves ( from Angel and Achenbach [3]).

## Chapter V

### Experimental measurement of $V(x)$

In this chapter a comparison will be made between experimentally measured  $V(x)$  and  $V(x)$  calculated using the ray theory discussed in Chapter IV. An algorithm for extracting the reflection coefficient of the crack from the observed  $V(x)$  data will be presented and used to determine the  $R_c$  value for a cracked glass sample.

#### 5.1 Experimental measurement of $V(x)$

To obtain a suitable sample, 1 mm Corning glass microscope slides were stressed with a pointed object to introduce a linear localized defect. The sample was then heated on a hot plate which caused the crack to propagate a distance through the sample. Only samples with straight cracks that were normal to the surface and contained internally to the sample dimensions were chosen for measurement.

The  $V(x)$  curves for the circular and slot lenses, calculated for various defocus distances  $z$ , and for the range  $0 < x < 500 \mu\text{m}$  are displayed along with measured  $V(x)$  curves in Figs. 5.1 - 5.2 and 5.3 - 5.4, correspondingly.

The theoretical model in Chapter IV predicts that for  $x$  near the origin, or, equivalently, lens approximately centered above the crack, there is one cylindrical (line) focus in the lens rod located a distance  $f_x$  above the lens surface. Actually, as shown in Fig. 5.5, the crack acts as a plane mirror, and the rays trace symmetrically the same paths as they do in the defect-free case; however, source and radiation points now lie on the same side of the transducer. This results in a ring (and not a line) focus, as mentioned in Chapter II review of the geometric ray method. Thus some disagreement between theory and experiment may be expected for small  $x$  in the case of a circular lens. The leaky rays entering the slot lens from defect-free sample form short arc foci in the lens



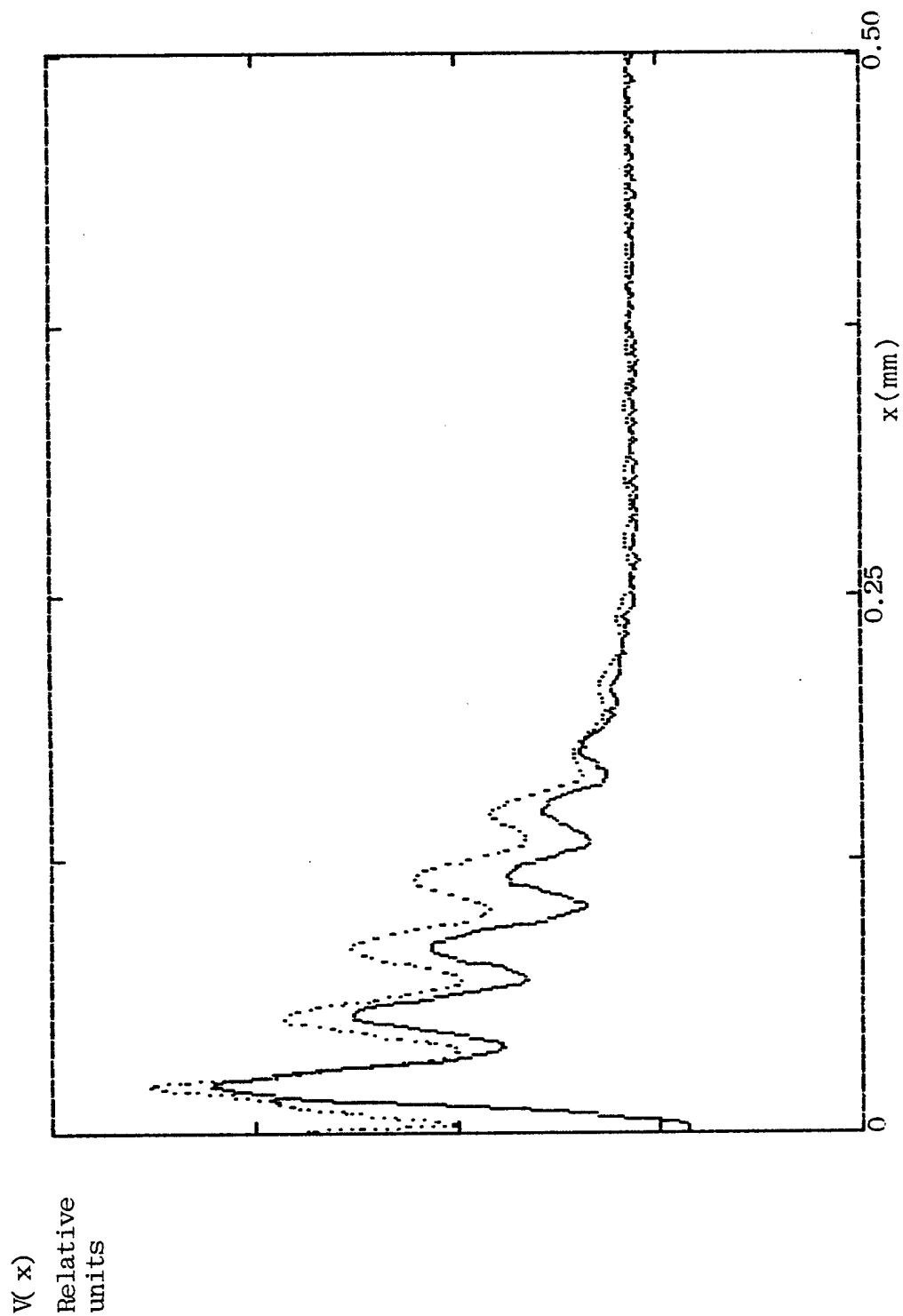


**Fig. 5.1**  $V(x, z = -300 \mu\text{m})$  for a circular aperture lens : observed (solid) and calculated (dotted) (scaled to match at  $x = -500 \mu\text{m}$ ).

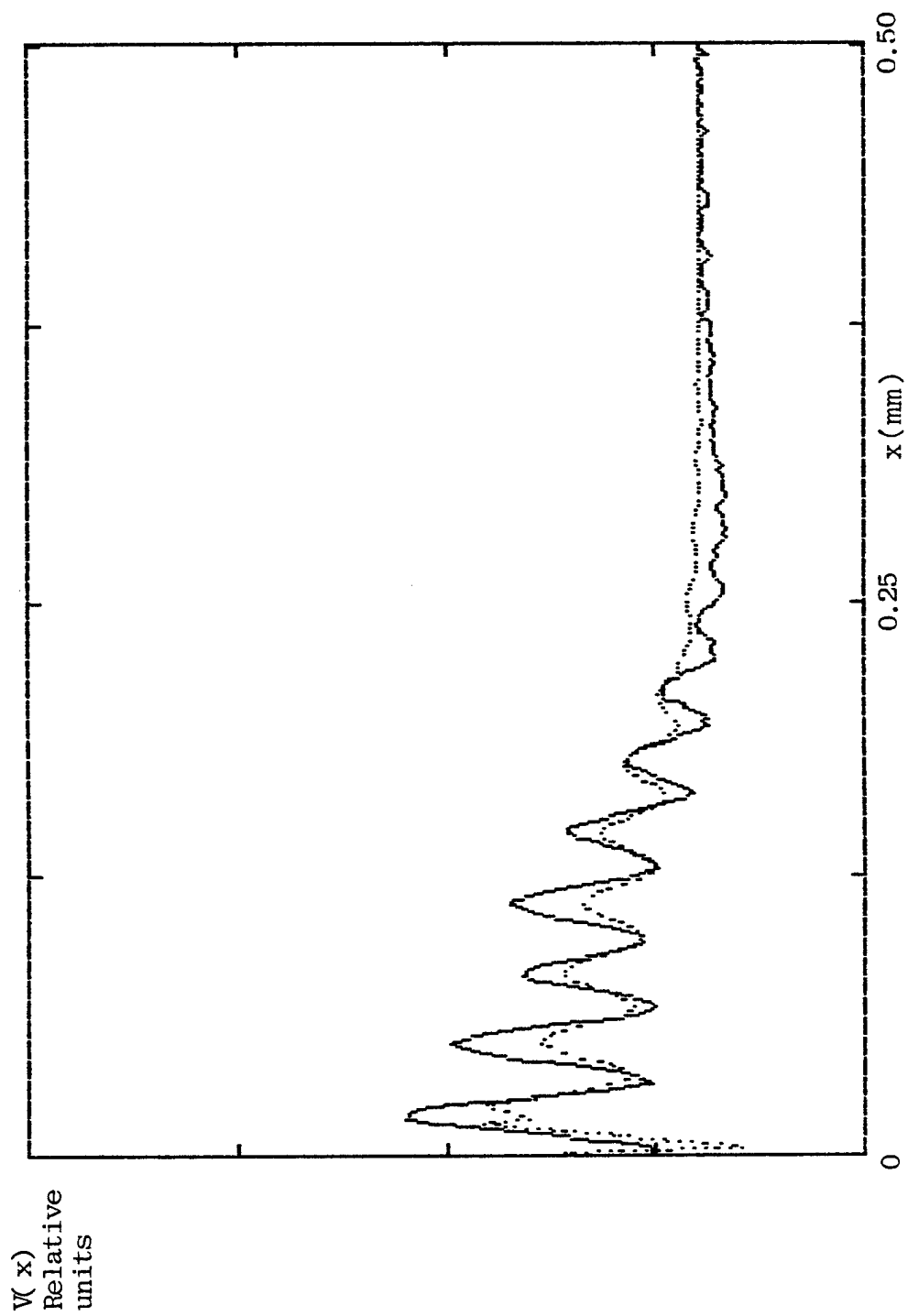


**Fig. 5.2**  $V(x, z = -400 \text{ } \mu\text{m})$  for a circular aperture lens : observed (solid) and calculated (dotted).

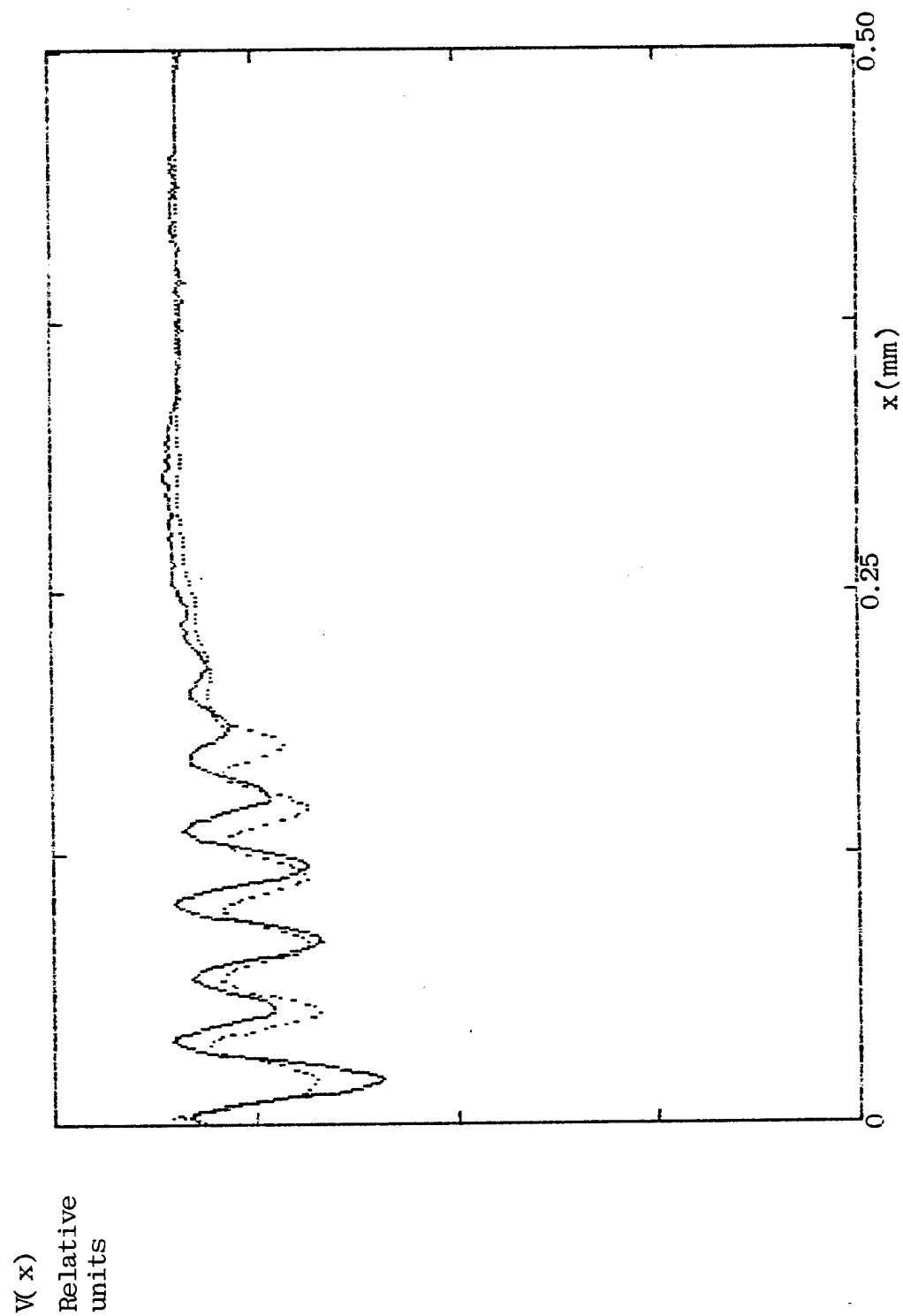


**Fig. 5.3**  $V(x, z = -346 \mu\text{m})$  for a slot aperture lens : observed (solid) and calculated (dotted).

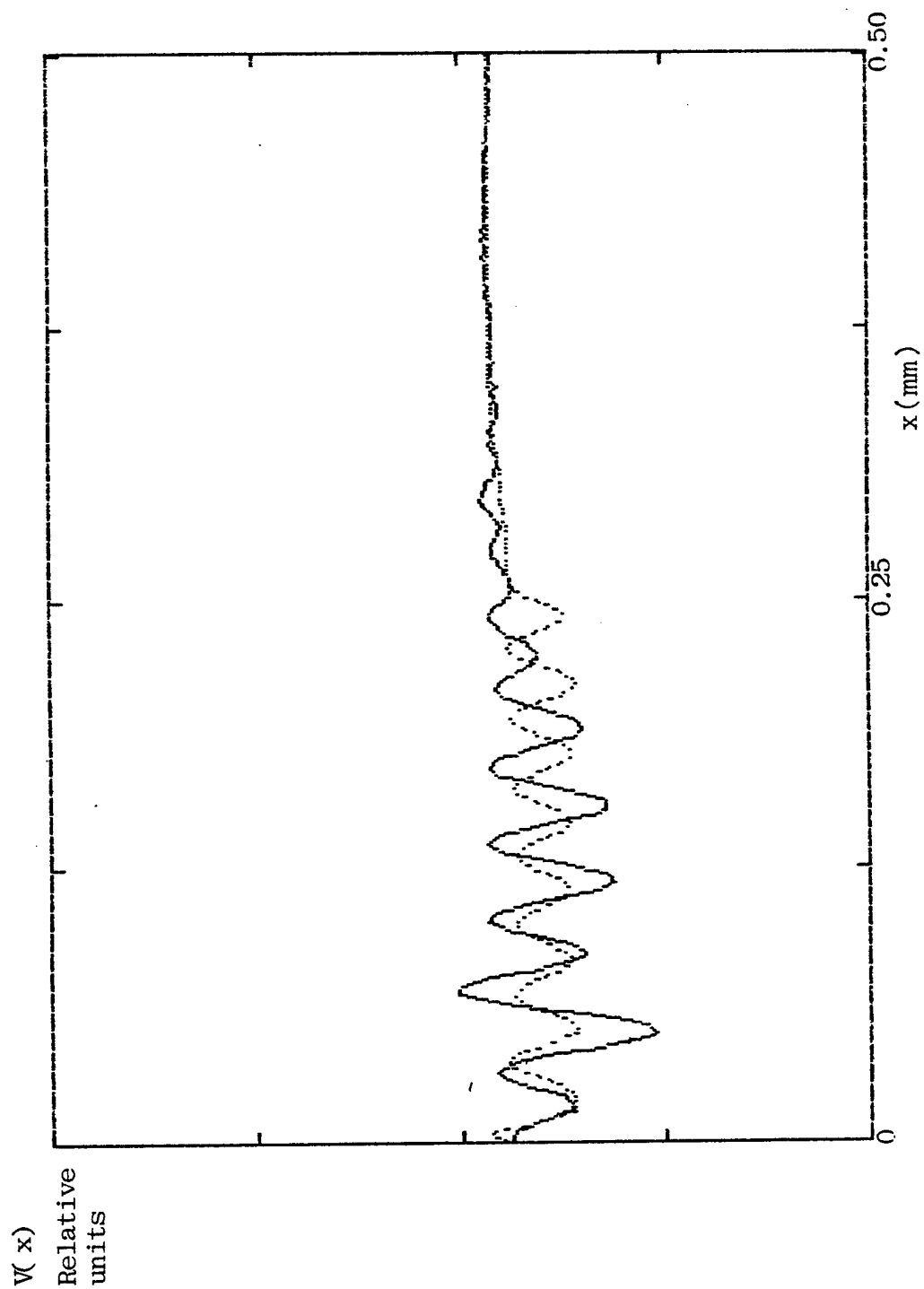


**Fig. 5.4**  $V(x, z = -474 \mu\text{m})$  for a slot aperture lens : observed (solid) and calculated (dotted).

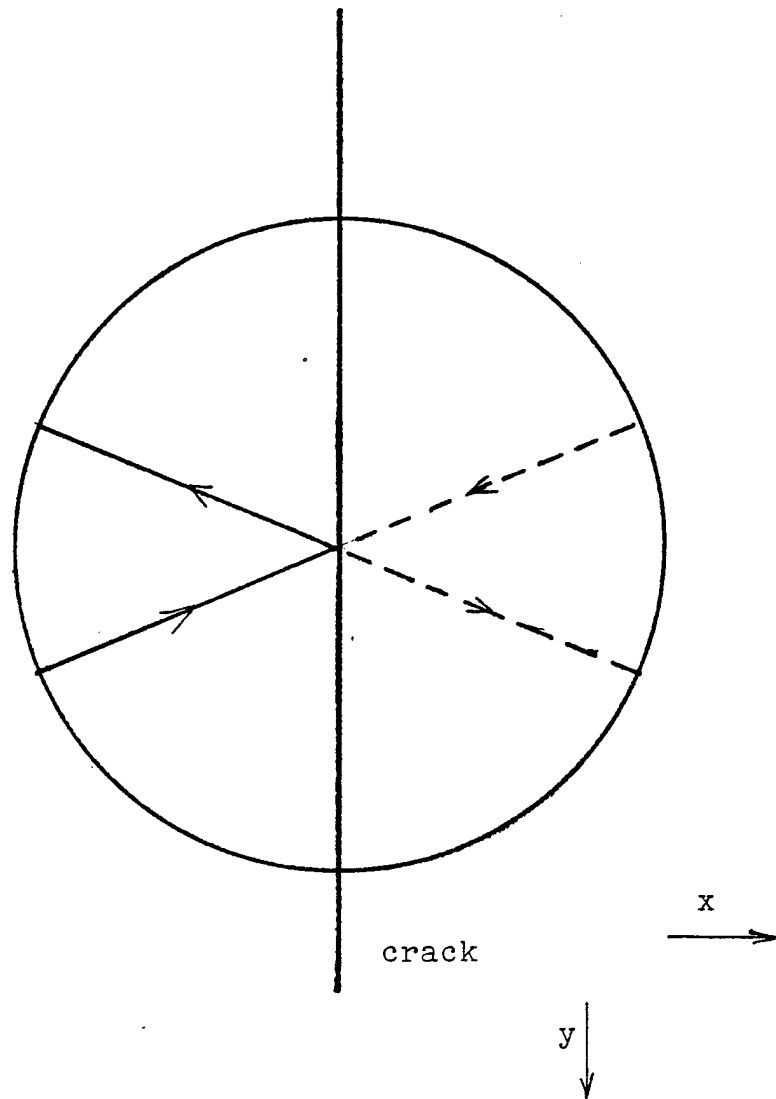


**Fig. 5.5** Selected surface wave paths on the sample surface at  $z < 0$  containing a crack parallel to the  $y$ -axis at  $x = 0$ .

rod; this error is not expected to be as significant as in the case of the circular lens since for a narrow slot these arcs are short and hence close in shape to line foci.

When the crack is near the edge of the Rayleigh circle, i.e.  $x \approx c = |z| \tan \theta_R$ , Rayleigh waves are excited, scattered from the crack, and re-radiated within a small distance and therefore the expression (4.3.2) for coefficient E is no longer correct, as mentioned in Chapter IV. Also, some disagreement is expected due to the fact that the variation in the  $R_c$  and  $T_c$  with the angle of incidence was ignored.

## 5.2 Extracting the surface wave reflection coefficient of a crack from

### $V(x)$ measured using a slot lens

As mentioned above, when the lens is negatively defocused and the crack lies at the lens axis, i.e.  $x = 0$ ,  $z < 0$ , the leaky rays trace paths that are mirror images of leaky wave paths for the defect-free case. Therefore, the microscope response at that point may be represented in terms of unperturbed contributions  $V_G$  and  $V_L$  as

$$V(x=0, z) = V_G(z) + T_c \cdot V_L(z) + R_c \cdot \left( \frac{V_L(z)}{2} + \frac{V_L(z)}{2} \right), \quad (5.2.1)$$

where the reflected contribution has been separated into two identical terms due to surface waves incident on the crack from the right and from the left. Note when the discontinuity is not present,  $T_c = 1$  and  $R_c = 0$ , and (5.2.1) reduces to the usual form  $V(z) = V_G(z) + V_L(z)$ . At this point  $f_y$  tends to infinity (4.3.4), and there is only one focus in the lens rod, located at  $f_x$  above the aperture.

When the lens is moved from the crack in the positive  $x$  direction ( see Fig. 4.7), the surface waves incident from the left have to propagate an additional distance of  $2x$  to the crack and back, thus gaining  $i2k_R x$  in phase. Similarly, the rays incident from the

right encounter the crack sooner and thereby lose  $i2k_R x$  in phase. Neglecting other variations, which will be considered later, expression (5.2.1) can therefore be generalized for  $x > 0$  as

$$\begin{aligned} V(x, z) &= V_G(z) + T_c \cdot V_L(z) + R_c \cdot \frac{V_L(z) \exp(i2k_R x) + V_L(z) \exp(-i2k_R x)}{2} \\ &= V_G(z) + T_c \cdot V_L(z) + R_c \cdot V_L(z) \cos 2k_R x. \end{aligned} \quad (5.2.2)$$

The expression (5.2.2) can be used as a basis for the extraction of  $R_c$  from  $V(x)$  data but first the region of its validity should be determined. Since  $f_y$  varies as  $1/x$  for small  $x$ , it rapidly approaches the plane of the transducer as  $x$  increases from 0. A critical point is encountered when this focal point crosses the transducer plane, which occurs at  $x$  given by (4.3.9). Evaluating (4.3.9) for the lens used in this work gives the location of the critical point as  $x = 15 \mu\text{m}$ . The amplitude of  $V(x)$  calculated for  $z = -346 \mu\text{m}$  is plotted in Fig. 5.7. It can be observed from the graph that for  $0 < x < 10 \mu\text{m}$  the  $V(x)$  varies as a cosine function, in agreement with (5.2.2). As discussed above, the model for  $V(x)$  described in Chapter IV fails at  $x = 0$ . At that point, however, the microscope response is reasonably well described by (5.2.1). Thus, the expression (5.2.2) will be assumed to be valid for small  $x$  and, therefore, be used for extracting a value for  $R_c$ .

The acoustic microscope employed in this work measures only the amplitude of the transducer voltage  $|V(x, z)|$ . Taking the amplitude of (5.2.2) and squaring it for convenience gives

$$\begin{aligned} |V(x, z)|^2 &= |V_G + T_c \cdot V_L|^2 + 2 |V_G + T_c \cdot V_L| \cdot |V_L R_c| \cdot \cos(2k_R x + \phi(z)) + \\ &\quad + |V_L R_c|^2 \cos^2 2k_R x. \end{aligned} \quad (5.2.3)$$

where  $\phi(z) = \arg(V_G(z)) - \arg(V_L(z)) - \arg(R_c)$ . Since the measurement is carried out on

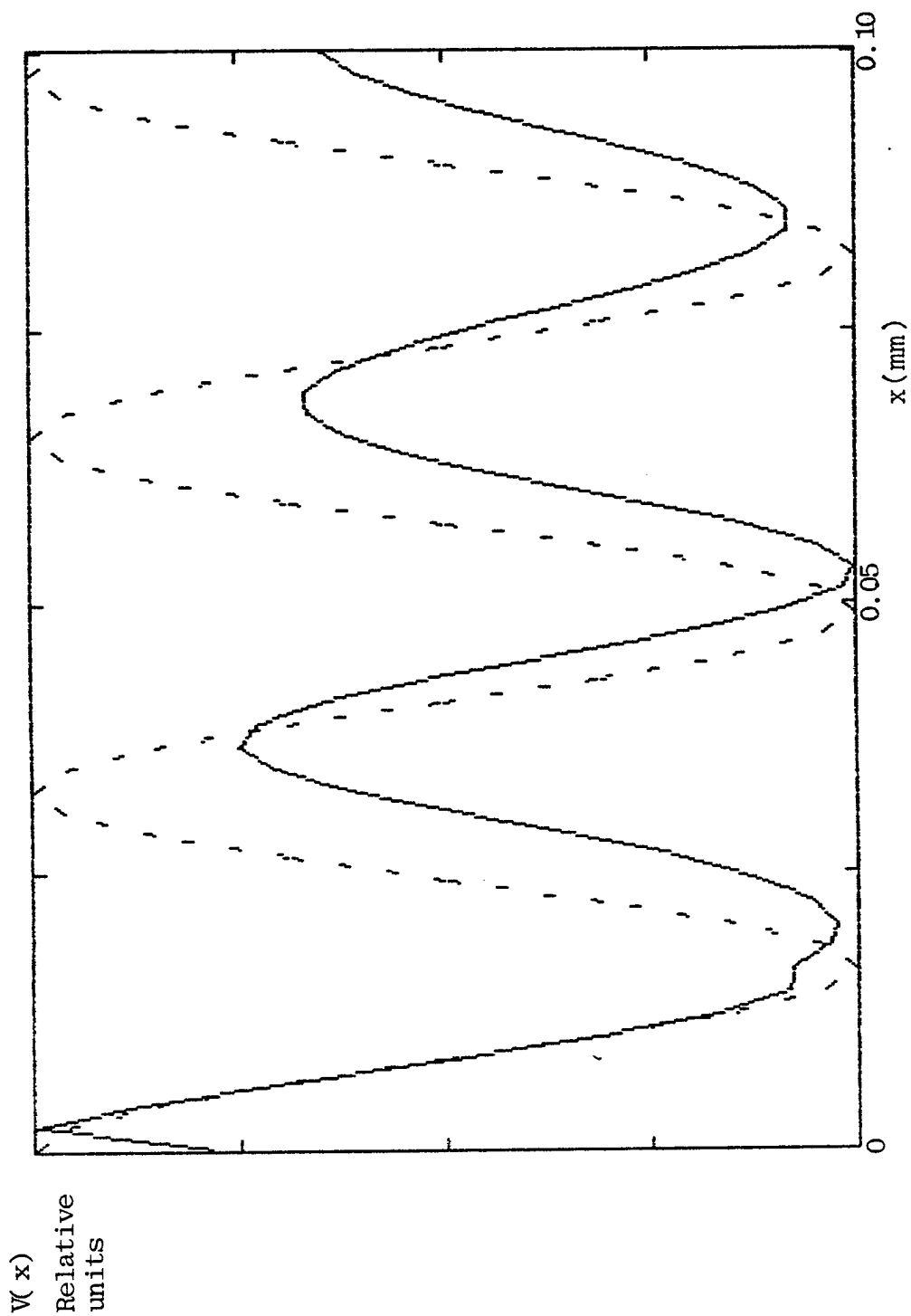


**Fig. 5.6** (a) Calculated  $V(x, z = -346 \text{ } \mu\text{m})$  for a slot aperture lens (solid) and  
(b)  $\cos(2k_R x)$  function (dashed).



a system where the smallest translational step is  $2 \mu\text{m}$ , there is a positional uncertainty of under  $1 \mu\text{m}$  in locating the true  $x = 0$  point. The resultant error in  $x$  can be included as a constant phase term in  $\phi$  in (5.2.3).

When the  $V(x)$  measurement is performed at  $z$  corresponding to a  $V(z)$  maximum or minimum, the  $V_G$  and  $V_L$  are exactly in phase or  $180^\circ$  out of phase, respectively, ( $V(z) = |V_G| \pm |V_L|$ ) and the magnitude of  $|V_L|$  can be deduced by subtracting  $|V_G|$  from  $V(z)$ . To find  $|V_G|$ , the  $V(z)$  of teflon is scaled to match the  $V(z)$  of glass at large  $z$ , where  $|V_L| \ll |V_G|$ .

The last term in (5.2.3) can be expanded as :

$$|V_L R_c|^2 \cos^2 2k_R x = \frac{|V_L R_c|^2}{2} (1 + \cos 4 k_R x) . \quad (5.2.4)$$

Evaluating the  $|V_L|$  and  $|V_G|$  at several local  $V(z)$  maxima and minima gives  $|V_G| > 10 |V_L|$  in which case the term (5.2.4) is small compared to the other terms in (5.2.3) and can be neglected. To remove the  $x$ -independent term  $|V_G + T_c V_L|^2$  from (5.2.3),  $|V(0, z)|^2 - |V(x, z)|^2$  is evaluated as

$$\begin{aligned} |V(0, z)|^2 - |V(x, z)|^2 &= 2 |(V_G + T_c V_L) V_L R_c| \cos \phi (1 - \cos 2k_R x) \\ &\quad - 2 |(V_G + T_c V_L) V_L R_c| \sin \phi \sin 2k_R x . \end{aligned} \quad (5.2.5)$$

The objective here is to find the coefficients multiplying the  $(1 - \cos 2k_R x)$  and  $\sin 2k_R x$  terms. When (5.2.5) is evaluated at two points  $x_1$  and  $x_2$ , a system of two equations and containing the two undetermined coefficients  $A$  and  $B$  results that satisfy

$$\begin{aligned} A(1 - \cos 2k_R x_1) - B \sin 2k_R x_1 &= |V(0, z)|^2 - |V(x_1, z)|^2 \quad \text{and} \\ A(1 - \cos 2k_R x_2) - B \sin 2k_R x_2 &= |V(0, z)|^2 - |V(x_2, z)|^2 . \end{aligned} \quad (5.2.6)$$

where A and B are independent of x and given by

$$\begin{aligned} A &= 2 |(V_G + T_c V_L) V_L R_c| \cos \phi \quad \text{and} \\ B &= 2 |(V_G + T_c V_L) V_L R_c| \sin \phi. \end{aligned} \quad (5.2.7).$$

The system (5.2.6) can be solved for A and B from the measured data. From (5.2.7) it follows that

$$\sqrt{A^2 + B^2} = 2 |(V_G + T_c V_L) V_L R_c|$$

and

$$\phi = \tan^{-1} B/A. \quad (5.2.8)$$

The factor  $|(V_G + T_c V_L)|$  in (5.2.7) is found by noting that it is exactly the square root of the x-independent term in (5.2.3) and can therefore be obtained by substituting (5.2.7) and (5.2.8) into (5.2.3) for any small x. Finally,  $|R_c|$  is found from (5.2.8) using the value of  $|V_L|$  deduced from the unperturbed  $V(z)$ 's of glass and teflon, in the procedure described above.

Since the system of equations (5.2.6) requires the knowledge of  $V(x,z)$  at only two x locations beside the value  $V(0,z)$ , it is possible to use the  $V(x,z)$  data at other points to create additional (redundant) equations and simultaneously solve any two of them. The resulting values of  $|R_c|$  can then be checked for consistency and if in reasonable agreement can then be averaged.

The results of applying this algorithm to extract  $|R_c|$  from  $V(x)$  measured at different defocus distances z are presented in Table I. Since the signal detected by the transducer weakens significantly as  $|z|$  increases, only  $V(x,z)$  measured at small  $|z|$  are deemed reliable, i.e., least corrupted by noise. It is seen that the values of  $|R_c|$  in Table I

for  $z > -210 \mu\text{m}$  compare favorably with the value  $|R_c| = 0.54$  deduced by Achenbach, et. al. [14] for a deep crack. Furthermore, the average value of  $|R_c|$ , calculated for all  $z$  in Table I, is found to be 0.55.

Angel and Achenbach [3] have also produced a study of the dependence of  $|R_c|$  on the crack depth, reproduced in Fig. 4.16. Such a correlation could be used to determine the crack depth once  $|R_c|$  is found. Thus, the  $V(x,z)$  can be used as an important tool in defect characterization.

$z(\mu\text{m})$	Averaged $ R_c $
-72	0.50
-130	0.53
-208	0.56
-346	0.60
-416	0.75
-474	0.34
-534	0.66
-604	0.48

**Table I.** Values of crack reflection coefficient  $|R_c|$  deduced from  $V(x)$  measured at various defocus distances  $z$ .

## Appendix A

Derivation of geometric quantities  $\rho_R$ ,  $f_x$ ,  $f_y$ ,  $\rho_{Rmin}$ ,  $\rho_{Rmax}$ ,  $c_{min}$  and  $c_{max}$ .

### A.1 Derivation of $\rho_R$

The leaky ray that appears to originate from the lens focal point crosses the lens surface at a distance  $\rho = \rho_R$  from the lens axis. It follows from Fig. A.1 that:

$$\rho_R = f - (R - \sqrt{R^2 - \rho_R^2}) \tan \theta_R . \quad (A.1)$$

Solving for  $\rho_R$  gives:

$$\rho_R = (f - R) \sin \theta_R \cos \theta_R + \sin \theta_R \sqrt{(f - r)^2 \cos^2 \theta_R - (f^2 - 2Rf)} . \quad (A.2)$$

Substituting  $\theta_R = 28^\circ$  (glass),  $R = 3$  mm and  $f = 4$ mm into (A.2) gives

$$\rho_R = 1.8 \text{ mm}.$$

### A.2 Derivation of $f_x$

The leaky rays strike the lens as parallel family of rays and focus at a distance  $f_x$  above the lens surface. In Fig. A.2 a leaky ray through the lens center of curvature and the principal ray, that appears to come from the lens focus are shown. It follows from this Figure that:

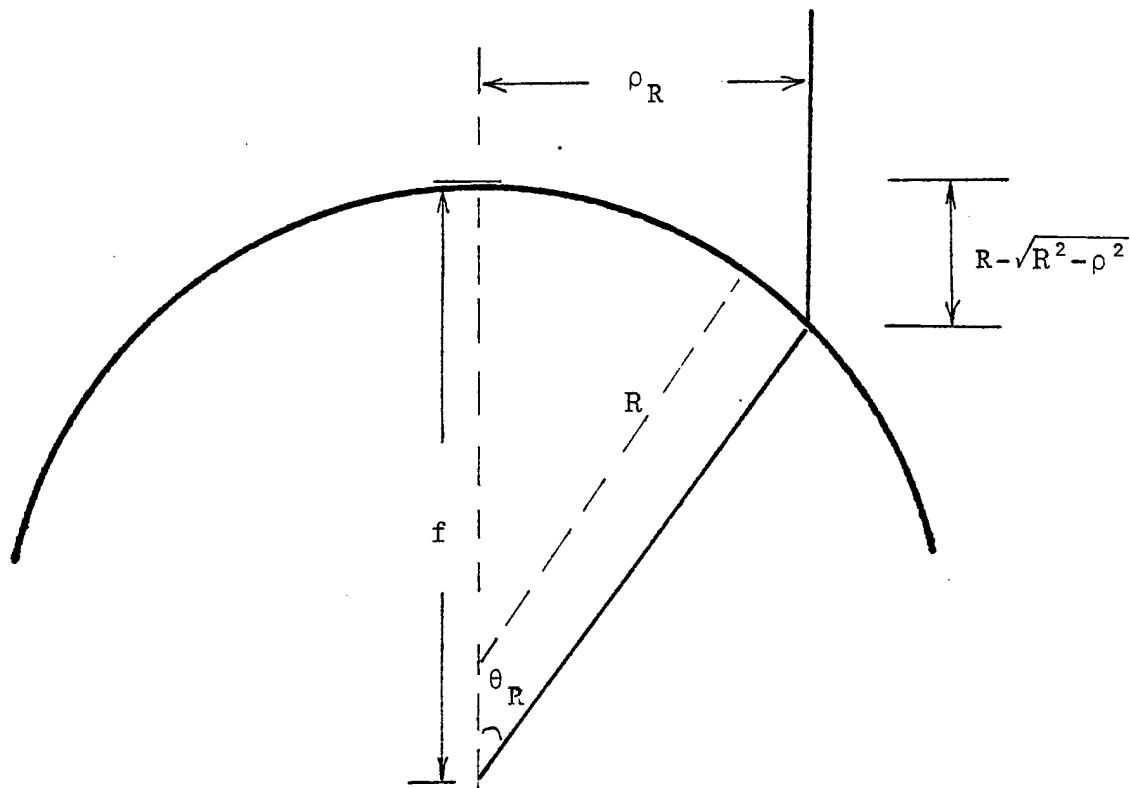


**Fig. A.1**

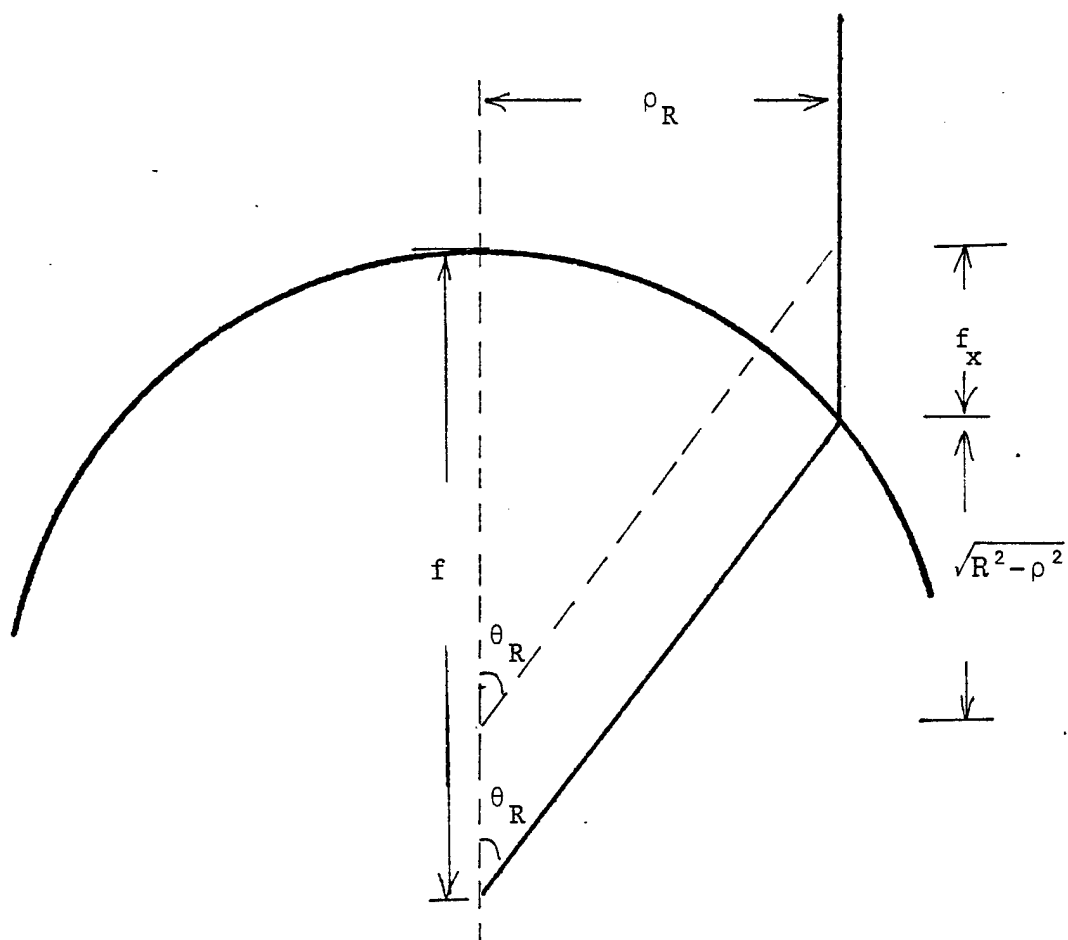


**Fig. A.2**

$$f_x = \frac{\rho_R}{\tan \theta_R} - \sqrt{R^2 - \rho_R^2} \quad . \quad (A.3)$$

### A.3 Derivation of $f_y$

The leaky rays re-radiated from the arc BAC (Fig. 4.8) form a cylindrical (line) focus at a distance  $f_y$  above the lens surface. These rays appear to originate from a point shown in Fig. 4.9 re-drawn for convenience in Fig. A.3. This line focus occurs at the intersection between the principal ray and a ray drawn through the lens center of curvature. Using Fig. A.3,  $f_y$  can be found from

$$\frac{2x}{\rho_R} = \frac{f - R + 2x/\tan \theta_R}{f_y + \sqrt{R^2 - \rho_R^2}} \quad . \quad (A.4)$$

Solving for  $f_y$ :

$$f_y = \frac{(f-R) \rho_R}{2x} + f_x, \quad (A.5)$$

where  $f_x$  is given by (A.3).



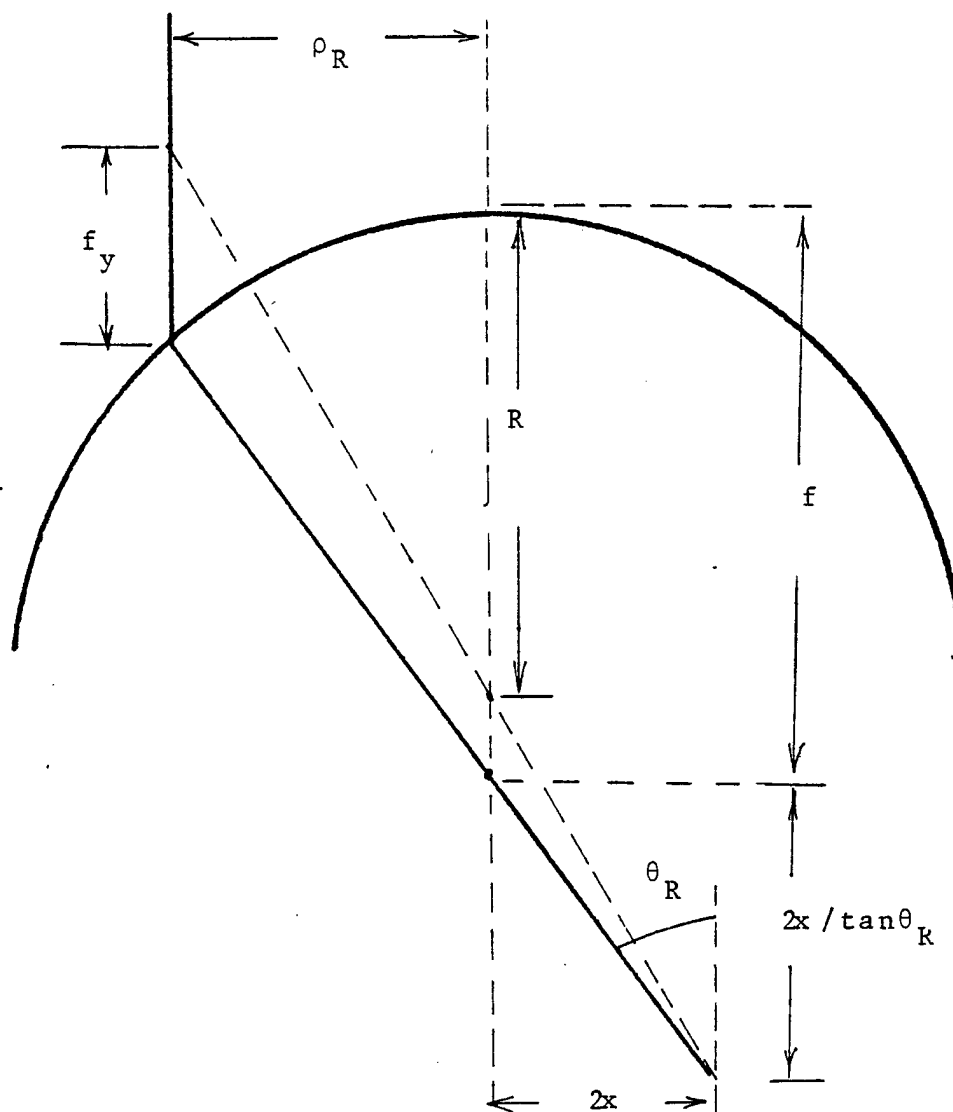


**Fig. A.3**

#### A. 4 Derivation of $\rho_{Rmin}$ , $\rho_{Rmax}$ , $c_{min}$ , $c_{max}$

The limiting rays of the leaky ray bundle that strikes the transducer cross the lens surface at  $\rho_{Rmin}$  and  $\rho_{Rmax}$ , shown in Fig. A.4. Using  $f_x \ll D$ , these quantities can be approximated as:

$$\begin{aligned}\rho_{Rmin} &= \rho_R - (R_T - \rho_R) f_x / D , \\ \rho_{Rmax} &= \rho_R + (R_T + \rho_R) f_x / D .\end{aligned}\tag{A.6}$$

These limiting rays appear to originate from points at  $\rho = c_{min}$  and  $\rho = c_{max}$ , respectively, on the sample surface, as shown in Fig. A.4. In Fig. A.4 the lens surface in the vicinity of  $\rho = \rho_R$  is approximated as a straight line at an angle  $\alpha$  with respect to a vertical line. The angle  $\alpha$  is found from

$$\alpha = \cos^{-1} (\rho_R / R) .\tag{A.7}$$

The quantities  $|z_{min}|$  and  $|z_{max}|$ , shown in Fig. A.4 are found to be

$$\begin{aligned}|z_{min}| &= |z| - (\rho_R - \rho_{Rmin}) (\cot \theta_R + \cot \alpha) \\ |z_{max}| &= |z| + (\rho_{Rmax} - \rho_R) (\cot \theta_R + \cot \alpha) .\end{aligned}\tag{A.8}$$

It follows from Fig. A.4 that

$$\begin{aligned}c_{min} &= |z_{min}| \tan \theta_R \\ c_{max} &= |z_{max}| \tan \theta_R .\end{aligned}\tag{A.9}$$

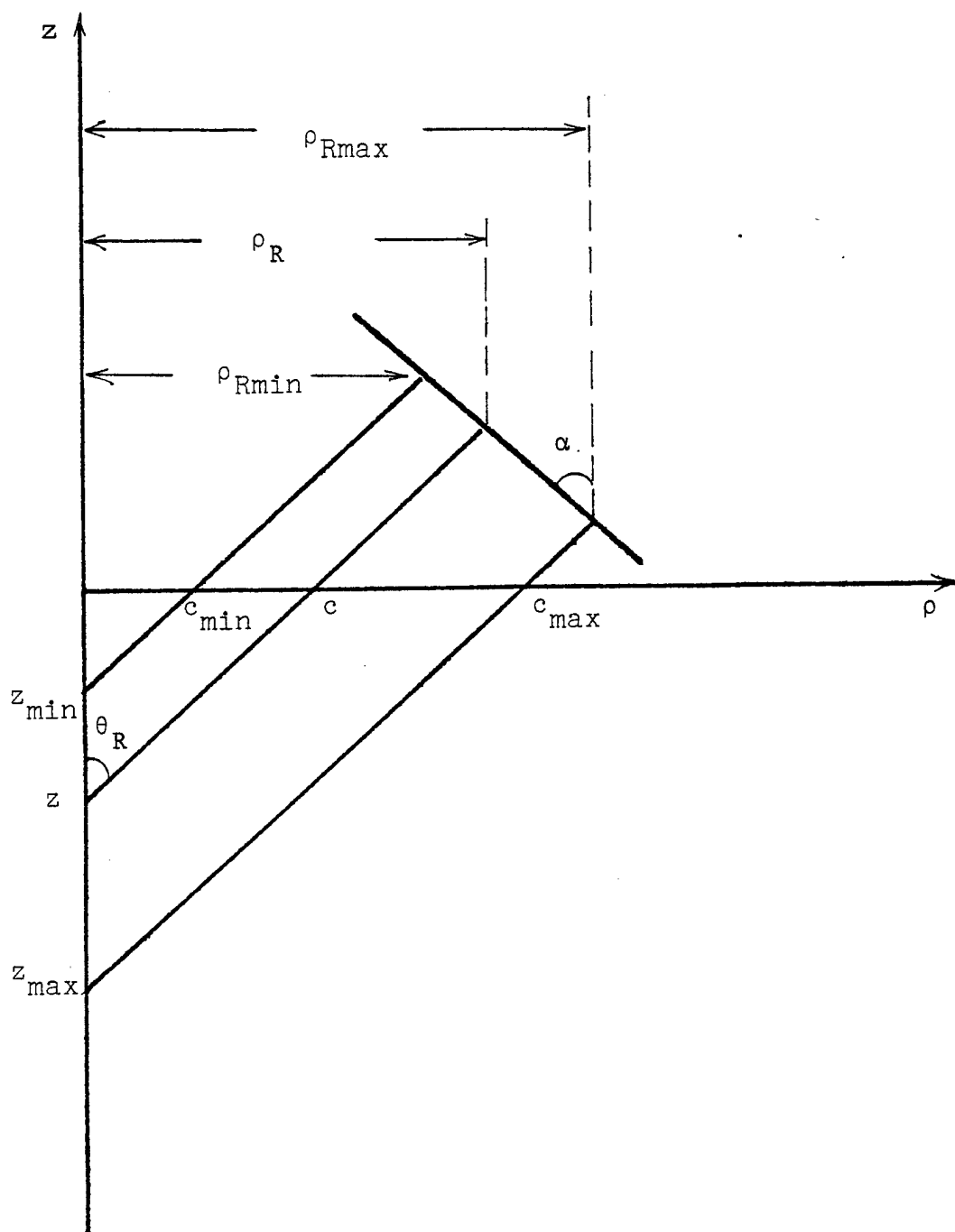


Fig. A.4

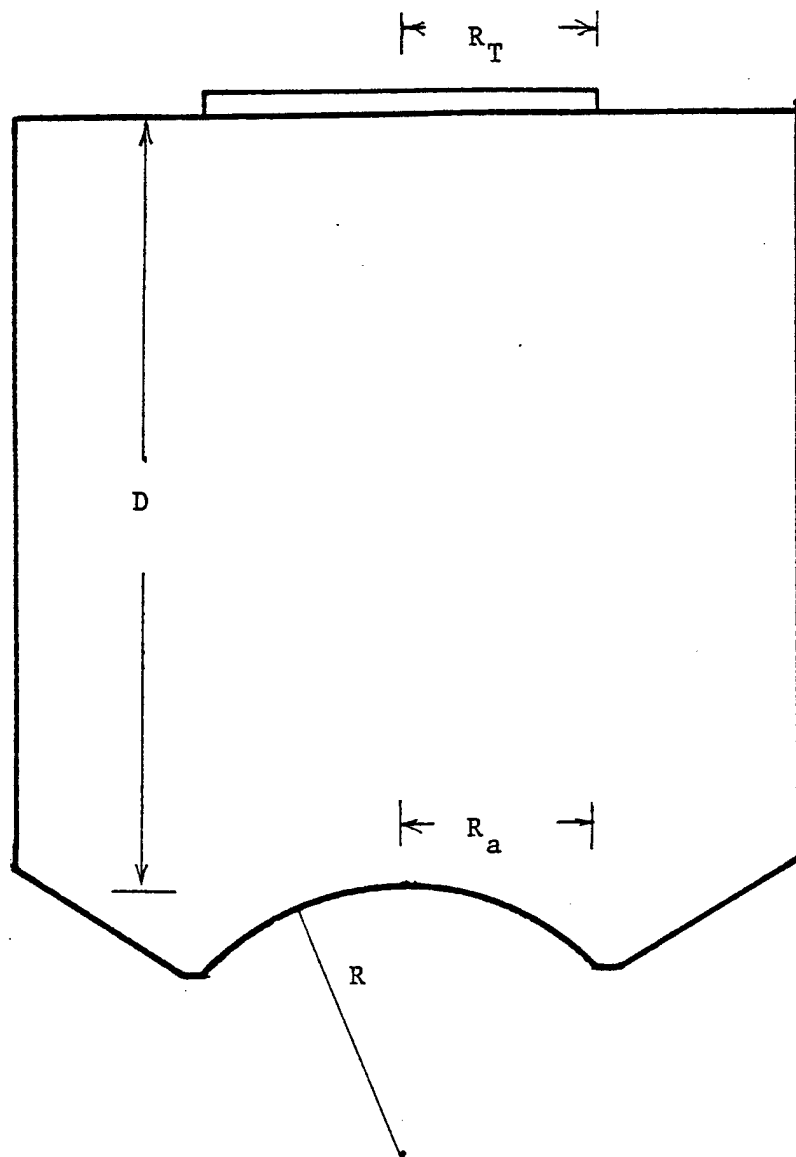


Fig. B.1 Lens dimensions

## References

- [1] R. G. Weglein, "A model for predicting acoustic material signatures", Appl. Phys. Lett. vol 34, pp. 179-181, 1979.
- [2] H.L. Bertoni , "Ray-optical evaluation of  $V(z)$  in reflection acoustic microscope", IEEE Trans. Sonics, Ultrason. ,vol. SU-31, pp.105-116, 1984.
- [3] Y. C. Angel and J.D. Achenbach, "Reflection and transmission of obliquely incident Rayleigh waves by a surface breaking crack", J. Acoust. Soc. Am. , 75 (2), pp.313-319, 1984.
- [4] J. Kushibiki, A. Ohkubo, and N Chubachi, "Acoustic anisotropy detection of materials using line-focus beam", 1981 IEEE Ultrason. Symp. ,pp.552-556, 1981.
- [5] D. A. Davids, P.Y. Wu, and D. Chizhik, "Restricted aperture acoustic microscope lens for Rayleigh wave imaging", Appl. Phys. Lett. 54 (17), pp. 1639-1641, 1989.
- [6] A. Atalar , "An angular spectrum approach to contrast in reflection acoustic microscopy", J. Appl. Phys. , vol. 49, pp. 5130-5139, 1978.
- [7] M. G. Somekh, H. L.. Bertoni, G. A. D. Briggs, and N. J. Burton, "A two-dimensional imaging theory of surface discontinuities with the scanning acoustic microscope", Proc. R. Soc. Lond. A 401, pp. 29-51, 1985.

- [8] V. S. Ahn, J. G. Harris, and J.D. Achenbach, "Acoustic material signature for a cracked surface", 1990 IEEE Ultrason. Symp., 1990.
- [9] J. W. Goodman, "Introduction to Fourier Optics", McGraw-Hill, New York, 1968.
- [10] A. A. Oliner, R. C. M. Li, H. L. Bertoni, "Catalog of acoustic equivalent networks for planar interfaces", Proc. IEEE, vol. 60 (12), pp. 1513-1518, 1972.
- [11] G. L. James, "Geometrical Theory of Diffraction for Electromagnetic Waves", Hertz, England: Peter Peregrinus, ch. 4, 1976.
- [12] J. N. Tjotta and S. Tjotta, "An analytical model for the nearfield of a baffled piston transducer", J. Acoust. Soc. Am., 68(1), pp.334-339, 1980.
- [13] G. A. D. Briggs, J. M. Rowe, A. M. Sinton and D. S. Spencer, "Quantitative methods in acoustic microscopy", Proc. IEEE 1988 Ultrason. Symp., pp. 743-749, 1988.
- [14] J. D. Achenbach, A. K. Gautesen, and D. A. Mendelsohn, "Ray analysis of surface-wave interaction with an edge crack", IEEE Trans. Sonics Ultrason., vol, SU-27 No. 3, pp. 124-129, 1980.